THESIS FOR THE DEGREE OF DOCTOR OF PHILOSOPHY

Ultraviolet vertical-cavity surface-emitting lasers and vertical microcavities for blue lasers

Filip Hjort

CHALMERS

Photonics Laboratory
Department of Microtechnology and Nanoscience (MC2)
CHALMERS UNIVERSITY OF TECHNOLOGY
Gothenburg, Sweden, 2021

Ultraviolet vertical-cavity surface-emitting lasers and vertical microcavities for blue lasers

Filip Hjort

ISBN 978-91-7905-499-1

Doktorsavhandlingar vid Chalmers tekniska högskola
Ny serie nr 4966
ISSN 0346-718X

Chalmers University of Technology
Department of Microtechnology and Nanoscience
Photonics Laboratory
SE-412 96 Göteborg
Sweden
Telephone: +46 (0)31-772 10 00

Front cover illustration: Left: Cross-sectional transmission electron microscopy (TEM) image of an ultraviolet B vertical-cavity surface-emitting laser (UVB VCSEL). Top center: Angle-resolved photoluminescence measurement of a UVB VCSEL above threshold. Bottom center: Schematic image of a UVB VCSEL. Top right: TEM image of an AlN/GaN distributed Bragg reflector with interlayers. Bottom right: Cross-sectional TEM image and simulated optical field in a GaN-prism microcavity.

Printed by Chalmers digitaltryck, Chalmers tekniska högskola, Göteborg, Sweden, 2021

Ultraviolet vertical-cavity surface-emitting lasers and vertical microcavities for blue lasers

Filip Hjort

Photonics Laboratory
Department of Microtechnology and Nanoscience
Chalmers University of Technology
SE-412 96 Göteborg, Sweden

Abstract

III-nitride materials are used for ultraviolet (UV) and visible light emitters. One such light source is the vertical-cavity surface-emitting laser (VCSEL) that could find applications within areas ranging from sterilization and medical treatment to car headlights and augmented reality displays. These devices are not yet commercialized, because of challenging mirror formation and electrical injection. However, due to the recent substantial performance improvement of blue-emitting VCSELs, it might not be long before they are available. UV VCSELs, on the other hand, are far from ready. Until recently, there were no VCSELs emitting in the UVB (280-320 nm) or at shorter wavelengths.

In this thesis, the first UVB VCSELs are demonstrated. These optically pumped devices emitting at wavelengths around 310 nm were realized by removing the substrate from high Al-content AlGaN structures using electrochemical etching, which allowed for the deposition of a high-reflectivity dielectric distributed Bragg reflector (DBR) on each side of the cavity. Thresholds below 1 MW/cm^2 were achieved by optimizing the sacrificial layer to achieve smooth etched surfaces and by accurately setting the cavity length and thereby the detuning.

Furthermore, electrically conductive DBRs for blue VCSELs were investigated. Insertion of interlayers in AlN/GaN DBRs increased the vertical resistance while measurements and simulations of ZnO/GaN multilayers showed that the resistance is similar to, or lower than, the lowest reported for pure III-nitride DBRs, as a result of the partial cancellation of polarization fields.

Finally, vertical cavities based on dislocation-free GaN microprism are demonstrated. The quality factor is strongly dependent on the prism diameter and is around 500 at yellow wavelengths for prisms with a 1-μm diameter. Simulations show that the quality factor should be approximately four times larger in the targeted blue wavelength regime.

These results serve as building blocks for future dislocation-free small-footprint VCSELs grown on low-cost substrates as well as short-cavity blue VCSELs with electrically conductive DBRs. Additionally, the UV VCSEL demonstration is an important step towards a compact, energy-efficient light source with attractive beam characteristics using a technology with great potential for realizing VCSELs in almost the full UV spectrum.

Keywords: vertical-cavity surface-emitting laser, GaN, AlGaN, electrochemical etching, ultraviolet, distributed Bragg reflector, electrical conductivity, nanostructures, microcavity

List of papers

This thesis is based on the following appended papers:

[A] **Filip Hjort**, Johannes Enslin, Munise Cobet, Michael A. Bergmann, Johan Gustavsson, Tim Kolbe, Arne Knauer, Felix Nippert, Ines Häusler, Markus R. Wagner, Tim Wernicke, Michael Kneissl, and Åsa Haglund, "A 310 nm optically pumped AlGaN vertical-cavity surface-emitting laser," *ACS Photonics*, vol. 8, issue 1, pp. 135-141, 2021.

[B] Giulia Cardinali, **Filip Hjort**, Nando Prokop, Johannes Enslin, Munise Cobet, Michael A. Bergmann, Johan Gustavsson, Joachim Ciers, Ines Häusler, Tim Kolbe, Tim Wernicke, Åsa Haglund, and Michael Kneissl, "Low-threshold UVB VCSELs enabled by post-growth cavity length adjustment and smooth surfaces," manuscript.

[C] Ehsan Hashemi, **Filip Hjort**, Martin Stattin, Tommy Ive, Olof Bäcke, Antiope Lotsari, Mats Halvarsson, David Adolph, Vincent Desmaris, Denis Meledin, and Åsa Haglund, "Effect of compositional interlayers on the vertical electrical conductivity of Si-doped AlN/GaN distributed Bragg reflectors grown on SiC," *Applied Physics Express*, vol. 10, p. 055501, 2017.

[D] **Filip Hjort**, Ehsan Hashemi, David Adolph, Tommy Ive, Olof Bäcke, Mats Halvarsson, and Åsa Haglund, "Vertical electrical conductivity of ZnO/GaN multilayers for application in distributed Bragg reflectors," *IEEE Journal of Quantum Electronics*, vol. 54, no. 4, p. 2400406, 2018.

[E] **Filip Hjort**, Maryam Khalilian, Jörgen Bengtsson, Marcus Bengths, Johan Gustavsson, Anders Gustafsson, Lars Samuelson, and Åsa Haglund, "Optical microprism cavities based on dislocation-free GaN," *Applied Physics Letters*, vol. 117, no. 23, p. 231107, 2020.

Related journal papers and conference contributions not included in the thesis:

Journal papers

[F] Magdalena Marciniak, Łucja Marona, Małgorzata Gramala, Robert Kudrawiec, Krzysztof Sawicki, Rafał Bożek, Wojciech Pacuski, Jan Suffczyński, Marcin Gębski, James A. Lott, **Filip Hjort**, Åsa Haglund, Tsu-Chi Chang, Tien-Chang Lu, and Tomasz Czyszanowski, "Impact of stripe shape on the reflectivity of monolithic high contrast gratings," manuscript.

[G] Joachim Ciers, Michael A. Bergmann, **Filip Hjort**, Jean-François Carlin, Nicolas Grandjean, and Åsa Haglund, "Smooth GaN membranes by polarization-assisted electrochemical etching," *Applied Physics Letters*, vol. 118, no. 6, p. 062107, 2021.

[H] Michael A. Bergmann, Johannes Enslin, **Filip Hjort**, Tim Wernicke, Michael Kneissl, and Åsa Haglund, "Thin-film flip-chip UVB LEDs realized by electrochemical etching," *Applied Physics Letters*, vol. 116, no. 12, p. 121101, 2020.

[I] Michael A. Bergmann, Johannes Enslin, Rinat Yapparov, **Filip Hjort**, Björn Wickman, Saulius Marcinkevicius, Tim Wernicke, Michael Kneissl, and Åsa Haglund, "Electrochemical etching of AlGaN for the realization of thin-film devices," *Applied Physics Letters*, vol. 115, no. 18, p. 182103, 2019.

Conference contributions

[J] **Filip Hjort**, Johannes Enslin, Munise Cobet, Michael A. Bergmann, Joachim Ciers, Giulia Cardinali, Tim Kolbe, Felix Nippert, Markus R. Wagner, Johan Gustavsson, Tim Wernicke, Michael Kneissl, and Åsa Haglund, "Advances in ultraviolet-emitting vertical-cavity surface-emitting lasers," *SPIE Photonics West*, 11686: Gallium nitride materials and devices XVI, online, Mar. 2021. (invited)

[K] Joachim Ciers, Michael A. Bergmann, **Filip Hjort**, Jean-François Carlin, Nicolas Grandjean, and Åsa Haglund, "Impact of polarization fields on electrochemical lift-off of GaN membranes," *SPIE Photonics West*, 11686: Gallium nitride materials and devices XVI, online, Mar. 2021.

[L] Michael A. Bergmann, Johannes Enslin, Martin Guttmann, Luca Sulmoni, Neysha Lobo-Ploch, **Filip Hjort**, Tim Kolbe, Tim Wernicke, Michael Kneissl, and Åsa Haglund "Thin-film flip-chip UVB LEDs enabled by electrochemical etching," *SPIE Photonics West*, 11686: Gallium nitride materials and devices XVI, online, Mar. 2021.

[M] Åsa Haglund, **Filip Hjort**, Johannes Enslin, Munise Cobet, Michael A. Bergmann, Ehsan Hashemi, Tim Kolbe, Johan Gustavsson, Jörgen Bengtsson, Tim Wernicke, and Michael Kneissl, "Recent progress for blue VCSELs and challenges to move to UV," *SPIE Photonics West*, OE107: Gallium nitride materials and devices XV, San Francisco, USA, Feb. 2020. (invited)

[N] Åsa Haglund, **Filip Hjort**, Johannes Enslin, Munise Cobet, Michael A. Bergmann, Ehsan Hashemi, Tim Kolbe, Johan Gustavsson, Jörgen Bengtsson, Tim Wernicke, and Michael Kneissl, "Are blue and ultraviolet VCSELs a reality or just a dream?," *SPIE Photonics West*, OE107: Vertical-cavity surface-emitting lasers XXV, San Francisco, USA, Feb. 2020. (invited)

[O] **Filip Hjort**, Johannes Enslin, Munise Cobet, Michael A. Bergmann, Tim Kolbe, Johan Gustavsson, Tim Wernicke, Michael Kneissl, and Åsa Haglund, "A 310 nm optically pumped AlGaN VCSEL with two dielectric distributed Bragg reflectors," *SPIE Photonics West*, OE107: Gallium nitride materials and devices XV, San Francisco, USA, Feb. 2020.

[P] Tim Wernicke, Luca Sulmoni, Martin Guttmann, Norman Susilo, Eviathar Ziffer, Christian Kuhn, Frank Mehnke, Anton Muhin, **Filip Hjort**, Johannes Enslin, Munise Cobet, Michael A. Bergmann, Martin Martens, Johan Gustavsson, Åsa Haglund, Michael Kneissl, "Prospects and challenges for UV LEDs and UV lasers with tunnel junctions," *SPIE Photonics West*, OE107: Gallium nitride materials and devices XV, San Francisco, USA, Feb. 2020. (invited)

[Q] Tim Wernicke, Luca Sulmoni, Martin Guttmann, Norman Susilo, Eviathar Ziffer, Christian Kuhn, Frank Mehnke, Anton Muhin, **Filip Hjort**, Johannes Enslin, Munise Cobet, Michael A. Bergmann, Martin Martens, Johan Gustavsson, Åsa Haglund, Michael Kneissl, "Prospects and challenges for UV LEDs and UV lasers with tunnel junctions," *Asian Pacific Workshop on Widegap Semiconductors*, Okinawa, Japan, Nov. 2019. (invited)

[R] Åsa Haglund, **Filip Hjort**, Michael A. Bergmann, Jörgen Bengtsson, and Johan Gustavsson, "Pushing performance in blue and UV VCSELs by nanometer structuring," *International Symposium Semiconductor Nanophotonics*, Berlin, Germany, Nov. 2019. (invited)

[S] **Filip Hjort**, Johannes Enslin, Michael A. Bergmann, Munise Cobet, Johan Gustavsson, Tim Kolbe, Tim Wernicke, Michael Kneissl, and Åsa Haglund, "UVB-emitting vertical-cavity surface-emitting lasers", *Heimbach XXXIII Workshop*, Colditz, Germany, Sep. 2019. (invited)

[T] Åsa Haglund, **Filip Hjort**, Michael A. Bergmann, Johan Gustavsson, Johannes Enslin, Munise Cobet, Tim Wernicke, Michael Kneissl, and Tim Kolbe, "UVB-emitting vertical-cavity surface-emitting laser", *International Workshop on UV laser Diodes*, Berlin, Germany, Aug. 2019. (invited)

[U] **Filip Hjort**, Johannes Enslin, Michael A. Bergmann, Munise Cobet, Johan Gustavsson, Tim Wernicke, Michael Kneissl, and Åsa Haglund, "Vertical microcavity based on an AlGaN membrane with two dielectric distributed Bragg reflectors emitting at 330 nm", *International Conference on Nitride Semiconductors*, Bellevue, USA, Jul. 2019.

[V] **Filip Hjort**[1], Maryam Khalilian[1], Filip Lenrick, Olof Hultin, Jovana Colvin, Marcus Bengths, Jörgen Bengtsson, Johan Gustavsson, Jonas Johansson, Rainer Timm, Reine Wallenberg, Jonas Ohlsson, Zhaoxia Bi, Åsa Haglund, Anders Gustafsson, and Lars Samuelson, "Quality factors of vertical cavities based on dislocation-free and atomically flat III-nitride hexagonal micro-prisms", *International Conference on Nitride Semiconductors*, Bellevue, USA, Jul. 2019.

[W] Maryam Khalilian, **Filip Hjort**, Filip Lenrick, Olof Hultin, Jovana Colvin, Marcus Bengths, Jörgen Bengtsson, Johan Gustavsson, Jonas Johansson, Rainer Timm, Reine Wallenberg, Jonas Ohlsson, Zhaoxia Bi, Åsa Haglund, Anders Gustafsson, and Lars Samuelson, "Growth of dislocation-free and atomically flat III-nitride micro-prisms", *International Vacuum Conference*, Malmö, Sweden, Jul. 2019.

[X] Åsa Haglund, Michael Bergmann, **Filip Hjort**, Ehsan Hashemi, Jörgen Bengtsson, and Johan Gustavsson, "Blue and ultraviolet vertical-cavity surface-emitting lasers", *Conference on and Lasers and Electro-Optics (CLEO)*, San Jose, USA, May 2019. (invited)

[Y] **Filip Hjort**, Johannes Enslin, Michael A. Bergmann, Munise Cobet, Johan Gustavsson, Tim Wernicke, Michael Kneissl, and Åsa Haglund, "Vertical AlGaN-microcavity with two dielectric distributed Bragg reflectors emitting at 330 nm", *VCSEL Day*, Brussel, Belgium, May 2019.

[Z] Åsa Haglund, Michael Bergmann, **Filip Hjort**, Ehsan Hashemi, Jörgen Bengtsson, and Johan Gustavsson, "Blue and ultraviolet thin-film light emitters", *UCSB-Chalmers Workshop by AoA Materials*, Gothenburg, Sweden, Jun, 2019.

[1]Equal contribution

[AA] Michael A. Bergmann, Johannes Enslin, **Filip Hjort**, Tim Wernicke, Michael Kneissl, and Åsa Haglund, "Thin-film UVB LEDs enabled by electrochemical etching of AlGaN", *International Workshop on Nitride Semiconductors*, OD14-7, Kanazawa, Japan, Nov. 2018.

[AB] Michael A. Bergmann, **Filip Hjort**, Ehsan Hashemi, David Adolph, Martin Stattin, Tommy Ive, Jörgen Bengtsson, Johan Gustavsson and Åsa Haglund, "Towards ultraviolet and blue microcavity lasers", *Northern Optics and Photonics Conference*, Lund, Sweden, Sep. 2018.

[AC] Åsa Haglund, Ehsan Hashemi, **Filip Hjort**, Michael Bergmann, Martin Stattin, David Adolph, Tommy. Ive, Jörgen Bengtsson, Johan Gustavsson, "Nanoscale structuring to improve laser performance", *Stanford Chalmers Workshop on Advancing Materials Innovatively*, Chalmers University of Technology, Sweden, Dec. 2017. (invited)

[AD] Åsa Haglund, Ehsan Hashemi, **Filip Hjort**, Michael Bergmann, Martin Stattin, David Adolph, Tommy Ive, Jörgen Bengtsson, Johan Gustavsson, "Optical feedback and confinement in GaN-based vertical cavity surface-emitting lasers", *Energy Materials Nanotechnology*, A22, Mauritius, Nov. 2017. (invited)

[AE] **Filip Hjort**, Ehsan Hashemi, David Adolph, Martin Stattin, Tommy Ive, Olof Bäcke, Mats Halvarsson, and Åsa Haglund, "Electrically conductive GaN-based distributed Bragg reflectors", *European Semiconductor Laser Workshop*, P2, Copenhagen, Denmark, Sep. 2017.

[AF] **Filip Hjort**, Ehsan Hashemi, David Adolph, Tommy Ive, and Åsa Haglund, "Electrically conductive ZnO/GaN DBRs grown by hybrid plasma-assisted molecular beam epitaxy", *SPIE Proceedings* 10104, 1010413, 2017. Presented at *SPIE Photonics West*, San Francisco, USA, Feb. 2017.

[AG] Ehsan Hashemi, **Filip Hjort**, Martin Stattin, Tommy Ive, and Å. Haglund "Effect of interlayers on the vertical electrical conductivity of Si-doped AlN/GaN DBRs grown by PA-MBE", *Optics and Photonics in Sweden*, Linköping, Sweden, Nov. 2016.

[AH] Åsa Haglund, Ehsan Hashemi, Jörgen Bengtsson, Johan Gustavsson, Martin Stattin, Stefan Carlsson, **Filip Hjort**, Marco Calciati, Michele Goano, Gatien Cosendey, Georg Rossbach, Marlene Glauser, and Nicolas Grandjean, "Progress and challenges in electrically pumped GaN-based VCSELs", *Workshop on Vertical-Cavity Lasers*, Gothenburg, Sweden, May 2016. (invited)

Acknowledgment

There are many people that deserve my gratitude for their support during this thesis work. I would like to start by thanking my main supervisor Prof. Åsa Haglund for giving me the opportunity to work within the exciting field of III-nitride VCSELs, for always being available for discussions, and for all the encouragement and guidance. I truly could not have wished for a better supervisor. I would also like to express gratitude to my assistant supervisors, Assoc. Prof. Johan Gustavsson and Assoc. Prof. Jörgen Bengtsson, for their help with simulations and valuable input, as well as to my examiner Prof. Anders Larsson for his support. Extra thanks to Jörgen for the countless enjoyable conversations during lunch time.

A special thank you to Dr. Ehsan Hashemi for welcoming me in the beginning and teaching me all there is to know about cleanroom fabrication. My deep gratitude goes to Dr. Michael Bergmann for being a central source of invaluable discussions, experimental support, and small talk during the past years. Thank you, Dr. Joachim Ciers, for sharing your knowledge, making the time spent in the office even more enjoyable, and for making Team Slow Light going a little bit faster. Lars Persson and Estrella Torres, I appreciate the enthusiasm and new perspective you have brought to the group, and I am happy to have had the opportunity to transfer some of my knowledge to you. It is with excitement I look forward to seeing what you will accomplish during your studies. Furthermore, it has been a pleasure to supervise Marcus Bengths, Mahdi Mohajeri, and Giulia Cardinali, which all made important contributions to my work.

Looking back, the importance of all the fruitful collaborations I have had the opportunity to be a part of becomes evident. I am grateful to all the people in the group of Prof. Michael Kneissl at the Technische Universität Berlin for enabling my work on UV VCSELs and for welcoming me in Berlin and to surrounding castles. Thank you Dr. Munise Cobet for introducing me to photoluminescence measurements, to Giulia Cardinali for giving my precious samples the attention they deserve, and to Dr. Tim Wernicke for all your smart ideas. Special thanks to Dr. Johannes Enslin for the fun times during your visit in Gothenburg, for the beers, and for all the samples grown. Furthermore, I am grateful for the collaboration on microprism cavities with Prof. Lars Samuelson's group at Lund University and especially for the cooperation with Prof. Anders Gustafsson and Dr. Maryam Khalilian. Moreover, the investigations of III-nitride DBRs would not have been possible without the excellent growth done by Dr. Martin Stattin, Dr. Tommy Ive, and Dr. David Adolph. I also would like to thank David for so generously sharing his experiences.

I am also lucky to have had the support of experienced and helpful cleanroom staff, which made the sometimes challenging fabrication work a bit easier. Here, Henrik Frederiksen deserves extra recognition for all his help.

These five years would not have been half as enjoyable and rewarding if it were not for all the colleagues at the Photonics lab. Thank you all for the lunchroom discussions, the interesting small talk, kick-offs, and the nice after works.

Finally, I would like to express my deepest gratitude to my friends and family. Especially to my mum and dad, Helga and Dick, for always being there and believing in me, not only during the last five years but since the start. Finally, Jenny, I cannot thank you enough for your unconditional support and for the joy you spread.

Filip Hjort
Gothenburg, May 2021

This work was done in part at the Nanofabrication Laboratory at Chalmers University of Technology belonging to the MyFab network and the Chalmers Materials Analysis Laboratory. This work was financially supported by Swedish Research Council, the Swedish Foundation for Strategic Research, the Swedish Energy Agency, and the European Research Council (ERC).

Abbreviations

AFM	atomic force microscopy
BTJ	buried tunnel junction
DBR	distributed Bragg reflector
ELO	epitaxial lateral overgrowth
FWHM	full width at half maximum
HCG	high contrast grating
IQE	internal quantum efficiency
ITO	indium tin oxide
LED	light-emitting diode
MBE	molecular beam epitaxy
MOCVD	metalorganic chemical vapour deposition
MOVPE	metalorganic vapour-phase epitaxy
PAMBE	plasma-assisted molecular beam epitaxy
PL	photoluminescence
Q	quality factor
Q3D-FEM	quasi-3D finite element frequency-domain method
QW	quantum well
RMS	root mean square
SEM	scanning electron microscopy
TEM	transmission electron microscopy
TJ	tunnel junction
TLM	transmission line measurement
TMM	transfer matrix method
UV	ultraviolet
UVA	ultraviolet A
UVB	ultraviolet B
UVC	ultraviolet C
VCSEL	vertical-cavity surface-emitting laser
VLC	visible light communication
YL	yellow luminescence

Contents

Chapter 1

Introduction

Ever since the first laser was demonstrated in 1960 [1, 2], the range of applications have continuously expanded and lasers are today used for countless purposes in consumer products, manufacturing, and research. There is a plethora of laser types and their applications depend on the properties of the device as well as of the coherent light its emits. Semiconductor lasers are preferred in many applications due to their compact size, low power consumption, and low cost. The vertical-cavity surface-emitting laser (VCSEL) is a type of semiconductor laser that today forms a fast-growing billion dollar industry [3]. The commercial success of GaAs-based infrared-emitting VCSELs was from an early stage driven by applications in short-reach optical data communication and computer mice and, more lately, by an increasing demand in 3D sensing applications such as face recognition [3–5]. The widespread use in completely different areas stem from the numerous beneficial traits of VCSELs. These include their very small footprints, low threshold currents and resulting low power consumption, and circular-symmetric and low-divergence output beams. VCSELs are also easily fabricated in 2D arrays, which lowers fabrication cost due to the possibility of on-wafer testing. Furthermore, VCSELs can be modulated at high speed at low currents, typically have single longitudinal mode emission that shows a relatively small wavelength shift with temperature and can be tuned continuously with current. Additionally, VCSELs can be made for single transverse-mode operation. Compared to light-emitting diodes (LEDs), VCSELs can provide higher conversion efficiencies at high current densities giving larger achievable output power per chip area [4].

Infrared GaAs-based VCSELs were first conceived by Iga et al. in 1979 and commercialized in 1996 [6–8], but despite its great success, the counterparts in the ultraviolet (UV) to green spectral region are still not commercially available. In the early 1990s, when GaAs-based VCSELs were rapidly improving in performance and moving closer to volume production, there were still no semiconductor materials suitable for compet-

itive UV to green LEDs and lasers. This changed due to the work of Isamu Akasaki, Hiroshi Amano, Shuji Nakamura et al., in which the crystal quality and p-type doping of GaN [9–12] were improved, enabling Nakamura et al. to demonstrate the first blue-emitting high brightness LEDs and lasers in the mid-1990s [13–17]. The realization of high-brightness blue-emitting LEDs also allowed for energy-efficient white light LEDs, and in 2014, Akasaki, Amano, and Nakamura were awarded the Nobel Prize in Physics for their work. Following the break-through in blue LEDs and lasers, research on GaN-based materials and devices intensified and the III-nitrides, which is the semiconductor group that GaN belongs to, are today the completely dominating semiconductor materials for UV and visible light emitters.

Also III-nitride-based VCSELs gained considerable attention and in 2008 the first electrically injected blue-emitting devices were realized [18, 19]. However, the continued progress has been hampered by challenges in, for example, mirror fabrication, electrical injection, and thermal management. Nevertheless, in the last few years, the performance of the best devices has improved significantly with achieved output powers of up to 24 mW, threshold current densities of a few kA/cm^2, and wall-plug efficiencies around 10%. Furthermore, yields of over 80% over a 2-inch wafer and 1000 hours continuous operation at room temperature have been demonstrated [20–22]. These results holds promise for near-time commercialization. In contrast, limited progress has been made for UV-emitting VCSELs. For wavelengths shorter than around 360 nm, these must be made using AlGaN, and the shorter the UV-emission wavelength, the higher the Al content must be. So far, AlGaN VCSELs have mainly been constrained to low Al content and solely to optically pumping. Nevertheless, research in both blue- and UV-emitting VCSELs remains intense and is fueled by the great potential of III-nitride VCSELs in numerous and wide-ranging areas.

1.1 Applications

Which applications III-nitride VCSELs will be used for will heavily depend on the achievable performance characteristics, such as optical output power, threshold current, and wavelength stability. Furthermore, factors such as reproducibility, lifetime, and manufacturing cost will play important roles. Different applications will also demand different emission wavelengths. In the visible spectrum, III-nitride VCSELs can enable wavelengths from blue to green and potentially orange, which together with the red-emitting VCSELs already available using other materials systems would provide VCSEL emission extending over the entire visible range. Additionally, III-nitride VCSELs could, at least in theory, be made with emission wavelengths almost anywhere in the non-vacuum compatible UV spectrum. This spectral range is often divided into three bands: UVA (320-400 nm), UVB (280-320 nm), and UVC (200-280 nm). Certain application areas, such as sensing, demand a wide range of wavelengths, while others, such as disinfection (UVC) and solid-state lighting (blue), are limited to a specific part of the spectrum.

Infrared VCSELs are employed in several different sensing applications, such as time-of-flight distance measurement, 3D imaging, computer mice, and gas analysis [5]. Optical gas sensing, such as tunable laser diode spectroscopy, has the benefit of being fast, non-destructive and typically having high sensitivity and gas specificity. In the UV, e.g. ozone, SO_2, NO_2, benzene, toluene, and xylene have strong absorption bands and so far deuterium or mercury lamps have most often been used as light sources. UV LEDs are emerging as alternative light sources that benefit from low operating voltages, long life times, low production cost, relatively narrow and stable emission spectrum with freedom to choose the peak spectral position, no warm-up times, less heat generation, compactness, better mechanical stability and absence of toxic mercury [23–25]. VCSELs share most of the benefits of LEDs but could also provide an even narrower emission spectrum, faster modulation speed, and more efficient fiber coupling. The low power consumption and the symmetric and low-divergent beam can make VCSELs more suitable than Fabry-Pérot or distributed feedback lasers.

Due to their high reliability and low power consumption, infrared VCSELs have also been used in chip-scale atomic clocks [26]. UVA VCSELs could in a similar way support the development of compact Yb^+ atomic clocks as the 369 nm pump laser previously employed prevents both a low power consumption and miniaturization [27, 28].

UV and visible light can be used to excite fluorescence in biological compounds such as amino acids, vitamins, and proteins, including enzymes, and can therefore be used for medical analysis, for example in cancer diagnosis [29–31]. Lasers are often used for fluorescent excitation, e.g. for time-resolved measurements [29, 32], and VCSELs could provide a compact laser with potential for point-of-care testing and lab-on-a-chip integration. Furthermore, the compact size and low power consumption could allow for VCSELs to be used in in-vivo treatment and diagnostics as an alternative with better high-speed performance and more directed beam than (micro-)LEDs [33, 34]. Thus, VCSELs could replace blue LEDs that, for example, have been used for neuron stimulation in cochlear implants [35–37].

Both UVA and UVB light are used for treatment of skin deceases such as vitiligo and psoriasis. Around 2% of all people suffer from vitiligo and 2-3% from psoriasis. UVA light in combination with the chemical compound psoralen can be used for treatment of both these diseases, but due to several side effects, such as an increased risk for skin cancer, it has to a large extent been replaced by narrow-band UVB phototherapy. The narrow-band UVB phototherapy usually consist of exposure to light with wavelengths around 310 nm, typically using fluorescent lamps, or in the case of targeted therapies, excimer lasers [38–40]. UVB LEDs are emerging as an alternative light source but VCSELs could provide additional benefits such as higher irradiance, more directional output beams, and a combination of targeted and large area treatment using arrays of individual addressable devices.

UVB light can also be used to improve agricultural products. For example, UVB exposure can enhance plants' production of secondary metabolites, which may have several

health benefits including antioxidant and anticarcinogenic effects [41]. Furthermore, exposure of egg laying hens to UVB light showed an increase in egg yolk vitamin D content [42]. VCSELs could potentially find use in agricultural UVB system that would benefit from more directional light and narrower emission spectrum than what is typically achieved for LEDs.

Maybe the most important application of UV light is the disinfection of air, water, and surfaces [43–45]. The germicidal effect is a result of the photochemical changes of microorganism DNA or RNA upon UV exposure that prevents the bacteria and viruses from reproducing themselves. The germicidal effect is mainly present for UVB and UVC wavelengths and is strongest in the UVC, around 260-265 nm, but also depends on the specific organisms [45]. The importance of improved means to reduce the spread of infectious diseases has become obvious during the ongoing Covid-19 pandemic. UVC light exposure can be used for intermediate exposure of commonly touched surfaces, or continuous exposure of air in ventilation systems, to inactivate SARS-CoV-2 or any viruses and bacteria of future pandemics [43]. Furthermore, the World Health Organization has estimated that as much as half a million deaths annually can be attributed to unsafe drinking water in low- and middle-income countries [46], which could be significantly reduced by a wider roll-out of UV disinfection solutions for water. UV VCSEL arrays, similar in layout to the high-power infrared VCSEL modules delivering power densities above 100 W/cm^2 for heat treatment applications [47], could facilitate new energy-efficient and small foot-print UV disinfection solutions with high throughput for both small and large scale water treatment as well as for air and surface disinfection systems.

Both UV and visible light is regularly used for curing of resins to form polymer materials such as inks, plastics, coatings, and adhesives. This process is employed in a wide range of fields, including dental, 2D and 3D printing, and medical applications [48–50]. VCSELs could potentially provide low-cost and compact but still high-throughput systems for homogeneous curing of coatings, provide targeted curing through fiber-coupling in dentistry or medicine, be used in digital light processing 3D printing [49], and allow for higher resolution classical 2D printing.

Phosphor-coated blue-emitting LEDs are today dominating white-light generation, but the number of lumens achievable per chip area is limited by a droop in efficiency at high current densities. Lasers can achieve higher efficiencies at high current densities, which make them suitable for compact, directional and high brightness light sources such as flashlights, floodlights, and adaptive headlights for cars. The higher optical output power per chip area could also lead to considerable cost savings [51]. In contrast to edge-emitting lasers, VCSELs can easily be fabricated in 2D arrays and allows for low-cost manufacturing due to on-wafer testing, and together with the highly directional and circular-symmetric beams, VCSELs could be used to realize the full potential of laser-based solid-state lighting [33].

By virtue of their compact size, 2D-array compatibility, beneficial beam properties, low power consumption, as well as the higher brightness and spectral purity compared

to LEDs, VCSEL could also be used in numerous displays applications ranging from picoprojectors, very large-sized high-brightness displays to wearable electronics such as retinal scanning displays for augmented and virtual reality [22, 52].

The high modulations speeds at small currents also make VCSELs suitable for visible light communication (VLC). VLC can be used to provide high-speed data communication with an added layer of security and VCSELs could be used as a higher speed alternative to LEDs in indoor VLC light sources [53]. Potentially, VCSELs with UVC emission could also be used in solar blind non-line-of-sight communication and blue- or green-emitting devices in underwater optical wireless communication [54–56].

The above discussed areas are just a sample of possible future applications of UV- and blue-emitting VCSELs. As predictions like these are highly speculative in nature, some of these applications will not materialize while others may become commercial drivers. Furthermore, just like few people a decade or two ago predicted the advent of 3D-sensing infrared VCSEL arrays in smartphones, there might be large volume applications of UV and blue VCSELs not yet foreseen. Nevertheless, based on the many beneficial traits of VCSELs and the huge technological importance of light in the UV to green spectrum, it is very likely that such light sources will find multiple applications, which prompt research efforts dedicated to these devices.

1.2 This thesis

Motivated by the various potential applications of III-nitride VCSELs, this thesis is devoted to work that can support the improvement in performance of both UV- and blue-emitting VCSELs. In Chapter 2, the most important properties of the III-nitride materials are explained, and this is followed by an introduction to VCSELs in Chapter 3. Chapter 4 gives a detailed overview of the III-nitride VCSEL field, including the different device geometries demonstrated, the main challenges, the state-of-the-art performance, and what solutions that can be used to extend the emission to shorter wavelengths. These three chapters provides a foundation for the research work presented in the appended papers, which are introduced and discussed in the three following chapters. Chapter 5 concerns the demonstration of the first optically pumped UVB VCSEL, its lasing performance, and an investigation of what is needed to realize UVC VCSELs using the same methods. Chapter 6 introduces two different types of electrically conductive distributed Bragg reflectors (DBRs); AlN/GaN DBRs and the influence of compositional interlayer, and the first investigation of the vertical electrical conductivity of ZnO/GaN multilayers. Chapter 7 shows how nanowire-based GaN prisms can be used to form dislocation-free vertical cavities. All the results are summarized in Chapter 8 where additional work needed and the future directions of the field will also be discussed. Finally, in Chapter 9, a summary of the appended papers is presented.

Chapter 2

III-nitride materials

The III-nitride materials system is a group of materials that consist of one or multiple of the metals Al, Ga, and In, which have three valence electrons, combined with the five valence electron element nitrogen. AlN, GaN, and InN, as well as their alloys, have direct bandgaps that can be tuned for emission from the far UVC to infrared wavelengths, as shown in Fig. 2.1. These properties have made III-nitrides very attractive for optoelectronic devices, especially for emission in the UV to green spectral range where there is a lack of other inorganic semiconductor materials suitable for efficient light generation.

2.1 Crystal structure

The thermodynamically stable crystal structure of the III-nitrides under ambient conditions is wurtzite, which is also the stable structure for the II-VI material ZnO. As shown in Fig. 2.2, wurtzite consists of two hexagonal closed-packed planes, each with only one type of atoms and with a lattice constant a, repeated in an AaBb stacking order. The out-of-plane lattice constant is c and the spacing between aligned planes of different atom types is $5c/8$ or $3c/8$. Crystal directions and planes are denoted using the four lattice vectors $\mathbf{a_1}$, $\mathbf{a_2}$, $\mathbf{a_3}$, and $\mathbf{c}$. Figure 2.2 also shows the orientation of the polar c-plane, the nonpolar a- and m-plane, and an example of a semipolar plane (s-plane), the r-plane. Furthermore, the direction of what is denoted as the metal-face (or Ga-face, Al-face, etc.), and the N-face in the non-centrosymmetric structure is also shown. Analogously, crystals or surfaces that are grown or oriented in these directions are often called metal-polar or N-polar [58].

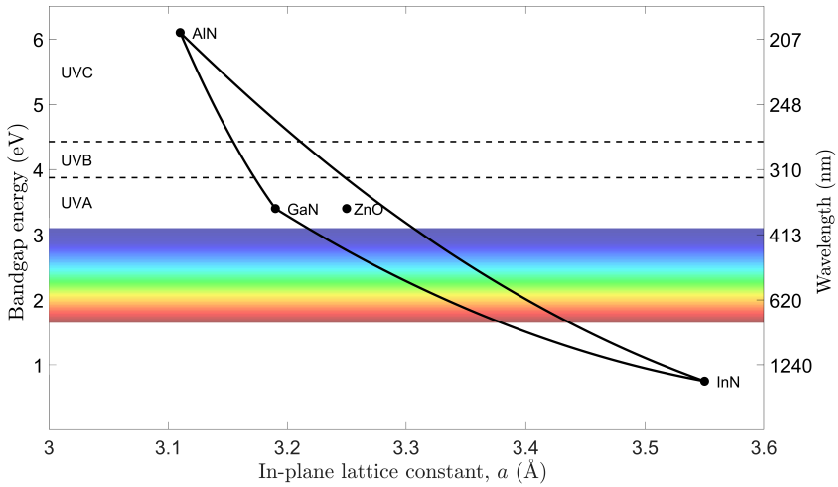

Figure 2.1: Bandgap energy and wavelength of III-nitride materials and ZnO versus in-plane lattice constant. Material data is taken from Ref. [57].

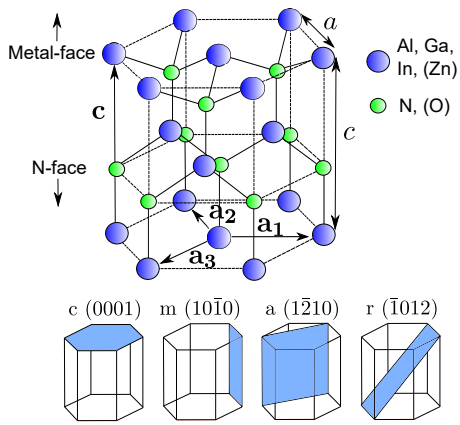

Figure 2.2: The wurtzite crystal structure and four important crystal planes.

2.2 Growth

Two of the most common methods of growing III-nitride heterostructures are metalorganic vapour-phase epitaxy (MOVPE) and molecular beam epitaxy (MBE). In MOVPE, which is also called metalorganic chemical vapour deposition (MOCVD), the growth is driven by chemical processes in which precursor gases react at the substrate surface held in a chamber under moderate pressures and elevated temperatures. Metalorganic gases such as triethylgallium (TEG), trimethylgallium (TMGa), or trimethylaluminium (TMAl) are used as metal precursors and NH_3 as precursor for nitrogen, while N_2 and H_2 are used as carrier gases. In contrast, MBE is done in ultra-high vacuum chambers where the metals atoms are provided by high-purity solid sources that are heated in effusion cells to create molecular beams that impinge on the heated substrate surface. For growth of III-nitrides using plasma-assisted MBE (PAMBE), the metal atoms react with active nitrogen that is introduced in the chamber using a plasma source.

One of the main challenges in epitaxial growth is achieving low-defect-density crystals. Low-defect growth is especially challenging when the materials have large differences in their in-plane lattice constant. The larger the lattice mismatch, and the thicker the grown layer, the more likely the crystal is to crack or form dislocations that can impede device performance. The relatively large lattice mismatches of the III-nitrides, as shown in Fig. 2.1, put limitations on what heterostructures can be grown with relatively high quality. Additionally, due to the high cost of free-standing substrates of GaN and AlN, most devices are grown on GaN- or AlN-on-sapphire templates, which have relatively high threading dislocation densities in the range of 10^7-10^{10} cm^{-2} [59, 60]. UVB devices need thick layers of AlGaN with close to 50% Al content and therefore have a large lattice mismatch to both GaN and AlN. As a result, high quality growth becomes especially challenging and often leads to lower efficiencies for UVB LEDs and higher threshold currents for UVB lasers than for their UVA and UVC counterparts [59, 61, 62]. Low dislocation densities can be especially important for lasers as high dislocation-density substrates may reduce both device lifetime and efficiency [63]. As a consequence, commercial blue edge-emitting lasers are typically grown on relatively small and expensive free-standing GaN substrates and the same is true for state-of-the-art III-nitride VCSELs [20–22]. As dislocation management still is one of the largest challenges for III-nitride growth, it remains an active research area with many different solutions used, including buffer layers [9], superlattices [64–67], relaxed AlGaN pseudosubstrates [64], epitaxial lateral overgrowth (ELO) [68, 69], high-temperature annealing [70], and nanostructures [71–73].

2.3 Electrical properties

Another major challenge with III-nitride growth is achieving high electron and hole concentrations using impurity doping. Typically, n-doping is done using Si and dopant con-

centrations up to over $10^{19}\,\mathrm{cm}^{-3}$ are regularly realized without significant degradation in crystal quality. The relatively low ionization energy for Si in GaN results in electron concentrations similar to that of the Si concentration. However, as the Al content increases, so does the ionization energy of the dopants, which leads to less efficient doping, especially for Al contents over 80% [74, 75]. Achieving high p-doping, which is typically done using Mg, is considerably more challenging because the relatively high ionization energy and compensating defects limit the hole concentrations to the order of $10^{18}\,\mathrm{cm}^{-3}$. Also in the case for p-doping, the difficulty in reaching high hole concentrations increase significantly with Al content due to higher ionization energies [74, 76].

Another property with a large influence on the electrical properties of III-nitrides are polarization fields. The asymmetry of the wurtzite crystal structure gives electrical fields that are dependent on the crystal orientations. The III-nitrides have large electronegativity differences, which makes these polarization fields relatively large. Inside bulk materials, the polarization fields cancel, but at interfaces of a heterostructure, they give rise to effective sheet charge densities that consist of two components. The first is the spontaneous polarization charge and is independent on the strain in the structure and the second is the piezoelectric polarization charge that is proportional to the strain. The total sheet charge density at a c-plane interface between two wurtzite layers A and B, where layer A is in-plane pseudomorphically strained to B, can be calculated using the formula

$$\sigma = P_{\mathrm{sp}}^{\mathrm{A}} - P_{\mathrm{sp}}^{\mathrm{B}} + 2\left(e_{31} - \frac{c_{13}}{c_{33}} e_{33}\right) \frac{a_{\mathrm{B}} - a_{\mathrm{A}}}{a_{\mathrm{A}}}, \tag{2.1}$$

where a is the in-plane lattice constant and P_{sp} is the spontaneous polarization charge densities of the two materials, and where e_{31} and e_{33} are the piezoelectric constants and c_{13} and c_{33} are the elastic constants for layer A. These interface charges, together with band offsets, give rise to band bending and potential barriers that can impede electron flow perpendicular to the interfaces. Polarization charges also give rise to the quantum-confined Stark effect, where the radiative recombination rate is reduced and the emission wavelength is redshifted. This effect is especially prominent for wide quantum wells (QWs) but is reduced at high carrier densities. It may be completely or partly avoided by using nonpolar or semipolar structures [58].

2.4 Optical properties

GaN has a bandgap of around 3.4 eV at room temperature corresponding to emission in the UVA near 360 nm. InGaN alloys are used in the QWs to achieve emission in the visible and near UVA, while AlGaN alloys are used to obtain emission at shorter wavelengths in the UVB and UVC. The recombination rate is often roughly approximated by

$$R = An + Bn^2 + Cn^3, \tag{2.2}$$

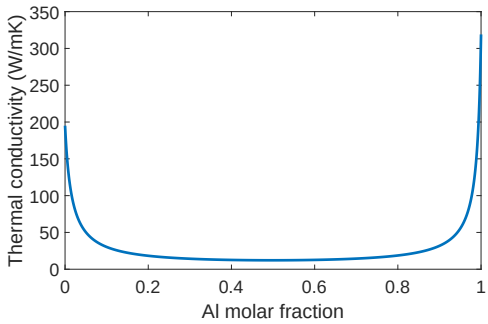

Figure 2.3: Thermal conductivity of AlGaN calculated using the material parameters in Ref. [81].

where n is the carrier density and A, B, and C are constants. Bn^2 is the radiative recombination rate while An comes from the trap-assisted Shockley-Read-Hall recombination rate and Cn^3 from Auger recombination rate, both non-radiative [58, 77]. High levels of trap-assisted non-radiative recombination will lead to poor efficiency in LEDs and higher thresholds in lasers. One important performance metric is the internal quantum efficiency (IQE), which is the ratio of radiative to total recombination. InGaN QWs can have IQEs above 90%, even when grown on relatively high dislocation density GaN-on-sapphire templates. This is attributed to carrier localization as a result of In fluctuations [77–79]. However, for InGaN QWs with lower In content and emission of around 400 nm and below, as well as for AlGaN QWs, the carrier localization is less and UV-emitting devices are, consequently, more sensitive to dislocations than blue-emitting devices [59, 79]. In addition to dislocations, point defects in the active region can increase the non-radiative recombination efficiency. Specifically, surface defects in GaN that are trapped during growth of InGaN QWs can have a detrimental effect on the radiative efficiency. However, this can be avoided by trapping the defects before the growth of the QWs using an InGaN underlayer [80].

2.5 Thermal properties

The binary compounds AlN, GaN, and InN have significantly higher thermal conductivity than ternary materials AlGaN, InGaN, and AlInN, as shown in Fig. 2.3. This is due to alloy scattering, and for AlGaN with around 50% Al content the thermal conductivity drops to below 1/10 of the values of the binary compounds [81]. The thermal conductivity will also depend on the deposition method and material quality as well as on the doping and thickness of the layers [82].

2.6 Growth of nanostructures

The traditional growth method is to grow homogeneous layers on top of a planar substrate, so called two-dimensional growth. However, it is possible to grow three-dimensional nanometer- or micrometer-sized structures by choosing appropriate growth substrate and growth conditions, and/or by pattering the substrates. These structures have the benefit that they can incorporate more strain and can achieve nonpolar or semipolar planes even when grown on a c-plane substrate [83, 84]. Furthermore, they can be used for small-footprint devices and can filter out threading dislocations [71–73]. It is possible to achieve controlled 3D growth using selective area growth where the growth substrates is patterned or partially covered by a mask to control the location where growth can start. Selective area growth can be used to create ordered array of nanowires but also ELO AlN- or GaN-on-sapphire templates with lower dislocation densities than what is achievable with two-dimensional growth on non-structured sapphire wafers [68, 69, 71–73].

Chapter 3

Fundamentals of vertical-cavity surface-emitting lasers

Figure 3.1 shows an example of a vertical-cavity surface-emitting laser structure. For VCSELs, the optical feedback is given by two mirrors that are parallel with the wafer plane and in this way forms a vertical cavity. One of the main challenges with VCSELs is that the vertical geometry, where the active region is perpendicular to the direction of light propagation, results in small round-trip gain. Therefore, the round-trip losses must be kept low, which is achieved using high-reflectivity mirrors. Typically, the mirrors employed are DBRs which use multiple reflections and constructive interference to achieve high reflectivity at specific wavelengths. If the top mirror has the lowest reflectivity of the two DBRs, the vast majority of the light is emitted through the top and the VCSEL is referred to as a top-emitting device, and if the bottom mirror has the lowest reflectivity, the majority is emitted through the substrate and the device is referred to as bottom-emitting. The gain is provided by an active region consisting of a few QWs that is positioned at an optical antinode of the standing wave within the cavity while lossy layers are positioned at optical nodes. Electrical contacts are used to pump the active region and structures to laterally confine the light as well as the current are also included. For initial demonstrations, with the goal to demonstrate that the cavity is of sufficiently high quality to support lasing, the structure is usually optically pumped using a shorter wavelength laser instead of using electrical contacts for pumping. This simplifies the epitaxial structure and device layout.

The vertical geometry and emission direction of the VCSEL have several benefits. In contrast to edge-emitting lasers, these devices can be characterized before dicing the wafer, which allows for significant savings in manufacturing cost. Furthermore, this allows for easy fabrication of two-dimensional VCSEL arrays. The footprint, and thus the active region of a VCSEL, is also much smaller than that of edge-emitting lasers which

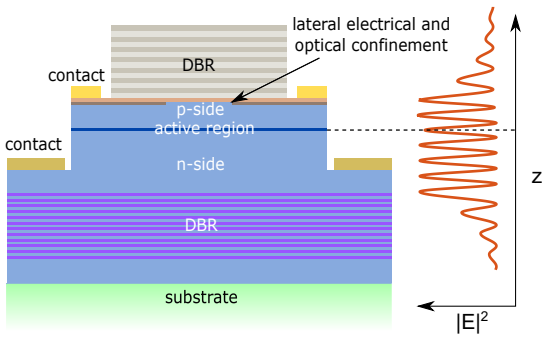

Figure 3.1: Example of a VCSEL structure with intracavity contacts. The red curve shows a standing electric field profile along the VCSEL z-axis.

results in a low threshold current. Additionally, the small device volume makes it possible to achieve high speed modulation even at lower currents and the short cavity length leads to a large mode spacing. The large mode spacing ensures single longitudinal mode lasing since only one of the longitudinal modes typically will overlap with the gain spectra and DBR stopband. It is also possible to achieve single transverse mode operation and, as a result of the lasing area being defined in the wafer plane, the emission is typically circular symmetric with a low divergence [4].

Although having many benefits, the VCSEL structure entails some manufacturing challenges. These include high-reflectivity mirrors, a high sensitivity to cavity length variations, and to achieve optical guiding and homogeneous current injection.

3.1 Distributed Bragg reflectors

DBRs consist of stacks of two alternating high and low refractive index materials where the thickness of each layer corresponds to a quarter of the target wavelength. The peak reflectivity and stopband width depends on the number of material pairs and the refractive index contrast between them, as shown in Fig. 3.2.

Reflection and transmission from multilayered structures such as DBRs can be simulated with the transfer matrix method (TMM). The transfer matrices for reflection at each interface and for propagation in each material are multiplied together to give the overall transfer matrix of the system,

$$T_{\text{tot}} = T_N T_{N-1} \ldots T_3 T_2 T_1, \tag{3.1}$$

where each T_i corresponds to either the transmission through a layer or reflection at an

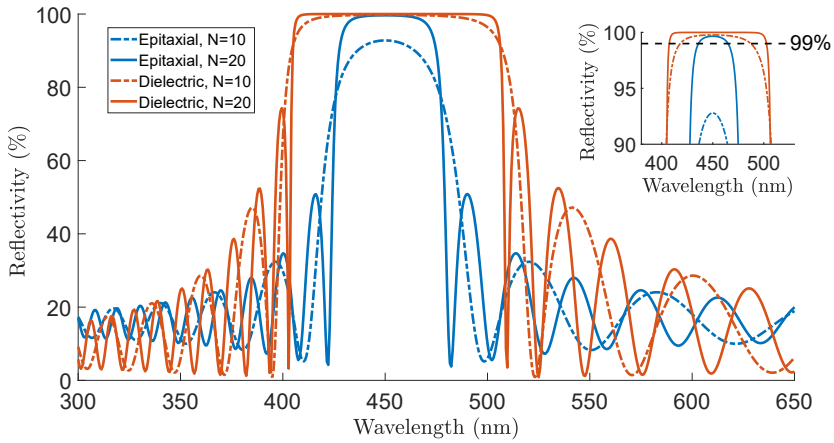

Figure 3.2: Simulated reflectivity of an epitaxial DBR, with refractive indexes of 2.45 (GaN) and 2.1 (AlN or ZnO), and a dielectric DBR, with refractive indexes 2.1 (HfO_2) and 1.5 (SiO_2). Each is simulated for 10 and 20 pairs.

interface according to

$$T_{\text{trans}} = \begin{pmatrix} e^{j\beta t\cos\theta} & 0 \\ 0 & e^{-j\beta t\cos\theta} \end{pmatrix}, \qquad T_{\text{inter}} = \frac{1}{t}\begin{pmatrix} 1 & r \\ r & 1 \end{pmatrix}. \tag{3.2}$$

Here $\beta = 2\pi n/\lambda - j\alpha/2$ is the complex propagation constant, t is the thickness of the layer, θ is the propagation angle in the layer relative to the interface normal. t and r are the complex and angle-dependent Fresnel transmission and reflection coefficients. n is the real part of the refractive index of the material and α the absorption coefficient. From the matrix elements of T_{tot}, the reflectivity of the structure is given by

$$R = \left|\frac{T_{\text{tot},12}}{T_{\text{tot},11}}\right|^2, \tag{3.3}$$

and the transmission can also be extracted [85]. By simulating cavities at multiple wavelengths, TMM can also be used to the extract resonance wavelength and the quality factor, which is directly related to the cavity losses, from the reflection dip or transmission peak of the spectrum. Other simulation methods such as the effective index method can be used to obtain additional data such as the lasing threshold material gain [86].

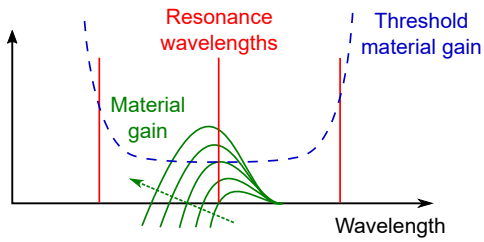

Figure 3.3: Schematic material gain spectra (green) for different carrier concentrations and an example of how the threshold material gain can vary with the spectral position of the resonance wavelength (dashed blue). The green dashed arrow denotes the direction of increased carrier concentration and the red vertical lines show an example of the spectral positions of three different longitudinal modes.

3.2 Gain

The material gain needed in the QWs to compensate for the losses and for the device to reach the lasing threshold is given by

$$g_{th} = \frac{1}{\Gamma}\left(\alpha_i \frac{L}{L_{eff}} + \frac{1}{2L_{eff}} \ln \frac{1}{R_1 R_2}\right), \tag{3.4}$$

where $\Gamma = \Gamma_r \Gamma_t d_a / L_{eff}$ is the total optical confinement factor, d_a is the total thickness of the QWs, L_{eff} is the the effective cavity length, Γ_r is the relative confinement factor that is a measure of how well the antinode of the longitudinal optical field overlaps with the QWs, and Γ_t is the transverse overlap of the field and active region. Furthermore, α_i is the average internal loss in the cavity layers, L is the thickness of the cavity layers, and R_1 and R_2 are the reflectivities of the two mirrors [4].

Figure 3.3 shows schematic material gain spectra for different carrier concentrations together with a curve illustrating how the threshold material gain can vary with spectral position of the resonance wavelength. Assuming that the mode overlap with the active region and lossy layers is constant, the spectral region with low threshold material gain will be determined by the DBR stopband. The material gain will increase and blue shift with increasing carrier concentration but the shape of the curve depends on the active region design. Standard VCSELs have only one longitudinal mode within the part of the spectrum with positive material gain. The material gain experienced by this mode will both be determined by the carrier concentration and spectral position of the resonance, and the material gain that the mode experience needs to reach the threshold material gain to achieve lasing. If the resonance is very close to or below the bandgap, lasing will not be possible, independently of the carrier concentration as the maximum modal gain is too low. If the resonance, on the other hand, is at a too short wavelength, a high carrier concentration is needed to achieve a positive material gain but the maximum

theoretical gain can be large. Depending on the required threshold gain of the laser, different positions of the cavity resonance relative to the material gain spectra may be optimum. Therefore, it is imperative to have good control of the resonance wavelength to achieve low lasing thresholds.

3.3 Resonance wavelength

The resonance wavelength of a VCSEL is sensitive to the cavity length, which is mainly determined by the optical thickness of the epitaxially grown layers between the two mirrors but also by the thicknesses of the DBR layers as the electric field extends into the mirrors. Assuming a cavity consisting of a cavity layer with thickness L and refractive index n between two DBRs, the resonance wavelengths are given by

$$\lambda_m = \frac{2nL_{eff}}{m + 2n(L_{pt}/\lambda_t + L_{pb}/\lambda_b)}, \tag{3.5}$$

where L_{pt} and L_{pb} are the DBR penetration depths, $L_{eff} = L + L_{pt} + L_{pb}$ is the effective cavity length, and λ_t and λ_b are the center wavelengths of the top and bottom DBRs [87]. Thus, the resonance wavelength will both depend on the cavity layer thickness and the DBR center wavelengths. Typically, the cavity thickness and the DBRs are designed such that $\lambda_m = \lambda_t = \lambda_b$, which gives the simpler expression $\lambda_m = 2nL/m$ [87]. As the optical length, nL, of the cavity layer for $m = 1$ is $\lambda/2$, this is often called a 0.5λ cavity and, similarly, for example $m = 5$ corresponds to a 2.5λ cavity. However, the realized resonance wavelength may deviate from the target if there are physical thickness deviations in the growth or optical thickness variations due to refractive index differences, e.g. as a result of deviations in the Al content for AlGaN layers. These effects are discussed in detail for UVB VCSELs in Chapter 5.

3.4 Thermal effects

How fast the temperature of the device will rise with increased pumping is determined by the fraction of the pumping power that is dissipated as heat and by the thermal resistance of the device. The thermal resistance is strongly dependent on the device design and the thermal conductivity of the different materials used. Metals and binary semiconductors typically have high thermal conductivities, while the thermal conductivity of ternary materials are lower (see Fig. 2.3). Furthermore, the thermal conductivity of dielectric materials is even worse. Therefore, especially when using dielectric mirrors, it can be beneficial to use longer cavities to reduce the thermal resistance.

The operating temperature of the device will affect both the resonance wavelength and the gain spectrum. In semiconductor materials, the refractive index typically increase with increasing temperature, leading to a red-shift of the resonance wavelength. Due to

a decreasing bandgap with temperature, the gain spectrum also redshifts with increasing temperature. However, the gain spectrum generally shifts faster than the resonance wavelength and it is, therefore, important to consider operating temperature as well as cold cavity detuning between the gain peak and the resonance wavelength to optimize performance [87]. Additionally, the gain peak is lowered and the carrier leakage from the QWs is increased with temperature, which makes it important to limit self-heating [77, 87].

3.5 Optical guiding

The light in VCSELs is confined vertically by the use of DBRs, but horizontal optical confinement is crucial as well since lateral leakage also has a large impact on the optical losses. If the effective cavity length is longer in the central part of the cavity than in the peripheral parts, i.e. a convex structure, the structure works as a waveguide and reduces lateral leakage. In contrast, an antiguiding concave structure can have significant optical leakage losses [88]. The difference in cavity length between the center and peripheral regions is connected to the effective refractive index differences between the regions according to

$$\frac{\lambda_{\text{center}} - \lambda_{\text{peripheral}}}{\lambda} = \frac{\Delta n_{\text{eff}}}{n_{\text{eff}}}. \tag{3.6}$$

The value of the effective refractive index difference determines if the structure is guiding or antiguiding, what modes that are supported, how temperature-dependent the performance characteristics are, and influences the threshold material gain. A too large optical guiding can lead to high diffraction losses, and to achieve guided single transverse mode VCSELs, both small index differences and small aperture diameters should be used [21, 86, 88, 89].

3.6 Cavity quality factor

The cavity quality (Q) factor is often defined as the ratio of the stored energy in the resonator to the energy losses per cycle. It can also be calculated using the linewidth of the resonances' spectral peak or from the complex eigenvalues of the solutions to the electromagnetic wave equations,

$$Q = \omega_r \frac{W_{\text{cav}}}{P_{\text{loss}}}, \quad Q = \frac{\omega_r}{\Delta\omega} = \frac{\lambda_r}{\Delta\lambda}, \quad Q = \frac{\omega'}{2\omega''}. \tag{3.7}$$

Here ω_r is the resonance frequency, W_{cav} the stored energy, P_{loss} the total loss, $\Delta\omega$ and $\Delta\lambda$ the full width at half maximum (FWHM) of the resonance, and $\omega = \omega' + j\omega''$ the complex eigenfrequency where $\omega' = \omega_r$ and where ω'' represents the losses. All these three methods give very similar results as long as the material dispersion is relatively low [90]. The first can be calculated, if the field profile is know, by integrating the stored

energy in the cavity and by estimating the cavity loss, for example by tuning a gain layer to compensate for the losses. The second can be extracted from simulated or experimentally measured emission, transmission, or reflection spectra. The third is calculated after numerically solving the eigenfrequency problem for the cavity.

Chapter 4

III-nitride vertical-cavity surface-emitting lasers

After the pioneering work by Nakamura, Amano, and Akasaki et al. that led to the first demonstrations of efficient GaN-based LEDs and lasers in 1994-1996 [13–17], research on optoelectronic GaN-based devices increased significantly. Driven by the then highly attractive applications such as high-density optical disc storage and high-resolution printing, a considerable effort was also aimed at VCSELs and within a few years, optically pumped devices were demonstrated. First, at wavelengths just above 360 nm by using a thick GaN cavity as the active material [91] and later at blue wavelengths using InGaN active regions [92]. Despite continued efforts and the successful commercialization of LEDs and edge-emitting lasers, it took until 2008 before the first electrically injected GaN-based VCSELs were realized [18, 19] and there are still today no commercially available III-nitride VCSELs. In the UV range, progress has been even slower, and only small improvements in performance and in expanding the wavelength range has been achieved since the first demonstrations at the end of the 1990s. To better understand the partly slow or limited progress for III-nitride-based VCSELs, this chapter will discuss the challenges related to the reflectors, electrical injection and optical guiding, and it will end with a review of the state of the art for both visible- and UV-emitting VCSELs.

4.1 Reflectors

Unlike the AlGaAs materials system, the III-nitrides suffer from large differences in in-plane lattice constants that puts constraints on the epitaxial growth. Furthermore, large band offsets, poor p-type conductivity, and polarization charges limit the vertical conductivity of III-nitride layer stacks. These challenges have impeded the realization of

electrically conductive III-nitride DBRs with high reflectivity and wide stopbands and instead spurred researchers to investigate multiple different fabrication routes as seen in the many different device schemes that have been successfully demonstrated for III-nitride VCSELs. Figure 4.1 shows schematics of the major schemes for III-nitride VCSELs, but the list would be significantly longer if all their variations would also be depicted. Due to their different benefits and limitations, there is still no obvious superior solution and parallel development remains active.

Even though the first optically pumped III-nitride VCSEL used two epitaxially grown DBRs [91], similar to the typical GaAs-based VCSELs, this was quickly abandoned as the poor p-type conductivity does not only prevent vertical injection but also prevents efficient p-side lateral current spreading. Instead, at least one dielectric DBR is used since these are compatible with an intracavity current spreading layer such as indium tin oxide (ITO). Furthermore, dielectric DBRs are significantly easier to fabricate and typically yields a broader reflectivity stopband and are therefore also used for devices using tunnel junctions (TJs) for electrical injection. Most III-nitride VCSELs can be divided into two broad categories, the hybrid type, which has a p-side dielectric DBR and an n-side epitaxial DBR, and the double-dielectric-DBR VCSEL.

Figure 4.1a-c show examples of hybrid VCSELs and Figure 4.1d,e show examples of double-dielectric-DBR VCSELs. Even though hybrid devices, such as the one shown in Fig. 4.1a, do not need to be bonded to a carrier substrate, it is often done anyway (Fig. 4.1b) to improve the thermal performance. This can also improve the light-extraction as the dielectric DBR typically has a higher reflectivity than the epitaxial DBR, and in these cases, the substrate is usually thinned down and an anti-reflective coating is deposited to further increase outcoupling.

Both the hybrid and the double-dielectric-DBR VCSELs have dielectric p-side DBRs, current confinement and current spreading layers as well as p-side intracavity contacts. For the VCSELs with double-dielectric DBRs, also the n-contact has to be intracavity while the hybrid VCSELs may use n-contacts outside the cavity, as in Fig. 4.1c, if the epitaxial DBR is electrically conductive. The benefits and challenges with electrically conductive DBRs are discussed in detail in Chapter 6.

The typical double-dielectric-DBR VCSEL scheme is shown in Fig. 4.1d. Compared to the hybrid approach, this has the benefit of a wider stopband and an easier achievable high reflectivity (see Fig. 3.2) but it also increases the fabrication complexity as the growth substrate needs to be removed. One other option to achieve a VCSEL with double-dielectric DBRs is to use ELO, see Fig. 4.1e, but this comes with several growth challenges. A scheme that does not belong to either the typical hybrid or double-dielectric classification is the one using a high contrast grating (HCG) either on the n-side (Fig. 4.1f) or the p-side.

Figure 4.2 shows the spectral range for which the different types of injection solutions and mirrors are suitable. In the following, an overview of the different types is given and their suitability in the UV spectral region is highlighted.

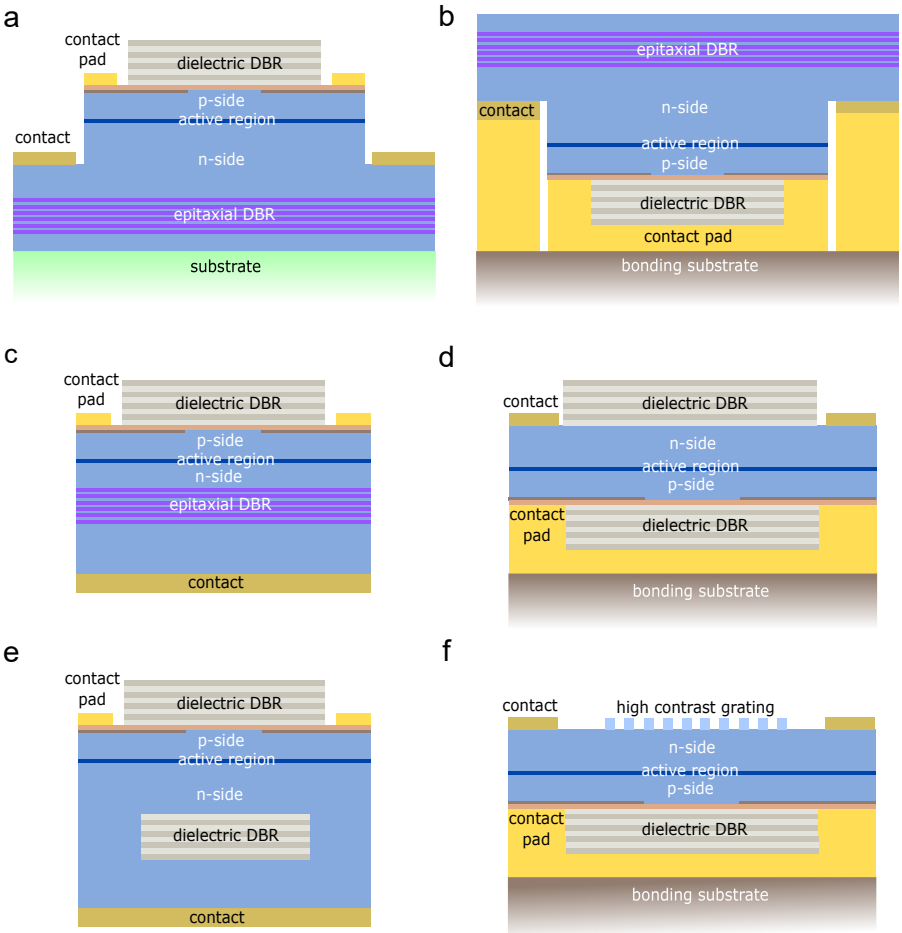

Figure 4.1: III-nitride VCSELs with different reflector schemes. (a) Hybrid VCSEL, (b) bonded hybrid VCSEL, (c) hybrid VCSEL with electrically conductive n-side DBR and back-side contact, (d) double-dielectric-DBR VCSEL, (e) ELO VCSEL, and (f) HCG VCSEL.

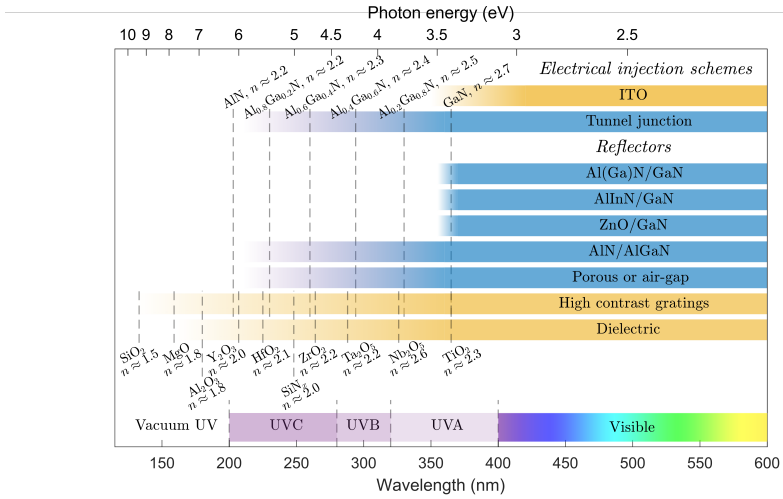

Figure 4.2: Spectral range for which different electrical injection schemes and reflector solutions are suitable. The vertical dashed lines mark approximate bandgaps of different AlGaN compositions and dielectric materials. The given refractive indexes are for a wavelength of 370 nm.

4.1.1 Epitaxial DBRs

The refractive index difference between the two layers in epitaxial DBRs is limited by which layers that can be grown on top of each other without introducing an unacceptable amount of defects. Defects, such as cracks or dislocations, can reduce the DBR reflectivity or lower the quality of other device layers grown on top. For III-nitrides, the lattice mismatch can be significant and the development of III-nitride DBRs demands a trade-off between refractive index contrast, defects, complexity of growth, and in the case of nanoporous or air-gap DBRs, post-growth fabrication. Hence, numerous different types of epitaxial III-nitride DBRs have been demonstrated, most of which can be electrically conductive, but with rather low electrical conductivity as discussed in Chapter 6.

Al(Ga)N/(Al)GaN

There have been many demonstrations of AlGaN-based DBRs, with a wide range of Al contents in the DBR bilayers and grown using both MBE and MOVPE [93–100]. The AlN/GaN combination offers the highest refractive index contrast, allowing for high reflectivity and a wide stopband using as few as around 20 pairs. Consequently, this type of DBR was used in one of the first electrically injected continuous-wave blue-emitting VCSELs [18]. However, due to the large in-plane lattice mismatch of AlN and GaN,

the growth is challenging and the layers may easily crack. Stress management can help against cracking or threading dislocation formation, e.g. by growing directly on SiC without any buffer layer [95], growing on GaN/AlGaN superlattices [100], or using thin strain-compensating interlayers in between the DBR layers [18, 66, 67, 101].

By exchanging one or both of the binary materials with the ternary compound AlGaN, the lattice mismatch decreases and reduces the probability of cracking or threading dislocation generation. The more similar the Al contents of the two layers are, the easier the growth becomes, but at the same time the refractive index contrast is reduced (see Fig. 4.2). Thus, for low contrast Al(Ga)N/(Al)GaN DBRs, it is more challenging to reach high reflectivities and the stopband will be narrower. A 99% reflectivity has been achieved using AlN/GaN [95], but also using $Al_{0.80}Ga_{0.20}N/Al_{0.18}Ga_{0.82}N$ [102] and $AlN/Al_{0.43}Ga_{0.57}N$ [103] DBRs.

For UV VCSELs with emission wavelengths below approximately 360 nm, AlN/GaN DBRs are not longer an option due to the bandgap absorption of GaN, as shown in Fig. 4.2. AlN/AlGaN DBRs can still be useful and Al(Ga)N/AlGaN DBRs have been demonstrated with reflectivities of 99% down to 347 nm [102, 103]. However, despite substantial efforts, there are no demonstrations of AlN/AlGaN DBRs in the UVB or UVC range with a reflectivity of 99% or above [96–99]. The highest reported reflectivity is 98% at 273 nm using either a 25-pair $AlN/Al_{0.65}Ga_{0.35}N$ DBR or a 50-pair $AlN/Al_{0.70}Ga_{0.30}N$ DBR, both with stopband widths below 10 nm [97, 99]. The difficulties in reaching above 99% reflectivity in this spectral range stem from the small achievable refractive index difference that shrinks as the wavelength becomes shorter and a higher Al content is needed to reduce absorption.

AlInN/GaN

By using an In content of approximately 18%, it is possible to grow AlInN lattice-matched to GaN (see Fig. 2.1) and this is used to grow close to strain-free AlInN/GaN DBRs. Although the refractive index contrast is only approximately half that of AlN/GaN, which means that around 40 DBR pairs are needed to reach a reflectivity above 99%, the low strain may allow for crack-free growth. However, due to primarily the large difference in optimum growth temperatures of AlN and InN, the growth of AlInN is hampered by phase-separation, slow growth rates, generation of threading dislocations, and In incorporation having a high sensitivity to growth conditions [104–106]. Despite this, AlInN/GaN DBRs with reflectivities above 99% have been achieved, mainly using MOVPE, with the first demonstrations at École polytechnique fédérale de Lausanne (EPFL) [94, 107]. EPFL also used their DBR in an electrically injected blue-emitting VCSELs [108]. In the last few years, AlInN/GaN has arguably been the most successful III-nitride epitaxial DBR, primarily due to the work by Meijo University and Stanley Electric, which have improved the DBR quality by, e.g., the use of in-situ curvature monitoring and GaN cap layers grown at similar conditions that are used for AlInN growth [105, 106]. Furthermore, they have incorporated their AlInN/GaN DBRs in blue-emitting

VCSELs [21, 109] showing record-high output powers. Recently, also Nichia Corporation demonstrated blue and green VCSELs with record-high wall-plug efficiencies using the same type of DBRs [22].

Unfortunately, the usefulness of AlInN/GaN DBRs in the visible and UVA does not transfer to shorter wavelengths. Although a reflectivity above 99% has been achieved down to approximately 340 nm using an $Al_{0.85}In_{0.15}N/Al_{0.20}Ga_{0.80}N$ structure [110], the lattice matching benefits mostly disappear if used in shorter wavelengths devices. AlInN and AlGaN can still be grown lattice-matched to each other but much of the AlInN/GaN benefit comes from being lattice-matched to the GaN substrate or template. In the UVB and UVC, AlN substrates or templates are usually used and AlInN/AlGaN will no longer provide any significant advantage over AlN/AlGaN.

Nanoporous or air-gap DBRs

Electrochemical etching can be used to selectively porosify or completely remove highly n-doped III-nitride layers [111, 112]. In Chapter 5, the principles of electrochemical etching and its use in lifting off UV structures are explained. However, many groups have also used this process to create air-gap [27] or nanoporous DBRs [113–117]. A nanoporous layer has an effective refractive index layer between that of the semiconductor and air, which depends on the degree of porosity. A GaN structure with alternating doped and undoped layers can be turned into nanoporous or air-gap DBRs by carefully selecting doping levels, etching voltage and layer thicknesses. These DBRs are relatively easy to grow and have a potential for a high refractive index contrast. However, the porosity may be sensitive to process conditions or sample inhomogeneities, it demands additional processing steps, and for high porosities and especially air-gap DBRs, the structural stability may be compromised. Large pores could also lead to losses due to optical scattering. Nevertheless, reflectivities above 99% have been demonstrated using nanoporous DBRs in the visible spectral region and these have been used in electrically injected blue-emitting VCSELs where the DBRs' anisotropy also can be used for polarization pinning [118, 119]. Furthermore, $Al_{0.05}Ga_{0.95}N$ nanoporous DBRs with above 99.5% reflectivity and an air-gap DBR have been incorporated into optically pumped UVA-emitting VCSELs [27, 120]. Air-gap DBRs may also be formed using wet etching of AlInN in hot nitric acid, but the chemical stability of AlInN gives etch rates of only around 200 nm/h [121], compared to electrochemical etching with etch rates that can be in the order of 10 µm/min [112].

To be used as reflectors in the UVB and UVC, high Al-content layers are needed. Complete etching of up to 50% and porosification up to 60% Al-content AlGaN have previously been demonstrated [112, 122, 123], and we have recently seen that it is possible to porosify AlGaN with at least 76% Al content as shown in Fig. 4.3. A porous AlGaN DBR is, thus, a relatively promising option for deep-UV DBRs. Reflectivities as high as 93% have been reported at 276 nm from a porous $Al_{0.47}Ga_{0.53}N$ DBR [124] and 89% at 324 nm from a porous $Al_{0.6}Ga_{0.4}N$ DBR [122]. However, reaching reproducible

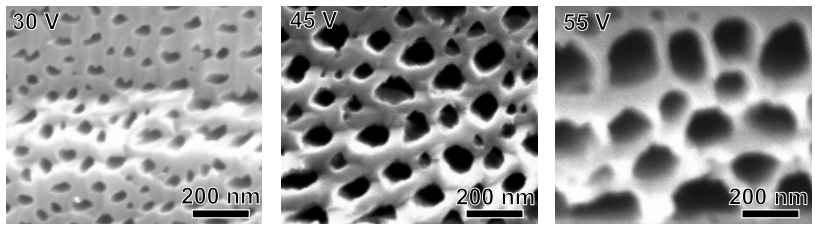

Figure 4.3: Cross-sectional view scanning electron microscopy (SEM) images of $Al_{0.76}Ga_{0.24}N$ with Si-doping of approximately $3 \times 10^{18}\,cm^{-3}$, porosified using electrochemical etching in 0.3 M HNO_3 at 30, 45, or 55 V.

reflectivities of 99% using porous AlGaN DBRs will be challenging as AlGaN suffers from more sample inhomogeneities than GaN. Furthermore, shorter wavelengths will be more sensitive to scattering from DBR pores which could lead to increased optical losses.

ZnO/GaN

An alternative to pure III-nitride DBRs is a ZnO/GaN DBR. ZnO/GaN has the benefit of a similar refractive index contrast as AlN/GaN but at the same time a smaller in-plane lattice-mismatch when grown on the c-plane, 1.9% instead of 2.5%. ZnO has a similar bandgap as GaN and the wavelength range that ZnO/GaN DBRs can be used for extends into the UVA. Furthermore, the ZnO/GaN material pair has several beneficial electrical properties, as discussed in Chapter 6, which makes it ideal for electrical injection through the DBR. In 2016, Adolph et al. demonstrated the first ZnO/GaN DBRs grown using hybrid PAMBE, where both the ZnO and GaN were grown in the same chamber, reaching reflectivities up to 77% [125]. However, the development of the growth of these heterostructures is still in its infancy, and more work is needed to improve the optical quality to be able to reach 99% reflectivity.

4.1.2 Dielectric DBRs

Compared to epitaxial DBRs, the fabrication of dielectric DBRs is less complex. The materials used are often amorphous or poly-crystalline and are deposited by sputtering or evaporation. Because of this, there is no need for lattice matching, and the two dielectric materials of the DBR can be chosen from a wide range of available oxides but also e.g. AlN and SiN_x, as shown in Fig. 4.2. The bandgap energies and refractive indexes (at a wavelength of around 370 nm) are taken from Refs. [126–138] except for the bandgap of HfO_2 and the refractive index of SiO_2 and HfO_2 which are from our own measurements. It is important to note that the refractive index varies with wavelength, especially close to the bandgap. Furthermore, the dielectrics' material properties strongly depend on deposi-

tion conditions and the values in Fig. 4.2 should therefore be taken as rough estimates. In general, SiO_2 is used as the low-index material because it has a very large bandgap, and thus also a low refractive index, and is straightforward to deposit using several different methods. For the high-index material, SiN_x, HfO_2, ZrO_2, Ta_2O_5, Nb_2O_5, and TiO_2 have been successfully implemented in blue VCSELs [108, 109, 139–142].

For short UV wavelengths, there are fewer transparent dielectric materials to choose from. Hafnium dioxide has both a large enough bandgap and refractive index to allow for the fabrication of HfO_2/SiO_2 DBRs with above 99% reflectivity in the UVB and the part of the UVC spectrum that is most interesting for sterilization applications (250-280 nm). Nevertheless, HfO_2 and other materials can suffer from deposition condition dependent sub-bandgap absorption, and our work on reducing this is presented in Chapter 5.

Although dielectric DBRs typically are superior to epitaxial DBRs in terms of ease of deposition, stopband width, and number of pairs needed, they can add additional device processing challenges. When an n-side dielectric DBR is used, either ELO or substrate removal is needed.

Substrate removal techniques

There are numerous techniques that have been used to remove the growth substrate of III-nitride devices. Laser lift-off is used extensively in fabrication of blue LEDs [143] but has also been explored for III-nitride VCSELs [19, 142, 144]. It uses a high intensity laser beam, directed at the backside of the sample, that is absorbed at the GaN/sapphire interface to thermally decompose the GaN and in this way releases the GaN film from the sapphire substrate. For VCSELs, it is combined with a chemical-mechanical polishing step to shorten the cavity length and achieve a smooth surface. Laser lift-off can lead to cracks in the film due to stress release during substrate removal, a problem that is especially pronounced for film thicknesses of a few micrometers or less [145]. Furthermore, laser lift-off is not compatible with free-standing GaN substrates, which is used in the top-performing GaN-based VCSELs [21, 22, 139]. Instead, when using GaN substrates, the entire thickness needs to be thinned down using polishing. This leads to poor thickness control and, in turn, poor wavelength control, which impedes mass production [22, 139, 146].

For AlGaN-based devices, the issues with cracking after laser lift-off worsens and rigid Al-residues can form on the exposed surface [147]. Laser lift-off has been used to form double-dielectric-DBR microcavities for wavelenghts around 300 nm but the resulting root-mean-square (RMS) roughness of 20 nm or higher prevented lasing [148, 149]. In these demonstrations, chemical-mechanical polishing was not used after lift-off as it is especially challenging for highly strained AlGaN-based devices due to the bowing of the sample after release. In a later demonstration, post lift-off polishing was employed and it resulted in very large variations in cavity length [149].

More promising is the use of electrochemical or photoelectrochemical etching. Electrochemical etching is discussed more in Chapter 5, and photoelectrochemical etching is

a similar process in which the sample is exposed to above bandgap light illumination to increase the carrier concentration and in this way enhance the etching. In short, these methods rely on the selective removal of a layer with high carrier concentration placed between the device layers and the substrate, where the carrier concentration is controlled through doping or illumination. These methods have the benefits of an excellent thickness control set by the epitaxial growth, allowing for the reuse of expensive GaN or AlN substrates, and can be tuned to achieve smooth surfaces. Additionally, electrochemical etching is compatible with high Al-content III-nitride device fabrication, including VCSELs. Photoelectrochemical etching has been used to create non- and semipolar blue-emitting VCSELs [150–153] and electrochemical etching enabled the demonstration of the first optically pumped UVB VCSEL, as discussed in Chapter 5.

Epitaxial lateral overgrowth

High-quality active regions can not be grown directly on dielectric materials, but using ELO, it possible to benefit from the high optical performance of dielectric DBRs without the need for complex substrate removal. Nevertheless, the epitaxial growth becomes more complex. First, the dielectric DBR is deposited and patterned on the III-nitride substrate. Next, the epitaxial growth of GaN is initiated and it will mainly start at the openings between the DBR stacks. After a while, the growth will also progress laterally and eventually bury the DBR mesa, as seen in Fig. 4.1e. Sony used ELO in their first blue-emitting VCSEL demonstration [140] but has since then instead focused on devices fabricated using chemical-mechanical polishing [139], perhaps due to the complexity of ELO growth. Furthermore, ELO may be difficult to use for short cavity VCSELs due to the ratio between the vertical and lateral growth rate and can lead to problems with cavity length control [154]. ELO of AlGaN can lead to different alloy compositions on different facets and ELO of high Al-content AlGaN or AlN is typically done at high temperatures (>1150°) and can suffer from slow lateral growth rates and parasitic growth on the mask [155, 156]. Thus, successful overgrowth of DBRs is likely more challenging for AlGaN devices than for GaN.

4.1.3 High contrast gratings

HCGs are periodic structures with features of near sub-wavelength size. By controlling the period, thickness, and duty-cycle, very high reflectivities can be achieved. HCGs can also be used for polarization and transverse mode control and post-growth wavelength setting of multiple wavelengths across one sample using a single patterning step [157]. Recently, the first electrically injected HCG GaN-based VCSEL was demonstrated, using a TiO_2 grating on GaN [142]. Moreover, HCGs can take many forms, e.g. as air-suspended gratings or monolithic gratings that are etched directly in the the III-nitride cavity layer [88, 158, 159]. There is nothing fundamental hindering the use of HCGs for VCSELs covering the entire UV range. However, due to the very small process toler-

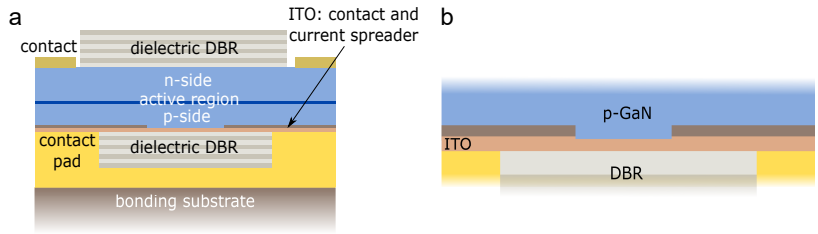

Figure 4.4: (a) Schematic cross-sectional view of a VCSEL using ITO as p-side contact and current spreader. (b) Magnified view of the aperture region where the brown layer is an insulating dielectric or passivated GaN.

ances of the sub-wavelength structures, it is challenging to achieve 99% reflectivity. This becomes increasingly more difficult the shorter the target wavelength is and is further complicated by the lack of high bandgap materials with high refractive index. Due to the complex fabrication, HCGs are usually used together with a traditional epitaxial or dielectric DBR, as shown in Fig. 4.1f.

4.2 Electrical injection schemes

It took over a decade from the first optically pumped III-nitride VCSEL [91] until the first demonstrations of electrically injected devices [18, 19]. The slow progress did not only stem from difficulties in achieving the higher reflectivity mirrors needed to sustain lasing from electrically injected cavities for which the achievable gain is typically lower than in optically pumped devices. It also arose from challenges related to the low electrical conductivity of p-GaN. The low conductivity prevents contacts directly to the p-GaN outside the aperture of the VCSEL, as the lateral current spreading will be insufficient. Instead, two different methods that support p-side current spreading have been implemented.

4.2.1 Indium tin oxide

The first and so far most widely used solution for electrical injection of III-nitride VCSELs is indium tin oxide. ITO, which is a transparent conductive oxide, has for a long time been used for transparent p-contacts to p-GaN. In VCSELs, ITO is used both as a p-contact and a p-side current spreader, as shown in Fig. 4.4. Current confinement can be accomplished by preventing electrical contact between the ITO and p-GaN outside the aperture, either by using an insulating oxide or by insulating the p-GaN using ion implantation or intentional dry etching damage [18, 19, 21, 150]. Note that the ITO layer is inside the cavity and adds additional optical losses. Although the bandgap lies below 350 nm, ITO has a significant absorption tail that extends into the blue spectral regime

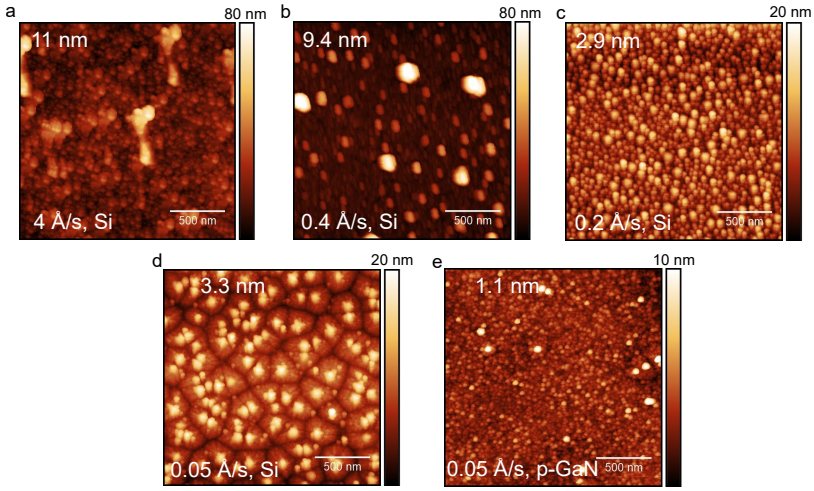

Figure 4.5: Atomic force microscopy (AFM) images of 30-nm thick e-beam deposited single-layer ITO on (a-d) Si using different deposition rates and (e) on p-GaN. The value at the top left corner is the RMS roughness over the $2 \times 2\,\mu$m. scan area.

with absorption coefficients typically above $1000\,\mathrm{cm}^{-1}$ [160]. To reduce the absorption, it is important to align the ITO layer to an optical node by using a dielectric spacer before the DBR. Furthermore, there is a trade-off between optical loss and lateral current spreading in the ITO-layer, and the thicknesses used are commonly 20-30 nm.

To reduce optical losses, it is also important that the surface of the ITO is smooth because roughness may propagate into the DBR on top and result in scattering at all interfaces. Leonard et al. showed that it is possible to get a roughness of 1 nm or less using two temperature steps during electron-beam deposition [160]. However, my experiments show that our 5 nm/25 nm room temperature/300°C ITO layer, also e-beam deposited, had more than twice the absorption compared to a single 30-nm layer deposited at 300°C, based on transmission and reflection measurements after a post-deposition 8-minute annealing at 600°C in nitrogen atmosphere. Instead, lower roughness with maintained low absorption (below $3000\,\mathrm{cm}^{-1}$ at 420 nm) and resistivity was achieved for single layers using lower deposition rates, as shown in Fig. 4.5. The morphology also depends on the substrate and ITO deposited on different p-GaN samples had RMS roughnesses between 1 and 2 nm.

ITO has been used in microcavities emitting at 375 nm where the high absorption of $7000\,\mathrm{cm}^{-1}$ is likely one of the reasons why the device did not lase [27]. It might find use in near UVA VCSELs, but for VCSELs emitting at shorter wavelengths than 370 nm, tunnel junctions seems to be the best, if not the only, option.

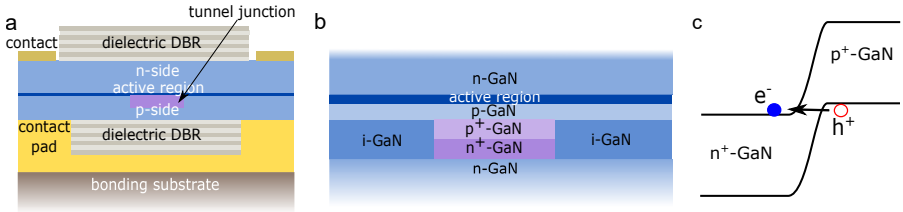

Figure 4.6: (a) Structure of a VCSEL using a buried tunnel junction for electrical injection. (b) Magnified view of the buried tunnel junction region. (c) Band diagram illustrating the tunneling processes in a reversed biased GaN homojunction.

4.2.2 Tunnel junctions

More recently, tunnel junctions have emerged as an alternative to ITO for electrical injection in III-nitride VCSELs. As depicted in Fig. 4.6, an n-(Al)GaN layer is grown on top of the p-(Al)GaN to support p-side current spreading, and electrons and holes are generated at the TJ. The generation is achieved by reverse biasing of a pn-junction that is doped high enough to give a sufficiently narrow depletion region and allow for significant tunneling when the n-side conduction band and p-side valence band align. To enhance tunneling and reduce the voltage penalty of the TJ, it is common to make use of an InGaN interlayer between the p- and n-GaN, or in the case of AlGaN-devices, a GaN interlayer. The smaller bandgap lowers the energy barrier for tunneling and the polarization charges decrease the depletion width [161]. For VCSELs, there is a need to confine the current by insulating the area outside the aperture before growthing the top n-GaN. This can be done by etching away the high-doped layers, creating a buried tunnel junction (BTJ), or by ion implantation.

The first TJ III-nitride VCSEL was demonstrated in 2015, when Leonard et al. implemented a hybrid MOVPE-MBE grown TJ in a non-polar VCSEL in which the aperture was defined using ion implantation [162]. Since then, TJ VCSELs grown using only MOVPE on c-, s- and m-planes have all been demonstrated, including devices with BTJs and InGaN interlayers [151, 152, 162–164]. The output powers are still lower than the best demonstrations using ITO by almost an order of magnitude [21, 151], but the results hold promise for high-performing devices not limited by the ITO absorption and with improved reliability [163].

Unlike ITO, there is no fundamental obstacle that limits the use of TJs for UV VCSELs. However, it becomes increasingly more challenging to grow low-resistance TJs for shorter wavelengths. This is due to the larger bandgap of AlGaN and increased difficulties with p-doping. Despite these challenges, there have recently been significant improvements in AlGaN TJs and both homojunctions with Al-content up to 58% and TJs with (In)GaN interlayers have been demonstrated, all the way down to UVC wavelengths [165–169]. The best results have been achieved using interlayers. Ohio State Univer-

sity has shown TJ LEDs with emission wavelengths from 365 nm to 257 nm with less than $2 \times 10^{-3}\,\Omega\,\mathrm{cm}^2$ differential series resistance and sustaining up to $1\,\mathrm{kA/cm}^2$, using MBE-grown TJs with a 4 nm thick InGaN interlayer with approximately 20% In content [169]. The Technische Universität Berlin has demonstrated fully MOVPE-grown LEDs emitting at 268 nm having 8 nm GaN interlayers and a differential series resistance of approximately $5 \times 10^{-3}\,\Omega\,\mathrm{cm}^2$ at $350\,\mathrm{A/cm}^2$ [166]. As the focus so far has been on LEDs and to some extent edge-emitting lasers, there is less data on the surface smoothness and exact amount of optical absorption in AlGaN TJs. Nevertheless, a 2 nm InGaN interlayer has been used for blue-emitting VCSELs and it was shown that despite the high absorption of the interlayer, the small thickness allows for efficient alignment to an electric field minimum in the cavity. Lower modal absorption can be achieved compared to using an ITO contact, although the alignment tolerance is smaller [164]. The recent AlGaN TJ results hold great promise, but significant efforts are still needed for AlGaN TJs to meet the tough requirements for the integration into VCSELs. These include reaching an RMS roughness close to or below 2 nm, round-trip absorption of less than 1% when placed in an optical node, sustaining current densities of around $10\,\mathrm{kA/cm}^2$ and having differential resistances below $10^{-3}\,\Omega\,\mathrm{cm}^2$ (1 V per $1\,\mathrm{kA/cm}^2$).

4.3 Optical guiding

Lateral optical losses due to insufficient waveguiding can be detrimental to the VCSEL performance. Hashemi et al. showed that many of the early III-nitride VCSELs structures actually had antiguided cavities resulting in high threshold material gain [88, 170]. Antiguiding can be avoided by using convex structures in VCSELs, as shown in Fig. 4.4b, and can be realized by either an etched shallow relief or BTJ. Ion-implantation can also be used to reduce the refractive index and provide lateral confinement [21, 89, 150], but can also lead to increased absorption losses in the implanted regions.

For very long cavities and small apertures, diffraction losses can become considerable. Sony Corporation has managed to solve this problem in their VCSELs with double-dielectric DBRs fabricated by chemical-mechanical polishing in which they use one curved mirror to form cavities with reduced diffraction losses [139].

It is common for III-nitride VCSELs to show a stochastic spatial intensity distribution that deviate significantly from the theoretical Laguerre-Gaussian modes expected for circular-symmetric resonators [118, 150, 171–173]. The origin of this type of filamentary lasing is not yet fully understood but could be a result of lateral variations in modal gain or effective cavity length, stemming from variations in material gain, absorption, alloy composition, carrier injection, and cavity thickness. For AlGaN-based VCSELs, the lasing wavelengths are shorter and the material inhomogeneities are larger, making these issues more pronounced than for GaN-based devices, as discussed in Chapter 5. Intentional index guiding has been shown to reduce filamentation [173, 174] but optically pumped devices often lack any physical apertures for optical and carrier confinement and

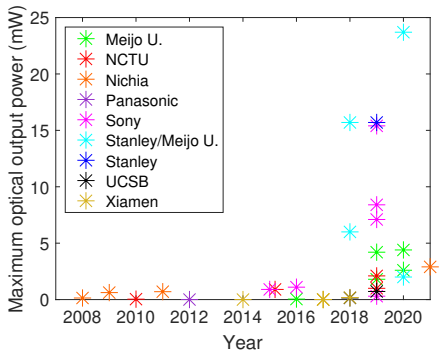

Figure 4.7: Output power versus reported year for electrically injected continuous-wave blue-emitting VCSELs at room temperature [19–22, 109, 139–141, 146, 151, 163, 164, 175–187].

are mainly optically guided by differences in gain and temperature resulting from the pumping and sample inhomogeneities.

4.4 State-of-the-art III-nitride VCSELs

The performance of blue-emitting VCSELs has advanced tremendously in just a couple of years as is obvious from Fig. 4.7, which shows the reported output powers of electrically injected continuous-wave VCSELs emitting at blue wavelengths at room temperature versus the year of the demonstration. Perhaps the most impressive results are by Stanley Electric and Meijo University, who by using an AlInN/GaN hybrid-type VCSEL with a 5 nm deep etched relief to define the 7 µm aperture and an ITO p-contact have achieved record output powers of 23.7 mW at room temperature. These devices have wall-plug efficiencies of 10%, differential quantum efficiencies of 43.6%, threshold currents of 8.2 mA (21 kA/cm^2), and lased up to 140°C with output powers above 3 mW. Furthermore, single-mode lasing up to 7 mW was achieved using 3.3 µm apertures for devices with threshold currents of 1.4 mA (16 kA/cm^2) [21]. The same groups have used similar structures but with SiO_2-defined apertures to demonstrate in-phase supermode operating VCSELs with very small 2.8° beam-divergence using a floral-patterned aperture [184], 1.2 W output power 16x16 VCSEL arrays [188], and a 2.6 mW output power VCSEL having an electrically conductive AlInN/GaN mirror and a backside n-contact [185]. Furthermore, Nichia Corporation has reported hybrid-type AlInN/GaN DBR VCSELs with record wall-plug efficiencies of 13.6% for devices emitting at blue wavelengths and 3.7% for green-emitting devices. These single-mode blue and green VCSELs have threshold currents of 1 mA (3.2 kA/cm^2) and 2.8 mA (14.3 kA/cm^2) and output powers of 3 mW and 1.5 mW, respectively. The blue devices had a yield of more than 80% over a 2″ wafer

and survived 1000 hours of continuous operation at room temperature. [22].

Also VCSELs with double-dielectric DBRs have recently shown great improvement in performance where Sony Corporation has demonstrated a 4.0 mA (8.0 kA/cm^2) threshold current and 15.4 mW output power multimode VCSEL using 20-µm thick cavity and a curved mirror. A single-mode 1.2 mA (9.5 kA/cm^2) threshold and 7.1 mW output power device was also demonstrated by tuning the aperture diameter and radius of curvature of the mirror [20]. Furthermore, Sony has used the same principle to demonstrate a green-emitting semipolar VCSEL with an output power of around 80 µW. Despite the still relatively low output power, they used it to show a proof-of-concept all-VCSEL-based white light source by combining it with blue- and red-emitting VCSELs [189]. Before Sony and Nichia, only Xiamen University had achieved continuous-wave green lasing, in their case using InGaN quantum-dot active regions [190].

Notably, the best results achieved were on free-standing GaN substrates [20–22, 146]. Free-standing GaN has low defect densities but the wafers are typically expensive and limited in size compared to GaN-on-sapphire templates. Although there are not many reports on the long term stability of III-nitride VCSELs, low-defect-density substrates as well as TJ contacts instead of ITO have been reported to increase device lifetimes [146, 163]. Low-defect nano- and microstructures, such as the microprisms discussed in Chapter 7, could potentially provide an alternative to the still expensive free-standing GaN substrates.

4.4.1 UV-emitting

As may be obvious to the reader after reaching this far in the chapter, UV VCSELs share most of the challenges of blue-emitting devices but also suffer from additional obstacles. It is telling that the challenges with AlGaN materials prevented electrically injected lasing even for edge-emitting lasers until 2019 when pulsed injection UVB and UVC laser diodes were demonstrated [61, 199, 200]. All UV VCSEL demonstrations are summarized in Fig. 4.8 where filled circles denote electrically injected devices and open circles optically pumped VCSELs. The only electrically injected VCSEL is a UV-blue-emitting device with a 6 µm long cavity length. A few of the lasing longitudinal modes are in the near-UV where the ITO absorption still was low enough to allow for lasing [141]. For even shorter wavelengths, the high absorption of ITO will be a severe limitation and probably was one of the reasons why resonant-cavity LEDs with emission around 370 nm did not lase [201, 202]. Zhang et al. used a TJ to drive a VCSEL structure emitting around 370 nm, but the device broke down before lasing was achieved [120]. Nevertheless, the recent progress in AlGaN TJs suggest they can become a viable solution for current injection in UV VCSELs.

In comparison, there have been more success for optically pumped devices and several groups have achieved lasing for wavelengths below the bandgap of GaN. However, this was achieved as early as in the mid 1990s [91], and before 2020, little progress had been made to extend the emission to shorter wavelengths. Previously, only one report had

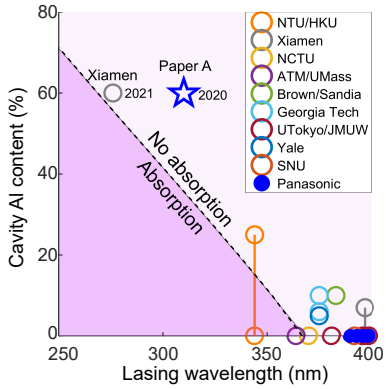

Figure 4.8: Al content in the cavity versus lasing wavelength for UV VCSELs [27, 91, 92, 120, 141, 191–198]. Open circles mark optically pumped devices and connected markers indicate devices with a range of Al contents in the thick cavity layers. The dark region corresponds to wavelengths above the bandgap of AlGaN.

claimed lasing below 360 nm [191]. In that demonstration, they optically pumped dry-etched micropillars consisting of an $Al_{0.49}Ga_{0.51}N/Al_{0.16}Ga_{0.84}N$ DBR and a HfO_2/SiO_2 DBR sandwiching an $Al_{0.25}Ga_{0.75}N$/GaN superlattice cavity with AlInGaN QWs. Although lasing was claimed, the emerging emission peak did not completely dominate the emission above threshold and the linewidth of the peak was as wide as 2 nm. Furthermore, there is no discussion on how the large amount of GaN in the cavity, which is highly absorptive at the 344 nm emission wavelength, is compatible with lasing. Thus, the claim of lasing can be questioned.

To realize UVB and UVC lasing, there is a need to increase the Al-content in III-nitride device layers as the cavity otherwise would be highly absorptive. Until our demonstration of the first high Al-content VCSEL presented in Paper A, there were no demonstrations of either UVB or UVC VCSELs. This was due to the problems with achieving high reflectivity III-nitride DBRs with large Al content for use in hybrid-type devices and the difficulties with lifting off high Al-content AlGaN layers for VCSELs with double-dielectric DBRs. Recently, after our UVB VCSEL demonstration, Xiamen University reported a device having a weak lasing peak at 276 nm. However, the cavity length of the double-dielectric-DBR VCSEL after laser lift-off and chemical-mechanical polishing was 140-700 nm [198]. Therefore, it is doubtful that lasing occurred in more than a selected area where the spectral position of the cavity mode by chance overlapped sufficiently with the gain spectra. In the next chapter, I will discuss how we realized the UVB VCSELs and the importance of the superior cavity length control that is possible to achieve using electrochemical etching.

Chapter 5

Optically pumped ultraviolet vertical-cavity surface-emitting lasers

Methods to embed high Al-content AlGaN layers between two high-reflectivity DBRs are needed to realize VCSELs in the UVB and UVC spectral region. As will be explained in this chapter, it is possible to use electrochemical etching, which can provide precise cavity thickness control and smooth surfaces, to underetch high Al-content AlGaN layers for use in double-dielectric-DBR VCSELs. The AlGaN epitaxial structures in this work were grown using MOVPE by Johannes Enslin at the Technische Universität Berlin on substrates provided by the Ferdinand-Braun-Institut in Berlin.

5.1 Electrochemical etching and bonding

Electrochemical etching is a doping-selective method to etch semiconductors. It relies on bias voltage dependent anodic oxidation of a semiconductor surface in an electrolyte followed by dissolution of the oxidized material. Figure 5.1a shows the band diagram of the interface between the electrolyte and the semiconductor. The interface behaves as a Schottky junction with a band alignment at equilibrium determined by the semiconductor Fermi level and electrolyte redox level [203, 204]. When a voltage is applied, the band bending will increase, and when it is large enough, holes will be generated in the space-charge region either through Zener tunneling of electrons from the valence to conduction band or by impact ionization during avalanche breakdown. Tunneling is considered the main mechanism for hole generation in narrow depletion region materials such as highly n-doped GaN, while the influence of impact ionization is more important

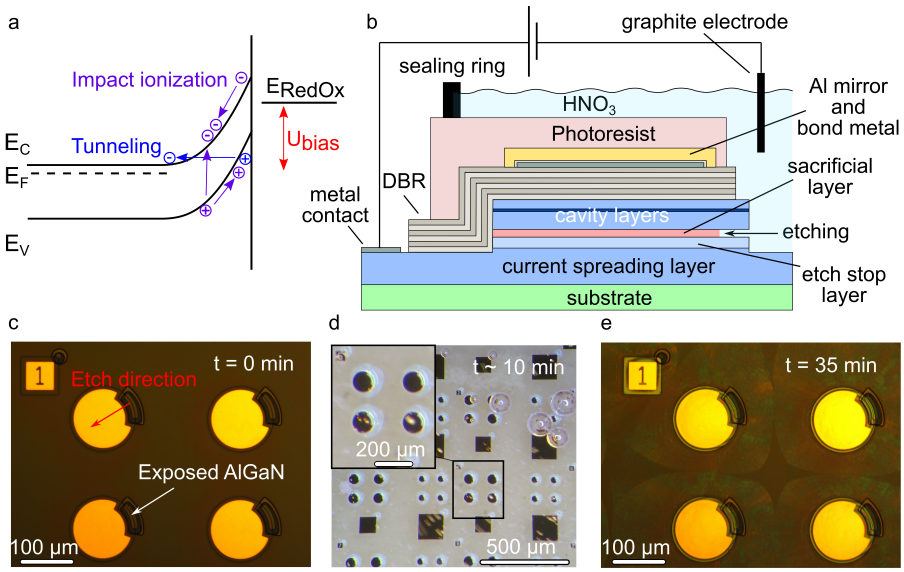

Figure 5.1: (a) Schematic band diagram of a biased semiconductor-electrolyte interface. (b) Schematic of the electrochemical etching of a sacrificial layer to release a VCSEL structure from its substrate. (c) Optical microscope image of four mesas before etching. (d) In-situ optical microscope image after about 10 minutes of etching. (e) Optical microscope image after 35 minutes of etching.

for wider depletion regions and might be relevant for lower doped and larger bandgap AlGaN. The generated holes will accumulate at the interface and facilitate oxidation of the semiconductor surface. The electrolyte, often an acid and in our case HNO_3, dissolves the oxidized material. In the case of electrochemical etching of III-nitrides, the byproducts at the sample are dissolved metal ions and nitrogen gas, and at the cathode hydrogen gas. Also oxygen gas may be formed by the unintended electrolysis of water [112, 116, 204, 205].

Depending on the material properties and etching parameters, different etching regimes can be observed, as shown in Fig. 5.2. The most important factors are bias voltage, n-doping, and, in the case of AlGaN, Al content. With increasing bias voltage and n-doping, the etching regime will transition from no etching, to porosification, and eventually electropolishing, i.e. complete removal of the semiconductor [116, 204, 205]. For higher Al content, higher voltages are needed to reach the electropolishing regime [112].

To create a UV VCSEL, the VCSEL structure is underetched as shown in Fig. 5.1b where a sacrificial layer that has higher doping and lower Al content than the surrounding

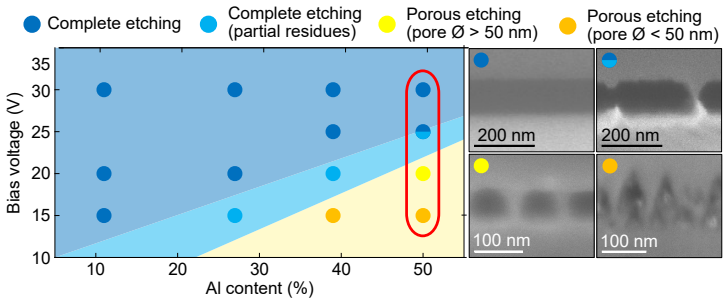

Figure 5.2: Etching regime of AlGaN as function of etching voltage and Al content. The mark in red shows the samples that are displayed in the SEM images to the right. Figure adapted from Ref. [112].

layers is selectively etched away. A sealing ring is used to prevent the acid from reaching the metal contact used for biasing. In Fig. 5.1c and Fig. 5.1e, optical microscope images of four devices are shown before and after a 35 minute long etching step. Figure 5.1d shows an in-situ microscope image taken after approximately 10 minutes of etching when the 120 µm-diameter circular mesas have just been completely underetched but where the larger square mesas are only partially released. The etching starts at an exposed mesa edge and progresses laterally until the device is completely released, as seen in Fig. 5.1e on the color shifts at the mesa edges. The unidirectional etching prevents etch fronts from merging in the mesa center, which would leave residues of the sacrificial layer. Below the sacrificial layer, there is an etch stop layer with lower doping and below the etch stop layer, a current spreading layer with intermediate doping is used to spread the current during the electrochemical etching. Depending on the bias voltage, the current spreading layer may become porosified, as seen in Fig. 5.1d where the bright etch fronts extend outside the mesas and in Fig. 5.1e where the etch fronts in the current spreading layers from the different mesas have merged. The mesas are held in place after electrochemical etching and resist stripping by the DBR that wraps around the mesa sidewalls. These DBR supports are broken during thermocompression bonding which is followed by a second DBR deposition to form the final VCSELs.

Another possibility is to bond the devices before electrochemical etching, instead of after. However, having the carrier substrate covering the top of the chip during etching can reduce the electrolyte access to the devices and increase the voltage drop in the acid. In addition, gas formed during the electrochemical reaction is trapped between the chips and can further slow down the etching or exert a mechanical force on the bonded chips. These effects can result in inhomogeneous and insufficient etching, especially in the center of the sample, which results in poor transfer yield as seen when comparing Fig. 5.3a, which shows bonding results for devices bonded before etching, and Fig. 5.3b where the devices

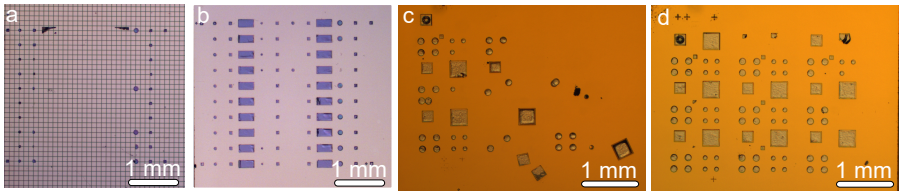

Figure 5.3: Optical microscope images of GaN membranes bonded either (a) before electrochemical etching or (b) after. (c,d) Optical microscope images of bonded UVB VCSEL structures underetched using different types of sacrificial layer.

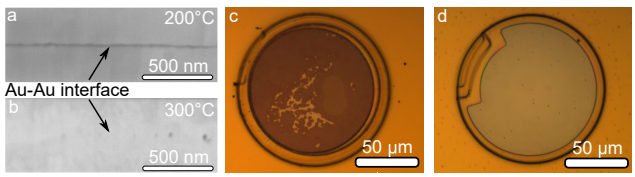

Figure 5.4: SEM images of an Au-Au interface after thermocompression bonding at (a) 200°C and (b) 300°C. (c,d) Optical microscope images of UVB VCSELs after the final DBR deposition. (c) Without a SiO_2 layer between the Al mirror and bonding metals. (d) With a SiO_2 layer between the Al mirror and bonding metals.

were bonded after etching. The disadvantage with bonding after sacrificial layer removal is that the device geometry and DBR support must be optimized to prevent loss of mesas during etching. The optimal design will depend on the epitaxial structure and etching parameters and this is seen from the difference in yield for the samples in Fig. 5.3c and Fig. 5.3d, which only differ in the design of the sacrificial layer used.

The SEM images in Fig. 5.4a and Fig. 5.4b show the importance of using temperatures above 200°C to get an Au-Au thermocompression bonding interface with few voids. However, when using an Al-mirror on the first DBR to boost the power reflectance for the pump beam, the Al can alloy with the Ti and Au bonding metals. Alloying can happen either during bonding or when the samples are unintentionally heated during the top DBR sputtering and is observed as a color shift of the metal after processing. Nevertheless, by adding a SiO_2 layer between the Al and bonding metals, the Al remains intact. This is seen when comparing the VCSEL without this layer in Fig. 5.4b, which has a dark color, with the VCSEL with the SiO_2 layer in Fig. 5.4c, which has the brighter color of the as-deposited Al.

When removing the substrate, it is crucial to achieve smooth etched surfaces to minimize optical scattering losses. Figure 5.5 shows the roughness of the N-polar $Al_{0.6}Ga_{0.4}N$ surface, which is created by the removal of the sacrificial layer, of different VCSEL structures after bonding but before the top DBR deposition. The epitaxial structures have dif-

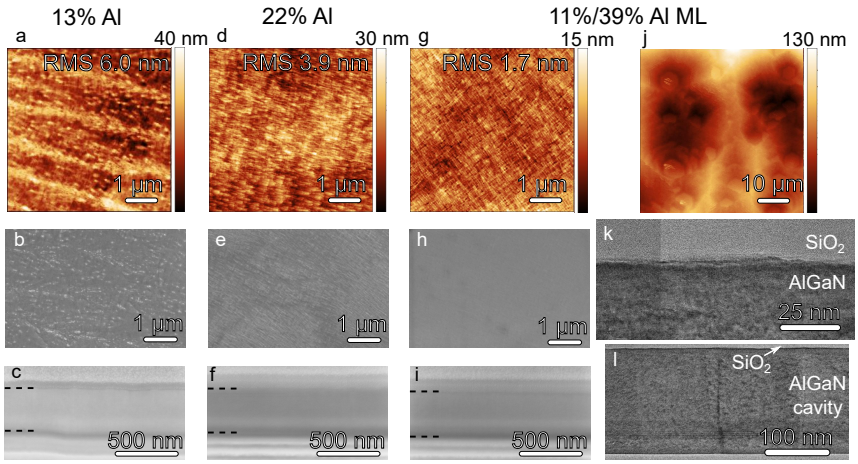

Figure 5.5: AFM and top-view SEM images of the N-polar $Al_{0.6}Ga_{0.4}N$ surface, which is exposed after electrochemical etching, and cross-sectional SEM images of the VCSEL structures, taken after bonding but before top DBR deposition. (a-c) Using a 13% Al-content sacrificial layer, (d-f) using a 22% Al-content sacrificial layer, and (g-j) using an 11/39% Al-content multilayer at the top of a 39% sacrificial layer. The dashed lines mark the interfaces between the bottom DBR, the AlGaN cavity, and the platinum layers deposited on the top as protection during focused-ion-beam milling. (k) TEM image of the interface between the top DBR and etched N-polar surface and (l) of the entire AlGaN cavity between the two DBRs (only the first SiO_2 layers are visible).

ferent sacrificial layers but are otherwise identical and were etched using the same voltage and acid concentration. The Si concentration were 2×10^{19} cm^{-3} in all sacrificial layers. In an initial fabrication run, the sacrificial layer was a 130-nm thick $Al_{0.13}Ga_{0.87}N$ layer and the RMS roughness of the etched surface was approximately 6 nm over $5 \times 5\,\mu m^2$. A smoother surface with an RMS of 4 nm was achieved for an $Al_{0.22}Ga_{0.78}N$ sacrificial layer. The $Al_{0.22}Ga_{0.78}N$ sample did not show the relatively large striations marks along the etching direction that are visible for the $Al_{0.13}Ga_{0.87}N$ sample in Fig. 5.5a. Furthermore, the higher Al content improved the morphology of the as-grown structure, which for the $Al_{0.13}Ga_{0.87}N$ sacrificial layer sample showed roughening due to partial relaxation. This improvement is visible when comparing the bottom DBR-cavity interfaces in Fig. 5.5c and Fig. 5.5f. Even smoother interfaces were achieved for the VCSELs in Paper A for which an $Al_{0.11}Ga_{0.89}N/Al_{0.39}Ga_{0.61}N$ multilayer allowed for a preferential etching at the interface between the cavity layers and sacrificial layers, while maintaining the structural quality of the device layers grown on top. On a small scale, there is still visible roughness as seen in the AFM image in Fig. 5.5g and the transmission electron microscopy (TEM) image in Fig 5.5k. However, the correlation length of these structures, extracted from the AFM measurements, is below 50 nm, which is considerably smaller than the lasing wavelength and should therefore only give a modest contribution to the scattering losses [160]. On a larger scale, as seen in Fig. 5.5j, the morphology shows hillocks similar but inverted to those of the as-grown structures, which were grown on AlGaN pseudosubstrates.

5.2 Proof of lasing

To confirm lasing in standard lasers with well-known behaviour it is often sufficient to observe a threshold in output power versus pump power and a clear spectral narrowing. However, for lasing in novel devices, more detailed analysis is warranted to unambiguously verify lasing as thresholds in emission intensity and moderate linewidth narrowing, for example, can be a result of stimulated emission without sufficient optical feedback to provide a net round-trip gain [206–208]. To support reporting and evaluation of lasing claims, *Nature Photonics* provides a useful checklist of points to evaluate when claiming lasing [209]. All points might not be relevant for every demonstration, but they serve as practical guidelines. The listed points include the observation of a threshold in output power and spectral narrowing as well as measurements of the coherence/polarization and the beam profile. Additionally, a lasing claim should include a description of operating conditions as well as a theoretical analysis to confirm that the results are plausible and rule out alternate explanations. It is also helpful to include data about the number of devices fabricated and characterized as well as information about their lifetimes.

A valuable characterization tool to address multiple of these points is angle-resolved photoluminescence (PL). Like ordinary PL, both the intensity and linewidth can be tracked, but it also gives information about the beam divergence. In Fig. 5.6, the angle-

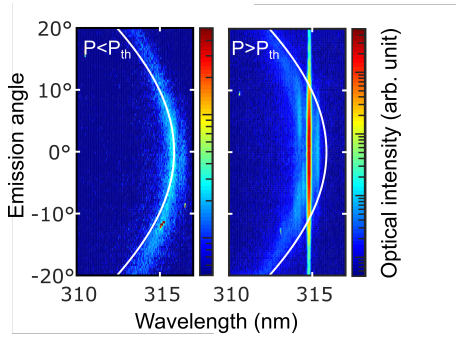

Figure 5.6: Measured angle-resolved PL spectra with optical intensity in logarithmic scale of a UVB VCSEL below and above the threshold pump power P_{th}. The white curves show the position of the longitudinal mode simulated using TMM.

resolved spectrum of a UVB VCSEL is shown both below and above threshold, including TMM simulations of the angular dispersion of the cavity mode. The cavity mode shape is explained by the fact that the out-of-plane wavevector needs to have a certain value to maintain resonance while the in-plane wavevector will increase with the emission angle, thus giving rise to an increased magnitude of the total wavevector and a decrease in wavelength with angle. Below threshold, the emission is dominated by the angular-dispersive cavity mode. If the cavity resonance has a large blue shift relative to the PL peak of the as-grown epitaxy, coupling between the cavity mode and QW emission is poor, and at low pump powers, the spectrum would instead be dominated by non-dispersive emission similar to that of a sample without a cavity. Above threshold, a lasing peak with narrow linewidth and narrow beam width is visible. The lasing emission is directly distinguishable from any spontaneous emission unfiltered by the cavity or coupled into cavity modes. Angle-resolved PL, therefore, greatly aides the evaluation of VCSEL lasing and can be used to rule out other explanations such as amplified spontaneous emission and non-vertical cavities, which were debated in the early days of optically pumped III-nitride vertical cavity devices [91, 194, 210–213]. Furthermore, it can provide a more convincing proof of lasing for demonstrations with only moderate linewidth narrowing and with peak intensities in the same order of magnitude as the background spontaneous emission [191, 198].

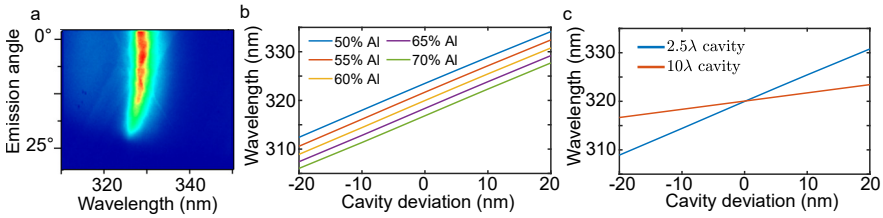

Figure 5.7: (a) Measured angle-resolved spectrum for a UVB VCSEL with a longer cavity length than targeted. (b) Simulated resonance wavelength of a VCSEL cavity as a function of thickness deviation of the cavity layers for different Al content in the top and bottom AlGaN cavity layers. (c) Simulated resonance wavelength of an $Al_{0.6}Ga_{0.4}N$ VCSEL as a function of thickness deviation of the cavity layer for two different cavity lengths.

5.3 Cavity length, resonance wavelength, and filamentation

A precise control of the cavity length is crucial to tailor the detuning between gain peak and resonance wavelength and to obtain the right spatial overlap between the standing optical field and the gain and loss regions. The importance of this precise control is seen in Fig. 5.7. Figure 5.7a shows the angle-resolved PL spectrum of a VCSEL which had a longer cavity length, and as a result, a longer resonance wavelength than the intended 320 nm. These devices did not lase as the PL peak of the as-grown sample was around 320 nm and the gain at 330 nm, therefore, is insufficient to support lasing even at high pump powers. As shown from the TMM simulations presented in Fig. 5.7b, the deviation in resonance wavelength of the 2.5λ cavity could be due to thicker cavity layers and/or lower Al-contents than intended. Inaccuracies in assumed refractive indexes or thickness deviations of especially the first DBR layers could also influence the resonance. However, the Al contents extracted from X-ray diffraction measurements differ from the design by a at most a few percent, the measured DBR stopband matches well with the simulated, VCSELs fabricated in different batches but using the same epitaxial structure have a reproducible detuning, and the detuning is different for VCSELs fabricated using structures from different growth runs, indicating that it is not due to inaccurate refractive index. The physical thickness deviation is, therefore, likely the major contribution to the deviation in resonance wavelength as the other sources are estimated to only contribute with a few nm or less in resonance shift. Note that the resonance shift of the cavity of between 0.5 and 0.6 nm per nanometer thickness deviation agrees well with the result received by taking the derivative of Eq. (3.5) and assuming a DBR penetration depth of $\lambda/4\Delta n$ [85]. It is possible to set the resonance to other values than that given by the epitaxial thicknesses by changing the thickness of the first DBR layers or adding a dielectric layer between the AlGaN and the DBR, as described in Paper B.

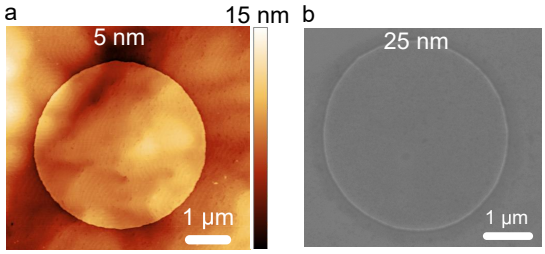

Figure 5.8: (a) AFM image of a 5 nm deep relief etched into $Al_{0.6}Ga_{0.4}N$. (b) SEM image of a 25 nm deep relief etched into $Al_{0.6}Ga_{0.4}N$.

In addition to macroscopic deviations in cavity length, also local lateral variations will influence the lasing characteristics. These variations, together with the lack of intentional optical guiding structures and other sample inhomogeneities that give lateral fluctuations in modal gain, can give rise to filamentary lasing. A route to instead promote lasing of well-defined lateral modes is to add relief structures inside the cavity to introduce intentional optical guiding. These can be etched into the AlGaN cavity as shown in Fig. 5.8 by slow (0.4 nm/s) Cl_2/Ar reactive ion etching. However, for the relatively short 2.5λ cavities, the unintentional lateral cavity variations are themselves similar to what would be needed to achieve the $\Delta n/n \approx 1\%$ index guiding which is typically used [88, 89]. Thicker cavities are less sensitive to cavity length variations, as shown in Fig. 5.7c, and filamentation could then potentially be easier to suppress as long as the lateral thickness variations do not scale with cavity length.

Another benefit with a long cavity length is that it can improve the thermal performance, which has been shown for GaN-based VCSELs by multiple groups [181, 214, 215]. The poor thermal conductivity of especially dielectric DBRs means that the majority of the generated heat will need to flow laterally. The high thermal resistance of the DBRs will be an even bigger problem for UV VCSELs where a large part of the cavity will consist of low thermal conductivity AlGaN, and not GaN, as is the case for near UVA and visible-emitting VCSELs. However, this problem could be reduced by using a small bottom DBR radius and an intracavity heat spreading layer [216, 217].

One interesting feature with our 2.5λ-cavity VCSELs is that the lasing wavelengths are surprisingly stable with temperature and show an average lasing wavelength shift of approximately -0.001 nm/K from room temperature to 66°C. This value has a different sign and is about one order of magnitude smaller than what is typically measured for blue-emitting VCSELs [109]. The reason for this is attributed to a relatively large and negative thermo-optic coefficient of HfO_2, which was measured by ellipsometry. As these short-cavity VCSELs have a significant part of the optical field intensity in the dielectric mirrors, the decreased refractive index with temperature in the HfO_2 layers compensates for the increase in refractive index in the AlGaN and SiO_2 layers, resulting in only a

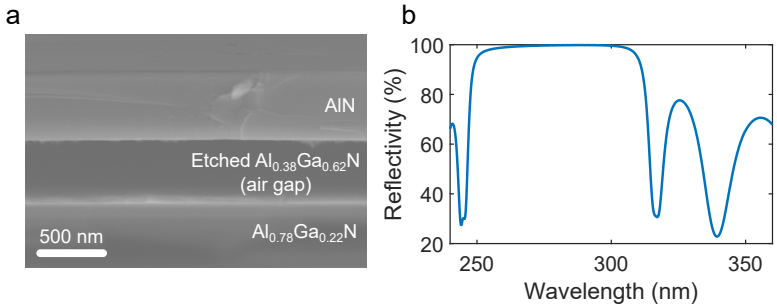

Figure 5.9: (a) Cross-sectional SEM image of an underetched AlN membrane. (b) Measured reflectivity spectrum of a 10 pair HfO_2/SiO_2 UVC DBR deposited on a Si wafer.

minor net change in resonance wavelength.

5.4 Towards optically pumped UVC VCSELs

The methods used to fabricate optically pumped UVB VCSELs can also be extended to UVC VCSELs. We have previously demonstrated complete electrochemical etching of AlGaN with up to 50% Al content, but these structures were grown on AlGaN pseudosubstrates with $Al_{0.5}Ga_{0.5}N$ top membranes [112]. Our experience is that it can be difficult to reach complete etching, even at significantly higher voltages, for structures grown on AlN templates and with higher Al-content membranes. The reason for this is still unknown, but could be due to the influence of strain on the electrical and mechanical properties, doping incorporation, or process related complications. Nevertheless, electrochemical release of an AlN membrane was achieved by using a thin $Al_{0.38}Ga_{0.62}N$ sacrificial layer etched at 60 V. The release of the AlN membrane was done using a lower acid concentration compared to that used for the UVB structures, as the resulting slower dissolution of the metaloxides can promote electropolishing over porosification [218]. However, too low acid concentrations leads to a build-up of Ga-oxides and prevents etching. The underetched AlN membrane, shown in cross-section in Fig. 5.9a, had an RMS surface roughness of the etched N-polar surface that was similar to the as-grown metal-polar surface of the epitaxial structure.

To extend the VCSEL emission to UVC wavelengths also requires dielectric DBRs with above 99% reflectivity. SiO_2 has a negligible absorption even in the UVC, but HfO_2 can have significant sub-bandgap absorption when the deposition process is not optimized. By increasing the oxygen to argon ratio during sputtering, we reduced the HfO_2 absorption and achieved a DBR with over 99% reflectivity in the entire 260-300 nm range, as shown in Fig. 5.9b [219].

Chapter 6

Electrically conductive GaN-based distributed Bragg reflectors

Most III-nitride VCSELs use intracavity contacts, as shown in Fig. 6.1a. If, however, the n-side mirror is made to be electrically conductive, it would be possible to place the n-contact outside the cavity, either as in Fig. 6.1b or by using a backside contact as in Fig. 6.1c. Such solutions could lead to improved current spreading and lower device resistance as well as allow for shorter cavities lengths [185, 186]. Although shorter cavities can increase the thermal resistance, it may also reduce the internal absorption losses and in this way reduce the device threshold. Furthermore, a short cavity can be beneficial for high speed applications as this would lead to a higher optical confinement factor and a shorter photon lifetime, and an in turn potentially higher modulation bandwidth, without the threshold current penalty that results from shortening the photon lifetime by reducing the DBR reflectivity [220–222].

Unfortunately, the III-nitrides suffer from large band offsets and polarization fields, and donors with high ionization energies in high Al-content layers. This complicates the growth of DBRs that have both high reflectively and low electrical resistance perpendicular to the layers. Furthermore, there is a trade-off between electrical conductivity and optical losses as graded interfaces reduce reflectivity and high doping increases optical absorption. Nevertheless, several types of electrically conductive DBRs have been reported and two types have also been incorporated in VCSELs.

The first type is AlInN/GaN, where Meijo University has managed to achieve specific series resistances (series resistance multiplied with the mesa area) down to $1.7 \times 10^{-4}\,\Omega\,\mathrm{cm}^2$ for 10 pairs using compositional gradients and modulation doping at the DBR

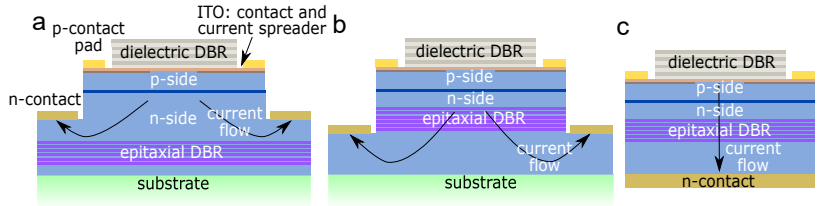

Figure 6.1: (a) Schematic of a hybrid VCSEL having electrically insulating DBRs and intracavity contacts. (b,c) Hybrid VCSEL with electrically conductive epitaxial n-side DBR and n-contact outside the cavity on the (b) frontside or (c) backside of the wafer.

interfaces [186, 223, 224]. To reach the high reflectivity that is required for VCSELs, about 40 pairs are needed, but even for such a DBR, the specific series resistance will be below $10^{-3}\,\Omega\,\mathrm{cm}^2$. Meijo University used conductive 40-pair AlInN/GaN DBRs in 4λ-cavity VCSELs reaching output powers up to 2.6 mW [185, 186]. However, the output power was still lower than for similar structures with non-conducting DBRs. This was attributed to higher surface roughness and lower efficiency of the QWs as a result of the high doping levels in the DBR and shows that additional optimization of the growth is needed [185]. Furthermore, a 1.5λ-cavity device showed lower maximal output power, mainly due to a high thermal resistance resulting from the thin cavity and low thermal conductivity of the ternary AlInN layers in the DBR [186]. This problem could be reduced by using only binary materials in the DBR [214], such as AlN/GaN or ZnO/GaN.

The second type of electrically conductive mirror that have been successfully incorporated in III-nitride VCSELs is the nanoporous DBR. Yale University demonstrated a VCSEL operated in pulsed mode with an increase in turn-on voltage of 0.4 V and in differential resistance of only $4\,\Omega$ when using a contact outside the cavity instead of the intracavity contact [119]. Important to note is that the lateral porosification of the DBR only extended across parts of the device mesa and it is, therefore, not possible to rule out that at least a part of the injected current circumvents the DBR by laterally spreading in the intact n-GaN layers below the DBR and in the 6λ cavity. Nevertheless, similar voltage penalties have been seen for vertical injection through a comparable DBR used in LEDs, where the porosification extended across the entire device mesa, but the large difference between current aperture and mesa area prevents a direct calculation of the specific series resistance of the DBR [225]. Porous structures can have both high thermal and electrical conductivity but as both decrease with increasing porosity, there is trade-off between thermal and electrical performance and high optical performance, i.e. high refractive index contrast [226].

There have also been a few demonstrations of electrically conductive Al(Ga)N/GaN DBRs [95, 227–229]. The lowest specific series resistance, $2\times10^{-4}\,\Omega\,\mathrm{cm}^2$, was achieved using an Al content of only 12%, resulting in a reflectivity of only 92% due to the small

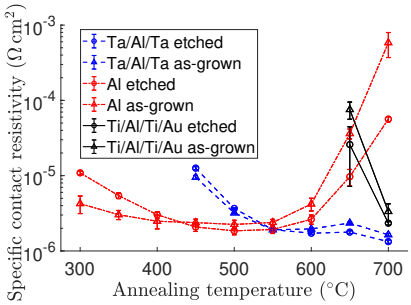

Figure 6.2: Measured specific contact resistivity as a function of annealing temperature in a nitrogen atmosphere for Ta/Al/Ta, Al, and Ti/Al/Ti/Au contacts deposited on dry etched and as-grown n-GaN with an electron concentration of $n = 1\text{-}3 \times 10^{18}$ cm^{-3}.

refractive index contrast [229]. The only demonstration of a reflectivity above 99% was using AlN/GaN, with a specific series resistance of around 0.1 $\Omega\,\text{cm}^2$ extracted from the current-voltage characteristics [95]. As mentioned in Chapter 4, the complex growth of the large lattice mismatch AlN/GaN may require insertion of strain-compensating layers, and this motivates the investigation in Paper C on how the vertical resistance is affected by compositional interlayers.

A new type of an electrically conductive DBR is ZnO/GaN, which in addition to a similar large refractive index contrast and smaller lattice mismatch than AlN/GaN, has several properties that makes it ideal for vertical injection. ZnO and GaN are easily n-doped, have a small conduction band offset, and, as discussed in Paper D, strained structures have much smaller polarization charges at the interfaces than pure III-nitride DBRs.

All ZnO/GaN and AlN/GaN samples investigated were grown using PAMBE at Chalmers. The ZnO/GaN was grown by David Adolph using a hybrid MBE and the AlN/GaN DBRs by Martin Stattin using a nitride-dedicated system.

6.1 Characterization of electrically conductive DBRs

To electrically characterize DBRs accurately, it is important to use low-resistance ohmic contacts. However, as the structures have significant built-in strain and differences in thermal expansion, the rapid thermal annealing at temperatures above 800°C and fast ramps typically used for III-nitride n-contacts, could potentially degrade the DBR quality. To avoid annealing at unnecessarily high temperatures, the contact resistance of three different metal stacks annealed at low temperature was investigated. Based on previous reports in literature [230, 231], Al (150 nm) and Ta/Al/Ta (7/280/20 nm) together with the standard high-temperature annealed Ti/Al/Ti/Au (5/10/20/200 nm) contact were chosen, and

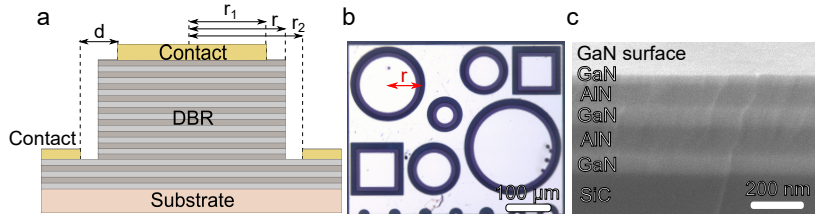

Figure 6.3: Structure used to measure the resistance through AlN/GaN and ZnO/GaN stacks. (a) Schematic cross-section. (b) Top-view optical microscope image of mesas with different sizes (only circular mesas were used). (c) Cross-sectional SEM image of an etched AlN/GaN DBR showing the exposed GaN surface on which the bottom contact was placed.

the results are shown in Fig. 6.2. Contacts to both dry etched and as-grown surfaces were investigated as the DBRs to be characterized were grown on low electrically conductivity substrates and the bottom contact, therefore, needs to be placed on an etched GaN layer (see Fig. 6.3). In the contact tests, the contacts were all deposited on commercially available GaN-on-sapphire templates with electron concentration of $n = 1\text{-}3 \times 10^{18}\,\mathrm{cm}^{-3}$, and each sample was annealed in a nitrogen ambient step-wise from 300°C, using a 30-s annealing duration for Ti/Al/Ti/Au and a 60-s annealing duration for Al and Ta/Al/Ta. As the Al contact showed the lowest contact resistance at low temperatures, these were chosen for the DBR characterization. When deposited on the DBRs, the Al contact was ohmic already as-deposited with a resistance around $10^{-4}\,\Omega\,\mathrm{cm}^2$. As this was low enough to only give a minor contribution to the total resistance, no annealing was performed.

The device structures used to characterize the DBRs' resistances are shown in Fig. 6.3. It is obvious, that if the vertical resistance through the DBR is dominating, as is the case for the AlN/GaN DBRs, the measured specific series resistance, R_sA, should be independent of the mesa area. However, the expected trend is less obvious if instead the contact and lateral resistance are dominating, which is the case for the ZnO/GaN DBRs. The lateral and contact contributions can be estimated using the same equations used for circular transfer length method (TLM) measurements. Assuming constant sheet resistance, these contributions are given by [232]

$$R_{lc} = \frac{R_{sh}}{2\pi}\left(\frac{L_t}{r_1}\frac{I_0(r_1/L_t)}{I_1(r_1/L_t)} + \frac{L_t}{r_2}\frac{K_0(r_2/L_t)}{K_1(r_2/L_t)} + \ln\left(\frac{r_2}{r_1}\right)\right). \tag{6.1}$$

I and K denotes modified Bessel functions of the first and second kind and L_t the transfer length, which is typically in the order of a few micrometer and a characteristic of how far from the contact edge the current flows. If $r = r_1 \approx r_2 \gg d$ and L_t (see Fig. 6.3), the Bessel functions approach unity and by using the Taylor expansion of the natural logarithm [232], Eq. (6.1) simplifies to

$$R_{lc} = \frac{R_{sh}}{2\pi r}\left(d + 2L_t\right). \tag{6.2}$$

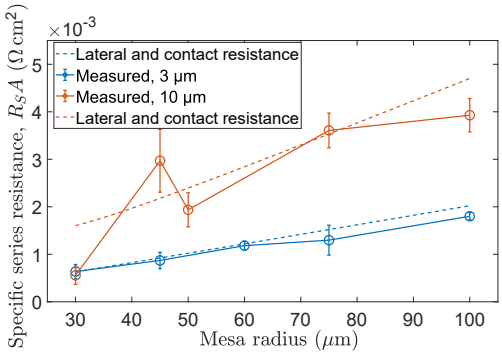

Figure 6.4: Measured and calculated specific series resistance of three ZnO/GaN pairs for a distance between contact edge and mesa ($r_2 - r$ and $r - r_1$ in Fig. 6.3) of 3 µm and 10 µm.

Thus, $R_{lc}A$ varies linearly with r since $A = \pi r^2$ and the measured specific series resistance should increase approximately linearly with increasing mesa radius if these contributions are dominating. The relatively large contribution from especially the lateral resistance in the ZnO/GaN samples is evident from the comparison in Fig. 6.4 between measurements on a sample, which had a spacing between contact and mesa edge of 10 µm ($d = 20$ µm), and a sample with mesa to contact edge spacing of 3 µm. The latter sample design is what is presented in Paper D. It is clear that the resistance of the ZnO/GaN multilayer is so small that the electrical measurements only provide an upper limit of the actual vertical resistance. Note that the calculations of the lateral and contact resistances in Fig. 6.4 are done using the exact Eq. (6.1) with R_{sh} and L_t extracted from TLM measurements.

6.2 Electrical simulations

To get a better estimate of the vertical resistance in ZnO/GaN DBRs, drift-diffusion simulations were performed as presented in Paper D. Spontaneous and piezoelectric polarization fields have a large influence on the electrical resistance and their implementation deserves extra attention. Typically, these effects are included in simulations by adding interface charges using Eq. (2.1) with material constants from e.g. Ref. [233]. However, in 2016, Dreyer et al. showed that two separate misinterpretations of the material constants have resulted in a general error in the implemented polarization charges. Due to inappropriate use of a zincblende reference structure in the calculations of the spontaneous polarization constants, a correction term should be added to the polarization charge [234],

$$\Delta P_{\text{corr,sp}} = \frac{e\sqrt{3}}{2}\left(\frac{1}{a_n^2} - \frac{1}{a_m^2}\right), \tag{6.3}$$

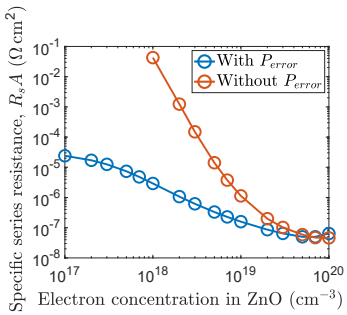

Figure 6.5: Simulated specific series resistance for three pairs of ZnO/GaN with and without the P_{error} term added to the interface charges.

where e is the electron charge and a_n and a_m are the in-plane lattice constants of the two materials. The second mistake, which is relevant for strained structures, is to use the so called "proper" instead of the "improper" piezoelectric constants for the strained material n. For e_{33} there is no difference, but for e_{31}, these constants are related according to

$$e_{31}^{n,\text{imp}} = e_{31}^{n,\text{prop}} - \left(P_{\text{sp}}^{n} + \frac{e\sqrt{3}}{2a_n^2} \right), \tag{6.4}$$

where $e_{31}^{n,\text{prop}}$ and P_{sp}^{n} are the values of the material constants most often found in literature. The addition of $\Delta P_{\text{corr,sp}}$ and the use of the improper rather than proper e_{31}, will add a term, P_{error} to Eq. (2.1). Luckily, in the most common situations of pseudomorphic growth of III-nitrides, these two contributions almost cancel each other out and there is only a relatively minor change in total polarization charge, especially considering that experimentally measured polarization charges often are considerably lower than what is theoretically estimated, which may be due to experimental uncertainties or, for example, compensation by interface traps. Nevertheless, for relaxed structures, P_{error} will make a significant difference [48].

In the case of ZnO/GaN interfaces, even for strained structures, the addition of P_{error} will result in noticeable changes in resistance, as shown in Fig 6.5. It is a result of the relatively small total polarization charge and band offset. It should be noted that no empirical scaling factor, sometimes used to account for the compensation of charges observed experimentally, was used in the simulations. Thus, it is reasonable to assume that, especially at low doping concentrations, the real resistance could be lower than simulated. At larger electron concentrations and low resistances, the resistance could instead be underestimated due to not accounting sufficiently for mobility-reducing material imperfections.

Chapter 7

Microcavities based on dislocation-free GaN prisms

Nanowire-based materials provides a platform for making devices with small footprints and the possibility of incorporating more strain than what is achievable using traditional growth [83, 84]. Perhaps most promising, is that it is possible to completely prevent threading dislocations to extend into the nanostructures [71–73]. Thus, these type of structures could allow for large and low-cost templates, such as GaN on sapphire or even GaN on Si, to be used instead of expensive free-standing GaN substrates typically employed for blue-emitting state-of-the-art VCSELs and commercial laser diodes.

Numerous types of nanowire-based III-nitride lasers have been reported, including horizontal Fabry-Pérot lasers [235–237], random lasers [238], photonic crystal surface- or edge-emitting lasers [239, 240], whispering-gallery mode lasers [241, 242], and vertical-cavity devices [191, 242–246]. In the case of vertical-cavity nanowire lasers, these have been optically pumped and mainly excited by pumping the entire GaN cavity. For a device to be suited for electrical injection, the cavity must have sufficiently small losses to support lasing using only a few QWs. This is unlikely to be met for vertical cavities without high-reflectivity mirrors, i.e. using single facet reflections [242, 245, 246] will make lasing under electrical injection extremely challenging.

An optically pumped nanopillar VCSEL with a QW active region has been reported, but in addition to having a weak lasing peak with a FWHM as large as approximately 2 nm above threshold, the nanopillar structures were fabricated using a top-down approach [191]. Top-down approaches, in which the nanostructures are created using subtractive processes such as dry etching, can lead to damaged and rough surfaces as well as inclined sidewalls. These problems can be solved by combining dry etching with anisotropic wet etching to create smooth vertical facets [236, 247]. Nevertheless, top-down fabrication can only achieve limited dislocation filtering. For making completely dislocation-free

structures, the bottom-up approach, where the nanostructures are created directly during growth must be used. Thus, to reap the full benefits of both VCSELs and nanowires, a structure that can support lasing in a vertical cavity while possible to create using the bottom-up approach is needed.

III-nitride nanowire structures usually have pyramidal-shaped tips [72, 73, 239–241, 244, 248] These prevent the perpendicular reflections that are needed to reduce losses and form the vertical cavity. However, Maryam Khalilian et al. at Lund University, have developed nanowire-based GaN hexagonal prisms grown using MOVPE (see Fig. 7.1a), which are both completely dislocation-free and have flat c-plane top facets [71]. The flat top make these structures a promising basis for dislocation-free VCSELs grown on low cost substrates. Figure 7.1b shows a proposed schematic of a future electrically injected prism VCSEL.

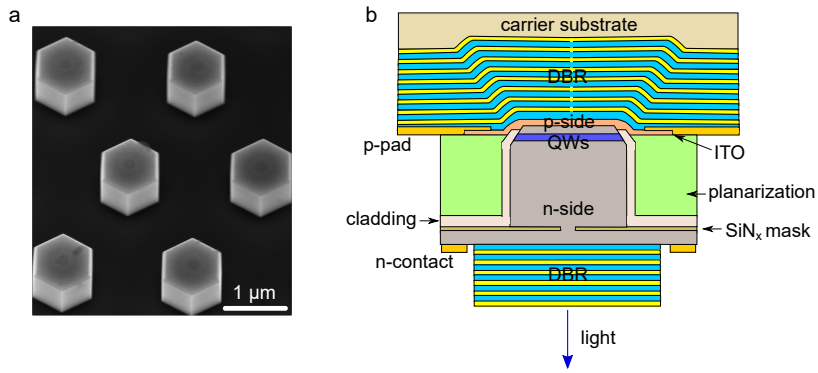

Figure 7.1: (a) SEM image of as-grown hexagonal GaN microprisms. (b) Schematic of a proposed electrically injected microprism VCSEL.

7.1 Microcavity fabrication and characterization

The different steps used to grow GaN microprisms are illustrated in Fig. 7.2a-h. First, a SiN_x mask is deposited and patterned to define the area where the selective area growth will take place. Thereafter, an annealing step, crucial for the threading dislocation filtering, is performed and results in an inverted pyramidal shape. The selective area growth starts with a nucleation step and vertical nanowire growth. By changing the growth parameters, the structure is grown radially before a high temperature reformation step is used to transform the pointed tip structure to a flat top prism [71]. The reformation relies on the minimization of the surface energy that can be described by the Wulff equilibrium shape model and surface diffusion kinetics [71, 249]. The structure is finalized by growing a thin layer of GaN on top to achieve an atomically flat surface [71].

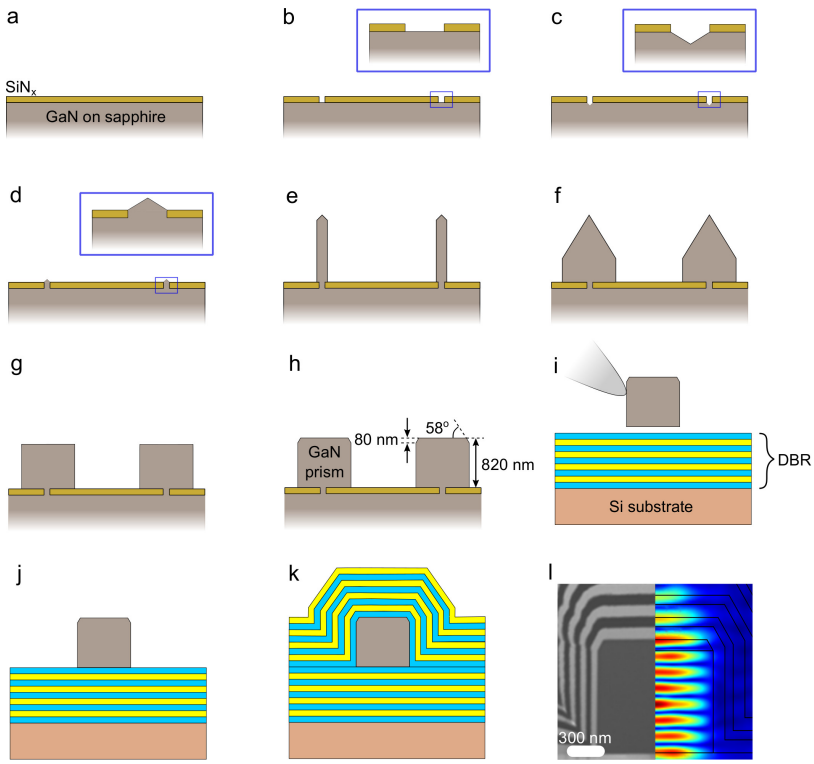

Figure 7.2: Growth and fabrication of microprism vertical cavities. (a) A silicon nitride mask on a GaN-on-sapphire template is (b) patterned with holes. (c) Inverted pyramidal structures are created by annealing before (d) nucleation and (e) nanowire growth. (f) The structure is grown radially before (g) reformation and (h) growth of a thin GaN layer on the c-facet. (i,j) Individual prisms are transferred to a DBR using a micromanipulator before (k) the cavity is finalized with a top DBR. (l) Cross-sectional scanning TEM image of a prism wrapped with a top DBR (left) and a simulated electrical field profile (right).

The unconventional structure of the prism prompts the question if the structural quality of the cavity is sufficient to support lasing. To answer this, prism microcavities were formed by embedding single prisms between two dielectric DBRs as shown in Fig. 7.2.

The Q factor of an optically cavity is often extracted by experimentally measuring the FWHM of a cavity resonance and applying Eq. (3.7). However, when the cavity contains active layers that are excited, the extracted Q will depend on the absorption or gain in these layers and will, thus, depend on pumping power [250]. For lasers, a rough estimation of the Q of the passive cavity (excluding any contribution from the QWs) can be measured slightly below threshold, where the active region is assumed to be pumped to transparency. Nevertheless, it is not uncommon that the Q factor is estimated using the FWHM above threshold [191, 245], but as these values will deviate significantly from the Q of the passive cavity, comparisons between values reported in literature should be made with care.

A way to exclude the influence of pumping power when measuring the intrinsic structural quality factor of the cavity is to investigate the FWHM of resonances at spectral positions where the losses and gain of the cavity material is negligible, e.g. at a sufficient spectral distance below the bandgap. In our case, we used the fact that the yellow luminescence (YL) often seen for GaN material is not associated with any absorption at these wavelengths. The YL is believed to originate from deep acceptor defects related to Ga vacancies or carbon, perhaps in the form of complexes formed with oxygen. Furthermore, the yellow luminescence emits over a wide spectral region [251]. Therefore, the cavities were fabricated to have a resonance at 550 nm. However, future devices with QWs would target emission at blue wavelengths.

7.2 Microcavity simulations

Simulations of microcavities were performed using the commercially available software COMSOL Multiphysics. The software allows for efficient meshing and numerical solutions using the finite element method. It was used to compute the solutions to the frequency domain wave equations that can be derived from Maxwell's equations assuming the solutions consist of time-harmonic electromagnetic fields [252]. COMSOL was controlled using LiveLink for MATLAB and the code, that initially was developed for simulations of threshold material gain of similar structures [253], was in this work expanded and modified to give the Q factor of the passive prism microcavities. To limit the computational complexity and allow for sweeps of structural parameters within reasonable time frames, the structures are approximated by circular symmetric cavities, which still gives similar lateral mode profiles and reflection at facets as hexagonal structures [253, 254]. Figure 7.3 shows electric field profiles of different sized prism cavities. All field profiles are the physical solutions to quasi-3D finite element frequency-domain method (Q3D-FEM) with the highest Q. The Q factor is calculated using the solutions' eigenvalues according to Eq. (3.7). Note that in the supplementary of Paper E, the notation

follows COMSOL's convention where the eigenvalue λ corresponds to $-j\omega$ in Eq. (3.7).

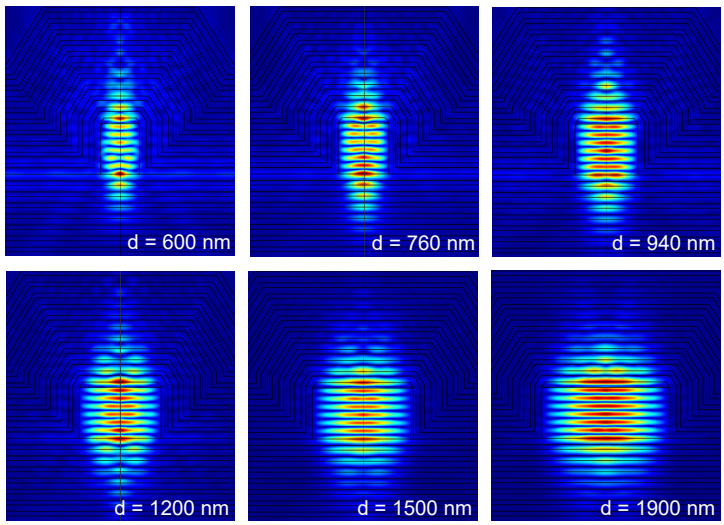

Figure 7.3: Simulated electrical field profiles in linear scale for circularly-symmetric microcavities with different prism diameters.

Chapter 8

Summary and future directions

Driven by applications within a wide range of areas, significant effort has been put into the development of III-nitride VCSELs. Due to challenges related primarily to mirror formation and electrical injection, numerous different device architectures have been pursued, each with different advantages and disadvantages. For blue-emitting VCSELs, the performance has improved significantly in the last few years and it is anticipated that the first commercial devices will be available within only a few years from now. As the field continues to mature, it is possible that the research and development converge towards a single superior device architecture. More likely, however, is that the parallel development will continue. As VCSELs are moving closer to being commercially available, the performance characteristics needed for different applications will become clearer. Depending on these characteristics, different solutions could be favored. For example, for high power applications, thermal performance will be crucial and devices with very long cavity lengths will be preferred, while for sensitive sensing applications requiring single-mode emission and precise wavelength control, shorter cavity lengths are likely needed. The trade-off between diverse performance requirements also needs to be balanced against production cost, which strongly depends on device complexity and yield for that device concept. Thus, it is not unlikely that multiple types of III-nitride VCSELs will reach the market in the future.

In contrast to blue-emitting devices, UV VCSELs still have a long way to go. Nevertheless, our demonstration of the first optically pumped UVB VCSEL, provides a key step towards VCSELs that together can cover a large part of the UV spectral range, as the use of electrochemical etching to create cavities with high Al-content AlGaN layers in between two dielectric DBRs also should be extendable to UVC devices. The development of UV VCSELs will also be spurred by the rapid technological improvements in growth and processing of UV LEDs and edge-emitting laser diodes. Furthermore, the ongoing pandemic has raised awareness of the importance of sterilization of air and surfaces and

will give a boost to the development of AlGaN emitters.

To become useful in real-world settings, VCSELs need to be electrically injected and as tunnel junctions seem to the by far most promising option for UV VCSELs, the continued improvement of high Al-content tunnel junctions is imperative. It is likely that these junctions will use a low bandgap interlayer and an optimization of doping, alloy composition, and thicknesses will be needed to find a balance between optical absorption and electrical performance. As the devices become electrically injected, optimization of thermal performance is necessary and intracavity heat spreaders are likely needed to divert heat away from the low thermal conductivity AlGaN layers.

Due to the importance of low threading dislocation densities, it is reasonable to expect that expensive free-standing AlN substrates in the future will be used for UV VCSELs, at least in the UVC. In that case, electrochemical etching would be beneficial compared to other mirror and substrate-removal technologies that are not compatible with substrate reuse.

In addition to VCSELs, the methods to underetch and bond AlGaN membranes with DBR mirrors or single dielectric layers could potentially be used for UV and blue vertical-external-cavity surface-emitting lasers (VECSELs) or opto-mechanical cantilevers. Furthermore, free-hanging III-nitride half-VCSELs released by electrochemical etching could be transfer-printed onto waveguides with diffractive gratings to be used as light sources in wide-bandgap photonic integrated circuits.[255, 256]

Although the performance of III-nitride VCSELs without electrically conductive DBRs are still superior, continued improvements in growth could make electrically conductive DBRs competitive for blue-emitting VCSELs. AlInN/GaN and low Al-content AlGaN/GaN DBRs will continue to have lower vertical resistance than AlN/GaN but the introduction of modulation doping and compositional gradients could potentially lower the resistance enough for the optical benefits of AlN/GaN DBRs to outweigh the resistance penalty. Another option would be to still place the VCSEL n-contact in the cavity or on one of the intermediate GaN layers in an electrically conductive AlN/GaN DBR. This could help with current spreading in short-cavity VCSELs but without the current having to pass vertically through 20 mirror pairs or more.

In theory, ZnO/GaN is a highly competitive alternative as an electrically conductive n-type DBR in VCSELs. The measured resistance is indeed comparable or better than the best pure III-nitride DBRs but the reflectivity is still not sufficient for VCSELs. The low reflectivity is likely not due to fundamental issues but due to limited work on the hybrid growth of ZnO and GaN. Hopefully, the beneficial properties of ZnO/GaN heterostructures could prompt investments in hybrid MBE systems to tap into the full potential of ZnO/GaN DBRs. Furthermore, as ZnO can easily be wet etched, it could potentially be used as a sacrificial layer for substrate removal, air-gap DBRs, or current confinement.

ZnO/GaN is not the only type of semiconductor material pair outside the AlInGaN system that can be used for DBRs in the UV-visible range. BAlN/AlN and hBN/BAlN DBRs, which can be used in the UVB and UVC, have also been demonstrated and lattice-

matched AlPN/GaN DBRs have been proposed [257–259]. Moreover, SiC/AlGaN structures have been suggested for use as electrically conductive DBRs and doping-induced refractive index differences can be used to create GaN/GaN DBRs [260, 261]. Nevertheless, all these would need to see significant improvements in performance to be suitable for incorporation into VCSELs.

For lasers based on GaN microprisms, the natural next step after the investigations of the Q factor of microprism vertical cavities would be to grow QWs on the c-facet similar to that done for LEDs in Ref. [262]. Optically-pumped lasers could then be fabricated by using the same process steps as for the empty cavities in this work but with adjusted DBR layer thicknesses. Extension to electrically injected devices (see Fig. 7.1) demands a more complex processes flow. Although significant process development will be needed, the process can in principle use straightforward fabrication steps such as contact formation, planarization, bonding, and substrate removal using e.g. electrochemical etching or laser lift-off. Due to the devices' small lateral scale and the sensitivity of device performance on the cavity geometry, the process development should continuously be coordinated with simulations to decide on e.g. how far down the top DBR should wrap around the prism and what cladding layer material and thickness is optimal. Optimization of the prism growth, including height control and increasing the lateral size, will also be crucial for the device performance. There is still much more development needed, but GaN prisms could in the future enable dislocation-free small footprint VCSELs grown on large, low-cost substrates. The well-defined facets also open up for investigations of the coupling between adjacent prisms and its influence on the device characteristics.

Chapter 9

Summary of papers

Paper A

A 310 nm optically pumped AlGaN vertical-cavity surface-emitting laser

Filip Hjort, Johannes Enslin, Munise Cobet, Michael A. Bergmann, Johan Gustavsson, Tim Kolbe, Arne Knauer, Felix Nippert, Ines Häusler, Markus R. Wagner, Tim Wernicke, Michael Kneissl, and Åsa Haglund

ACS Photonics, vol. 8, issue 1, pp. 135-141, 2021.

Demonstration of an optically pumped UVB-emitting VCSELs. It is the first VCSEL with a high Al content and it has a shorter emission wavelength than any previously reported VCSEL. A cavity with over 99% reflectivity dielectric HfO_2/SiO_2 mirrors on each side of the cavity was realized by employing doping-selective electrochemical etching to remove the AlGaN substrate. By using a multilayer sacrificial layer, an etched surface as smooth as the as-grown layers was achieved, and this allowed for the formation of a high-quality cavity that supported lasing. Lasing was confirmed by a clear threshold in output power as well as a transition to polarized emission and narrowing of linewidths and beam widths at threshold, all observed using angular-resolved photoluminescence measurements.

My contribution: I developed the VCSEL fabrication process, including the creation and transfer by thermo-compression bonding of smooth AlGaN-membrane half-VCSEL structures that allowed for the double-dielectric DBR device geometry. I performed the device processing, with partial assistance from Johannes Enslin and Michael Bergmann, and did the SEM, AFM, reflectivity and parts of the photoluminescence measurement and most of the data processing and analysis. I also wrote the manuscript with input from the other co-authors.

Paper B

Low-threshold UVB VCSELs enabled by post-growth cavity length adjustment and smooth surfaces

Giulia Cardinali, **Filip Hjort**, Nando Prokop, Johannes Enslin, Munise Cobet, Michael A. Bergmann, Johan Gustavsson, Joachim Ciers, Ines Häusler, Tim Kolbe, Tim Wernicke, Åsa Haglund, and Michael Kneissl

Manuscript

Investigation of the influence of surface roughness and detuning between cavity resonance wavelength and PL peak of the as-grown sample on the UVB VCSEL lasing characteristics. VCSELs fabricated using a multilayered sacrificial layer showed a reduced surface roughness after electrochemical etching, and therefore lower threshold power density compared to VCSELs fabricated using a bulk sacrificial layer. Furthermore, by adding HfO_2 cavity length adjustment layers inside the cavity to reduce the detuning, the threshold power density can be decreased with an order of magnitude to below 1 MW/cm^2, compared to the sample without a cavity length adjustment layers.

My contribution: I decided which cavity length adjustment layers to use, fabricated the VCSELs and performed initial optical measurements. I contributed to the data analysis and paper layout, wrote parts of the paper, and gave feedback on the rest of the paper.

Paper C

Effect of compositional interlayers on the vertical electrical conductivity of Si-doped AlN/GaN distributed Bragg reflectors grown on SiC

Ehsan Hashemi, **Filip Hjort**, Martin Stattin, Tommy Ive, Olof Bäcke, Antiope Lotsari, Mats Halvarsson, David Adolph, Vincent Desmaris, Denis Meledin, and Åsa Haglund

Applied Physics Express, vol. 10, p. 055501, 2017.

Investigation of the impact of compositional interlayers on the vertical electrical resistance of AlN/GaN DBRs. A sample without interlayers had a specific series resistance of 0.044 $\Omega\,$cm^2 through 8 pairs, which is comparable to previously reported electrically conductive AlN/GaN DBRs. Compositional interlayers, consisting of 1.5 nm graded AlGaN or 0.5 nm/0.5 nm or 2 nm/2 nm AlN/GaN, had 4 to 10 times higher resistance. The results show that insertion of interlayers to, for example, compensate for strain, may reduce the vertical conductivity.

My contribution: I, together with Ehsan Hashemi, developed low-temperature annealed

n-contacts to n-GaN and processed the AlN/GaN samples. I measured the I-V characteristics of the samples with different compositional interlayers as well as processed and analyzed the data. I contributed to the discussion on what to include and gave feedback on the paper.

Paper D

Vertical electrical conductivity of ZnO/GaN multilayers for application in distributed Bragg reflectors

Filip Hjort, Ehsan Hashemi, David Adolph, Tommy Ive, Olof Bäcke, Mats Halvarsson, and Åsa Haglund

IEEE Journal of Quantum Electronics, vol. 54, no. 4, p. 2400406, 2018.

The first investigation of the electrical properties of recently developed ZnO/GaN multilayers that could find use as DBRs in GaN-based VCSELs. The measured resistance is dominated by lateral and contact resistance and the vertical electrical conductivity of three pairs of in-plane strained ZnO/GaN is determined to be around $10^{-4}\ \Omega\,\mathrm{cm}^2$ or lower. This is similar to, or lower, than the lowest values for pure III-nitride DBRs and, according to electrical simulations, the actual vertical resistance can be orders of magnitudes lower. The low resistance of the strained multilayer stack is identified to be a result of the partial cancellation of the piezoelectric and spontaneous polarization components at the ZnO/GaN interfaces.

My contribution: I, together with Ehsan Hashemi, developed the low-temperature annealed n-contacts to n-GaN and processed the ZnO/GaN samples. I measured the I-V characteristics, analyzed the data, identified the beneficial cancellation of polarization components in strained ZnO/GaN DBRs, developed the electrical simulations of multilayered ZnO/GaN in TCAD, and performed the electrical simulations. I also wrote the manuscript with input from the other co-authors.

Paper E

Optical microprism cavities based on dislocation-free GaN

Filip Hjort, Maryam Khalilian, Jörgen Bengtsson, Marcus Bengths, Johan Gustavsson, Anders Gustafsson, Lars Samuelson, and Åsa Haglund

Applied Physics Letters, vol. 117, no. 23, p. 231107, 2020.

Completely dislocation-free hexagonal GaN microprisms are used to form optical ver-

tical cavities by embedding the prisms between two dielectric DBRs. The Q factor of the cavities is investigated using cathodoluminescence measurements and both quasi-3D finite element frequency-domain method (Q3D-FEM) and 3D beam propagation method simulations. The filtered yellow luminescence show resonances with linewidths that decrease with increasing prism width. 1000 nm wide prisms have Q factors of around 500, with good agreement between measurements and simulations. Furthermore, Q3D-FEM simulations show that the Q factor should be approximately four times higher at blue wavelengths, which is the target spectral regime for future devices.

My contribution: I designed the cavity and fabricated the mirrors that together with the GaN prisms form the microcavity. I supported the development of the base code for Q3D-FEM simulations, further developed the code, and performed all Q3D-FEM simulations in the paper and the data analysis. I wrote the manuscript with input from the other co-authors.

References

[1] T. H. Maiman, "Stimulated optical radiation in ruby," *Nature*, vol. 187, no. 4736, pp. 493–494, 1960.

[2] A. L. Schawlow and C. H. Townes, "Infrared and optical masers," *Physical Review*, vol. 112, no. 6, pp. 1940–1949, 1958.

[3] Yole Développement, "VCSELs - Market and technology trends 2020," Lyon-Villeurbanne, France, Tech. Rep., 2020.

[4] R. Michalzik, "VCSEL fundamentals," in *VCSELs: Fundamentals, Technology and Applications of Vertical-Cavity Surface-Emitting Lasers*, R. Michalzik, Ed., vol. 166, Berlin, Heidelberg: Springer Berlin Heidelberg, 2013, pp. 19–75.

[5] K. J. Ebeling, R. Michalzik, and H. Moench, "Vertical-cavity surface-emitting laser technology applications with focus on sensors and three-dimensional imaging," *Japanese Journal of Applied Physics*, vol. 57, no. 8S2, 08PA02, 2018.

[6] K. Iga, "Forty years of vertical-cavity surface-emitting laser: Invention and innovation," *Japanese Journal of Applied Physics*, vol. 57, no. 8S2, 08PA01, 2018.

[7] H. Soda, K.-i. Iga, C. Kitahara, and Y. Suematsu, "GaInAsP/InP surface emitting injection lasers," *Japanese Journal of Applied Physics*, vol. 18, no. 12, pp. 2329–2330, 1979.

[8] J. A. Tatum, A. Clark, J. K. Guenter, R. A. Hawthorne, and R. H. Johnson, "Commercialization of Honeywell's VCSEL technology," in *Proc. SPIE, Vertical-Cavity Surface-Emitting Lasers IV*, K. D. Choquette and C. Lei, Eds., vol. 3946, 2000, pp. 2–13.

[9] H. Amano, N. Sawaki, I. Akasaki, and Y. Toyoda, "Metalorganic vapor phase epitaxial growth of a high quality GaN film using an AlN buffer layer," *Applied Physics Letters*, vol. 48, no. 5, pp. 353–355, 1986.

[10] H. Amano, M. Kito, K. Hiramatsu, and I. Akasaki, "P-Type conduction in Mg-doped GaN treated with low-energy electron beam irradiation (LEEBI)," *Japanese Journal of Applied Physics*, vol. 28, no. 12A, pp. L2112–L2114, 1989.

[11] S. Nakamura, N. Iwasa, M. Senoh, and T. Mukai, "Hole compensation mechanism of p-Type GaN films," *Japanese Journal of Applied Physics*, vol. 31, no. 5A, pp. 1258–1266, 1992.

[12] S. Nakamura, T. Mukai, M. Senoh, and N. Iwasa, "Thermal annealing effects on P-type Mg-doped GaN films," *Japanese Journal of Applied Physics*, vol. 31, no. 2, pp. 139–142, 1992.

[13] S. Nakamura, T. Mukai, and M. Senoh, "Candela-class high-brightness InGaN/AlGaN double-heterostructure blue-light-emitting diodes," *Applied Physics Letters*, vol. 64, no. 13, pp. 1687–1689, 1994.

[14] S. Nakamura, M. Senoh, N. Iwasa, and S.-i. Nagahama, "High-brightness InGaN blue, green and yellow Light-Emitting Diodes with quantum well structures," *Japanese Journal of Applied Physics*, vol. 34, no. 7A, pp. L797–L799, 1995.

[15] S. Nakamura, M. Senoh, S.-i. Nagahama, N. Iwasa, T. Yamada, T. Matsushita, H. Kiyoku, and Y. Sugimoto, "InGaN-based multi-quantum-well-structure laser diodes," *Japanese Journal of Applied Physics*, vol. 35, no. 1B, pp. L74–L76, 1996.

[16] S. Nakamura, M. Senoh, S. i. Nagahama, N. Iwasa, T. Yamada, T. Matsushita, H. Kiyoku, and Y. Sugimoto, "InGaN multi-quantum-well-structure laser diodes with cleaved mirror cavity facets," *Japanese Journal of Applied Physics*, vol. 35, no. 2B, 1996.

[17] S. Nakamura, M. Senoh, S.-i. Nagahama, N. Iwasa, T. Yamada, T. Matsushita, Y. Sugimoto, and H. Kiyoku, "Room-temperature continuous-wave operation of InGaN multi-quantum-well structure laser diodes," *Applied Physics Letters*, vol. 69, no. 26, pp. 4056–4058, 1996.

[18] T.-C. Lu, C.-C. Kao, H.-C. Kuo, G.-S. Huang, and S.-C. Wang, "CW lasing of current injection blue GaN-based vertical cavity surface emitting laser," *Applied Physics Letters*, vol. 92, no. 14, p. 141 102, 2008.

[19] Y. Higuchi, K. Omae, H. Matsumura, and T. Mukai, "Room-temperature CW lasing of a GaN-based vertical-cavity surface-emitting laser by current injection," *Applied Physics Express*, vol. 1, no. 12, p. 121 102, 2008.

[20] H. Nakajima, T. Hamaguchi, M. Tanaka, M. Ito, T. Jyokawa, T. Matou, K. Hayashi, M. Ohara, N. Kobayashi, H. Watanabe, R. Koda, and K. Yanashima, "Single transverse mode operation of GaN-based vertical-cavity surface-emitting laser with monolithically incorporated curved mirror," *Applied Physics Express*, vol. 12, no. 8, p. 084 003, 2019.

[21] M. Kuramoto, S. Kobayashi, T. Akagi, K. Tazawa, H. Tanaka, and T. Takeuchi, "Nano-height cylindrical waveguide in GaN-based vertical-cavity surface-emitting lasers," *Applied Physics Express*, vol. 13, no. 8, p. 082 005, 2020.

[22] K. Terao, H. Nagai, D. Morita, S. Masui, T. Yanamoto, and S.-i. Nagahama, "Blue and green GaN-based vertical-cavity surface-emitting lasers with AlInN/GaN DBR," in *Proc. SPIE, Gallium Nitride Materials and Devices XVI*, H. Morkoç, H. Fujioka, and U. T. Schwarz, Eds., vol. 11686, SPIE, 2021, 116860E.

[23] M. Kneissl, "A brief review of III-nitride UV emitter technologies and their applications," in *III-Nitride Ultraviolet Emitters*, ser. Springer Series in Materials Science, M. Kneissl and J. Rass, Eds., vol. 227, Cham: Springer International Publishing, 2016, pp. 1–25.

[24] M. Degner and H. Ewald, "UV Emitters in gas sensing applications," in *III-Nitride Ultraviolet Emitters*, ser. Springer Series in Materials Science, M. Kneissl and J. Rass, Eds., vol. 227, Cham: Springer International Publishing, 2016, pp. 321–349.

[25] S. Khan, D. Newport, and S. Le Calvé, "Gas detection using portable deep-UV absorption spectrophotometry: A review," *Sensors*, vol. 19, no. 23, p. 5210, 2019.

[26] P. Cash, W. Krzewick, P. Machado, K. R. Overstreet, M. Silveira, M. Stanczyk, D. Taylor, and X. Zhang, "Microsemi chip scale atomic clock (CSAC) technical status, applications, and future plans," in *2018 European Frequency and Time Forum (EFTF)*, IEEE, 2018, pp. 65–71.

[27] Y. J. Park, T. Detchprohm, K. Mehta, J. Wang, H. Jeong, Y. J. Park, T. Detchprohm, K. Mehta, J. Wang, Y.-s. Liu, P. Chen, S. Wang, S.-c. Shen, D. Yoder, F. Ponce, and R. Dupuis, "Optically pumped vertical-cavity surface-emitting lasers at 375 nm with air-gap/$Al_{0.05}Ga_{0.95}N$ distributed Bragg reflectors," in *Proc. SPIE, Vertical-Cavity Surface-Emitting Lasers XXIII*, K. D. Choquette and L. A. Graham, Eds., 2019, 109389A.

[28] Y.-Y. Jau, H. Partner, P. D. D. Schwindt, J. D. Prestage, J. R. Kellogg, and N. Yu, "Low-power, miniature ^{171}Yb ion clock using an ultra-small vacuum package," *Applied Physics Letters*, vol. 101, no. 25, p. 253 518, 2012.

[29] E. Gutmann, F. Erfurth, A. Drewitz, A. Scheibe, and M. C. Meinke, "UV fluorescence detection and spectroscopy in chemistry and life sciences," in *III-Nitride Ultraviolet Emitters*, M. Kneissl and J. Rass, Eds., Springer International Publishing, 2016, pp. 351–386.

[30] S. P. Najda, P. Perlin, M. Leszczyński, T. J. Slight, W. Meredith, M. Schemmann, H. Moseley, J. A. Woods, R. Valentine, S. Kalra, P. Mossey, E. Theaker, M. Macluskey, G. Mimnagh, and W. Mimnagh, "A multi-wavelength (u.v. to visible) laser system for early detection of oral cancer," in *Proc. of SPIE, Imaging, Manipulation, and Analysis of Biomolecules, Cells, and Tissues XIII*, D. L. Farkas, D. V. Nicolau, and R. C. Leif, Eds., vol. 9328, 2015, p. 932 809.

[31] M. Panjehpour, C. E. Julius, M. N. Phan, T. Vo-Dinh, and S. Overholt, "Laser-induced fluorescence spectroscopy for in vivo diagnosis of non-melanoma skin cancers," *Lasers in Surgery and Medicine*, vol. 31, no. 5, pp. 367–373, 2002.

[32] J. R. Lakowicz, *Principles of fluorescence spectroscopy*, J. R. Lakowicz, Ed. Boston, MA: Springer US, 2006, pp. 1–954.

[33] Å. Haglund, E. Hashemi, J. Bengtsson, J. Gustavsson, M. Stattin, M. Calciati, and M. Goano, "Progress and challenges in electrically pumped GaN-based VCSELs," in *Proc. of SPIE, Semiconductor Lasers and Laser Dynamics VII*, K. Panajotov, M. Sciamanna, A. Valle, and R. Michalzik, Eds., vol. 9892, 2016, 98920Y.

[34] M. K. Hibbs-Brenner, K. L. Johnson, and M. Bendett, "VCSEL technology for medical diagnostics and therapeutics," in *Proc. of SPIE, Photons and Neurons*, A. Mahadevan-Jansen and E. D. Jansen, Eds., vol. 7180, 2009, 71800T.

[35] C. Goßler, C. Bierbrauer, R. Moser, M. Kunzer, K. Holc, W. Pletschen, K. Köhler, J. Wagner, M. Schwaerzle, P. Ruther, O. Paul, J. Neef, D. Keppeler, G. Hoch, T. Moser, and U. T. Schwarz, "GaN-based micro-LED arrays on flexible substrates for optical cochlear implants," *Journal of Physics D: Applied Physics*, vol. 47, no. 20, p. 205 401, 2014.

[36] V. Poher, N. Grossman, G. T. Kennedy, K. Nikolic, H. X. Zhang, Z. Gong, E. M. Drakakis, E. Gu, M. D. Dawson, P. M. W. French, P. Degenaar, and M. A. A. Neil, "Micro-LED arrays: a tool for two-dimensional neuron stimulation," *Journal of Physics D: Applied Physics*, vol. 41, no. 9, p. 094 014, 2008.

[37] A. Dieter, E. Klein, D. Keppeler, L. Jablonski, T. Harczos, G. Hoch, V. Rankovic, O. Paul, M. Jeschke, P. Ruther, and T. Moser, "μLED-based optical cochlear implants for spectrally selective activation of the auditory nerve," *EMBO Molecular Medicine*, vol. 12, no. 8, pp. 1–12, 2020.

[38] U. Wollina, B. Seme, A. Scheibe, and E. Gutmann, "Application of UV emitters in dermatological phototherapy," in *III-Nitride Ultraviolet Emitters*, ser. Springer Series in Materials Science, M. Kneissl and J. Rass, Eds., vol. 227, Cham: Springer International Publishing, 2016, pp. 293–319.

[39] J. M. Bae, H. M. Jung, B. Y. Hong, J. H. Lee, W. J. Choi, J. H. Lee, and G. M. Kim, "Phototherapy for vitiligo," *JAMA Dermatology*, vol. 153, no. 7, p. 666, 2017.

[40] P. Zhang and M. X. Wu, "A clinical review of phototherapy for psoriasis," *Lasers in Medical Science*, vol. 33, no. 1, pp. 173–180, 2018.

[41] M. Schreiner, I. Mewis, S. Neugart, R. Zrenner, J. Glaab, M. Wiesner, and M. A. K. Jansen, "UV-B elicitation of secondary plant metabolites," in *III-Nitride Ultraviolet Emitters*, M. Kneissl and J. Rass, Eds., Cham: Springer International Publishing, 2016, pp. 387–414.

[42] J. Kühn, A. Schutkowski, F. Hirche, A. C. Baur, N. Mielenz, and G. I. Stangl, "Non-linear increase of vitamin D content in eggs from chicks treated with increasing exposure times of ultraviolet light," *The Journal of Steroid Biochemistry and Molecular Biology*, vol. 148, pp. 7–13, 2015.

[43] F. J. García de Abajo, R. J. Hernández, I. Kaminer, A. Meyerhans, J. Rosell-Llompart, and T. Sanchez-Elsner, "Back to normal: An old physics route to reduce SARS-CoV-2 Transmission in Indoor Spaces," *ACS Nano*, vol. 14, no. 7, pp. 7704–7713, 2020.

[44] M. A. Lange, T. Kolbe, and M. Jekel, "Ultraviolet light-emitting diodes for water disinfection," in *III-Nitride Ultraviolet Emitters*, M. Kneissl and J. Rass, Eds., Cham: Springer International Publishing, 2016, pp. 267–291.

[45] W. Kowalski, *Ultraviolet germicidal irradiation handbook: UVGI for air and surface disinfection*. Springer, Berlin, Heidelberg, 2009, pp. 1–50.

[46] World Health Organization, *Preventing diarrhoea through better water, sanitation and hygiene*. 2014, pp. 1–48.

[47] H. Moench, R. Conrads, C. Deppe, G. Derra, S. Gronenborn, X. Gu, G. Heusler, J. Kolb, M. Miller, P. Pekarski, J. Pollmann-Retsch, A. Pruijmboom, and U. Weichmann, "High-power VCSEL systems and applications," in *Proc. of SPIE, High-Power Diode Laser Technology and Applications XIII*, M. S. Zediker, Ed., vol. 9348, 2015, 93480W.

[48] C. Dreyer and F. Mildner, "Application of LEDs for UV-curing," in *III-Nitride Ultraviolet Emitters*, M. Kneissl and J. Rass, Eds., Cham: Springer International Publishing, 2016, pp. 415–434.

[49] J. Zhang, Q. Hu, S. Wang, J. Tao, and M. Gou, "Digital light processing based three-dimensional printing for medical applications," *International Journal of Bioprinting*, vol. 6, no. 1, pp. 12–27, 2019.

[50] F. A. Rueggeberg, M. Giannini, C. A. G. Arrais, and R. B. T. Price, "Light curing in dentistry and clinical implications: a literature review," *Brazilian Oral Research*, vol. 31, no. suppl 1, pp. 64–91, 2017.

[51] J. J. Wierer and J. Y. Tsao, "Advantages of III-nitride laser diodes in solid-state lighting," *Physica Status Solidi (A)*, vol. 212, no. 5, pp. 980–985, 2015.

[52] P. Boulay, "AR & VR displays: a target for GaN-based VCSELs – An interview with Sony Corporation," in *i-Micronews*, https://www.i-micronews.com/ar-vr-displays-a-target-for-gan-based-vcsels-an-interview-with-sony-corporation/ (viewed 22-02-2021), 2020.

[53] S. Rehman, S. Ullah, P. Chong, S. Yongchareon, and D. Komosny, "Visible light communication: A system perspective—overview and challenges," *Sensors*, vol. 19, no. 5, p. 1153, 2019.

[54] R. Yuan and J. Ma, "Review of ultraviolet non-line-of-sight communication," *China Communications*, vol. 13, no. 6, pp. 63–75, 2016.

[55] T.-c. Wu, Y.-c. Chi, H.-y. Wang, C.-t. Tsai, and G.-r. Lin, "Blue laser diode enables underwater communication at 12.4 Gbps," *Scientific Reports*, vol. 7, p. 40 480, 2017.

[56] X. Liu, S. Yi, X. Zhou, F. Zhilai, Z.-J. Qiu, L. Hu, C. Cong, L. Zheng, R. Liu, and P. Tian, "34.5 m underwater optical wireless communication with 2.70 Gbps data rate based on a green laser with NRZ-OOK modulation," *Optics Express*, vol. 25, no. 22, p. 28 938, 2017.

[57] I. Vurgaftman and J. R. Meyer, "Band parameters for nitrogen-containing semiconductors," *Journal of Applied Physics*, vol. 94, no. 6, pp. 3675–3696, 2003.

[58] H. Morkoç, *Nitride semiconductor devices: fundamentals and applications*. Weinheim, Germany: Wiley-VCH Verlag GmbH & Co. KGaA, 2013.

[59] M. Kneissl, T.-Y. Seong, J. Han, and H. Amano, "The emergence and prospects of deep-ultraviolet light-emitting diode technologies," *Nature Photonics*, vol. 13, pp. 233–244, 2019.

[60] G. Li, W. Wang, W. Yang, Y. Lin, H. Wang, Z. Lin, and S. Zhou, "GaN-based light-emitting diodes on various substrates: a critical review," *Reports on Progress in Physics*, vol. 79, no. 5, p. 056 501, 2016.

[61] K. Sato, S. Yasue, K. Yamada, S. Tanaka, T. Omori, S. Ishizuka, S. Teramura, Y. Ogino, S. Iwayama, H. Miyake, M. Iwaya, T. Takeuchi, S. Kamiyama, and I. Akasaki, "Room-temperature operation of AlGaN ultraviolet-B laser diode at 298 nm on lattice-relaxed $Al_{0.6}Ga_{0.4}N$/AlN/sapphire," *Applied Physics Express*, vol. 13, no. 3, p. 031 004, 2020.

[62] S. Tanaka, Y. Kawase, S. Teramura, S. Iwayama, K. Sato, S. Yasue, T. Omori, M. Iwaya, T. Takeuchi, S. Kamiyama, I. Akasaki, and H. Miyake, "Effect of dislocation density on optical gain and internal loss of AlGaN-based ultraviolet-B band lasers," *Applied Physics Express*, vol. 13, no. 4, p. 045 504, 2020.

[63] P. Perlin, L. Marona, M. Leszczynski, T. Suski, P. Wisniewski, R. Czernecki, and I. Grzegory, "Degradation mechanisms of InGaN laser diodes," *Proceedings of the IEEE*, vol. 98, no. 7, pp. 1214–1219, 2010.

[64] J. Enslin, F. Mehnke, A. Mogilatenko, K. Bellmann, M. Guttmann, C. Kuhn, J. Rass, N. Lobo-Ploch, T. Wernicke, M. Weyers, and M. Kneissl, "Metamorphic $Al_{0.5}Ga_{0.5}N$:Si on AlN/sapphire for the growth of UVB LEDs," *Journal of Crystal Growth*, vol. 464, pp. 185–189, 2017.

[65] A. Mogilatenko, J. Enslin, A. Knauer, F. Mehnke, K. Bellmann, T. Wernicke, M. Weyers, and M. Kneissl, "V-pit to truncated pyramid transition in AlGaN-based heterostructures," *Semiconductor Science and Technology*, vol. 30, no. 11, p. 114 010, 2015.

[66] G. S. Huang, T. C. Lu, H. H. Yao, H. C. Kuo, S. C. Wang, C.-W. Lin, and L. Chang, "Crack-free GaN/AlN distributed Bragg reflectors incorporated with GaN/AlN superlattices grown by metalorganic chemical vapor deposition," *Applied Physics Letters*, vol. 88, no. 6, p. 061 904, 2006.

[67] Z. Y. Li, T. C. Lu, H. C. Kuo, S. C. Wang, M. H. Lo, and K. M. Lau, "HRTEM investigation of high-reflectance AlN/GaN distributed Bragg-reflectors by inserting AlN/GaN superlattice," *Journal of Crystal Growth*, vol. 311, no. 10, pp. 3089–3092, 2009.

[68] K. Hiramatsu, "Epitaxial lateral overgrowth techniques used in group III nitride epitaxy," *Journal of Physics: Condensed Matter*, vol. 13, no. 32, pp. 6961–6975, 2001.

[69] U. Zeimer, V. Kueller, A. Knauer, A. Mogilatenko, M. Weyers, and M. Kneissl, "High quality AlGaN grown on ELO AlN/sapphire templates," *Journal of Crystal Growth*, vol. 377, pp. 32–36, 2013.

[70] H. Miyake, G. Nishio, S. Suzuki, K. Hiramatsu, H. Fukuyama, J. Kaur, and N. Kuwano, "Annealing of an AlN buffer layer in N_2-CO for growth of a high-quality AlN film on sapphire," *Applied Physics Express*, vol. 9, no. 2, 2016.

[71] M. Khalilian, Z. Bi, J. Johansson, F. Lenrick, O. Hultin, J. Colvin, R. Timm, R. Wallenberg, J. Ohlsson, M.-E. Pistol, A. Gustafsson, and L. Samuelson, "Dislocation-Free and atomically flat GaN hexagonal microprisms for device applications," *Small*, vol. 16, no. 30, p. 1 907 364, 2020.

[72] P.-M. Coulon, B. Alloing, V. Brändli, P. Vennéguès, M. Leroux, and J. Zúñiga-Pérez, "Dislocation filtering and polarity in the selective area growth of GaN nanowires by continuous-flow metal organic vapor phase epitaxy," *Applied Physics Express*, vol. 9, no. 1, p. 015 502, 2016.

[73] R. Colby, Z. Liang, I. H. Wildeson, D. A. Ewoldt, T. D. Sands, R. E. Garcia, and E. A. Stach, "Dislocation filtering in GaN nanostructures," *Nano Letters*, vol. 10, no. 5, pp. 1568–1573, 2010.

[74] C. G. Van de Walle and J. Neugebauer, "First-principles calculations for defects and impurities: Applications to III-nitrides," *Journal of Applied Physics*, vol. 95, no. 8, pp. 3851–3879, 2004.

[75] F. Mehnke, X. T. Trinh, H. Pingel, T. Wernicke, E. Janzén, N. T. Son, and M. Kneissl, "Electronic properties of Si-doped $Al_xGa_{1-x}N$ with aluminum mole fractions above 80%," *Journal of Applied Physics*, vol. 120, no. 14, p. 145 702, 2016.

[76] M. L. Nakarmi, N. Nepal, J. Y. Lin, and H. X. Jiang, "Photoluminescence studies of impurity transitions in Mg-doped AlGaN alloys," *Applied Physics Letters*, vol. 94, no. 9, p. 091 903, 2009.

[77] A. David, N. G. Young, C. Lund, and M. D. Craven, "Review—The physics of recombinations in III-nitride emitters," *ECS Journal of Solid State Science and Technology*, vol. 9, no. 1, p. 016 021, 2020.

[78] Q. Dai, M. F. Schubert, M. H. Kim, J. K. Kim, E. F. Schubert, D. D. Koleske, M. H. Crawford, S. R. Lee, A. J. Fischer, G. Thaler, and M. A. Banas, "Internal quantum efficiency and nonradiative recombination coefficient of GaInN/GaN multiple quantum wells with different dislocation densities," *Applied Physics Letters*, vol. 94, no. 11, p. 111 109, 2009.

[79] A. Bojarska-Cieślińska, Ł. Marona, J. Smalc-Koziorowska, S. Grzanka, J. Weyher, D. Schiavon, and P. Perlin, "Role of dislocations in nitride laser diodes with different indium content," *Scientific Reports*, vol. 11, p. 21, 2021.

[80] C. Haller, J.-F. Carlin, G. Jacopin, W. Liu, D. Martin, R. Butté, and N. Grandjean, "GaN surface as the source of non-radiative defects in InGaN/GaN quantum wells," *Applied Physics Letters*, vol. 113, no. 11, p. 111 106, 2018.

[81] S. Adachi, "Lattice thermal conductivity of group-IV and III–V semiconductor alloys," *Journal of Applied Physics*, vol. 102, no. 6, p. 063 502, 2007.

[82] J. Zou, D. Kotchetkov, A. A. Balandin, D. I. Florescu, and F. H. Pollak, "Thermal conductivity of GaN films: Effects of impurities and dislocations," *Journal of Applied Physics*, vol. 92, no. 5, pp. 2534–2539, 2002.

[83] A. Bao, "Group III-nitride nanowires," *Materials Science and Technology*, vol. 33, no. 7, pp. 765–776, 2017.

[84] M. T. Björk, B. J. Ohlsson, T. Sass, A. I. Persson, C. Thelander, M. H. Magnusson, K. Deppert, L. R. Wallenberg, and L. Samuelson, "One-dimensional steeplechase for electrons realized," *Nano Letters*, vol. 2, no. 2, pp. 87–89, 2002.

[85] L. A. Coldren, S. W. Corzine, and M. L. Mašanović, *Diode lasers and photonic integrated circuits*. Hoboken, NJ, USA: John Wiley & Sons, Inc., 2012.

[86] G. R. Hadley, "Effective index model for vertical-cavity surface-emitting lasers," *Optics Letters*, vol. 20, no. 13, p. 1483, 1995.

[87] O. Marek and W. Nakwaski, "Thermal effects in vertical-cavity surface-emitting lasers," in *Current Trends in Vertical Cavity Surface Emitting Lasers*, T. P. Lee, Ed., World Scientific Publishing, Singapore, 1995, pp. 139–202.

[88] E. Hashemi, J. Bengtsson, J. Gustavsson, M. Stattin, G. Cosendey, N. Grandjean, and Å. Haglund, "Analysis of structurally sensitive loss in GaN-based VCSEL cavities and its effect on modal discrimination," *Optics Express*, vol. 22, no. 1, p. 411, 2014.

[89] N. Hayashi, J. Ogimoto, K. Matsui, T. Furuta, T. Akagi, S. Iwayama, T. Takeuchi, S. Kamiyama, and M. Iwaya, "A GaN-based VCSEL with a convex structure for optical guiding," vol. 215, no. 10, p. 1 700 648, 2018.

[90] T. Christopoulos, O. Tsilipakos, G. Sinatkas, and E. E. Kriezis, "On the calculation of the quality factor in contemporary photonic resonant structures," *Optics Express*, vol. 27, no. 10, p. 14 505, 2019.

[91] J. M. Redwing, D. A. S. Loeber, N. G. Anderson, M. A. Tischler, and J. S. Flynn, "An optically pumped GaN–AlGaN vertical cavity surface emitting laser," *Applied Physics Letters*, vol. 69, no. 1, pp. 1–3, 1996.

[92] T. Someya, R. Werner, A. Forchel, M. Catalano, R. Cingolani, and Y. Arakawa, "Room temperature lasing at blue wavelengths in gallium nitride microcavities," *Science*, vol. 285, no. 5435, pp. 1905–1906, 1999.

[93] M. A. Khan, J. N. Kuznia, J. M. Van Hove, and D. T. Olson, "Reflective filters based on single-crystal GaN/$Al_xGa_{1-x}N$ multilayers deposited using low-pressure metalorganic chemical vapor deposition," *Applied Physics Letters*, vol. 59, no. 12, pp. 1449–1451, 1991.

[94] R. Butté, E. Feltin, J. Dorsaz, G. Christmann, J.-F. Carlin, N. Grandjean, and M. Ilegems, "Recent progress in the growth of highly reflective nitride-based distributed Bragg reflectors and their use in microcavities," *Japanese Journal of Applied Physics*, vol. 44, no. 10, pp. 7207–7216, 2005.

[95] T. Ive, O. Brandt, H. Kostial, T. Hesjedal, M. Ramsteiner, and K. H. Ploog, "Crack-free and conductive Si-doped AlN/GaN distributed Bragg reflectors grown on 6H-SiC(0001)," *Applied Physics Letters*, vol. 85, no. 11, pp. 1970–1972, 2004.

[96] G. Brummer, D. Nothern, A. Y. Nikiforov, and T. D. Moustakas, "Deep ultraviolet distributed Bragg reflectors based on graded composition AlGaN alloys," *Applied Physics Letters*, vol. 106, no. 22, p. 221 107, 2015.

[97] A. Franke, M. P. Hoffmann, R. Kirste, M. Bobea, J. Tweedie, F. Kaess, M. Gerhold, R. Collazo, and Z. Sitar, "High reflectivity III-nitride UV-C distributed Bragg reflectors for vertical cavity emitting lasers," *Journal of Applied Physics*, vol. 120, no. 13, p. 135 703, 2016.

[98] T. Detchprohm, Y.-S. Liu, K. Mehta, S. Wang, H. Xie, T.-T. Kao, S.-C. Shen, P. D. Yoder, F. A. Ponce, and R. D. Dupuis, "Sub 250 nm deep-UV AlGaN/AlN distributed Bragg reflectors," *Applied Physics Letters*, vol. 110, no. 1, p. 011 105, 2017.

[99] G. Schmidt, C. Berger, A. Dadgar, F. Bertram, P. Veit, S. Metzner, A. Strittmatter, J. Christen, S. T. Jagsch, M. R. Wagner, and A. Hoffmann, "Nitride microcavities and single quantum dots for classical and non-classical light emitters," in *Semiconductor Nanophotonics*, ser. Springer Series in Solid-State Sciences, M. Kneissl, A. Knorr, S. Reitzenstein, and A. Hoffmann, Eds., vol. 194, Cham: Springer International Publishing, 2020, p. 390.

[100] N. Nakada, H. Ishikawa, T. Egawa, and T. Jimbo, "Suppression of crack generation in GaN/AlGaN distributed Bragg reflector on sapphire by the insertion of GaN/AlGaN superlattice grown by metal-organic chemical vapor deposition," *Japanese Journal of Applied Physics*, vol. 42, no. 2B, pp. L144–L146, 2003.

[101] H. S. Cheong, T. V. Cuong, H. G. Kim, J. Y. Park, C. S. Kim, C. H. Hong, J. H. Baek, S. H. Lee, T. H. Kim, and Y. M. Yu, "Suppression of cracks and V-shaped defects, and improvement of reflectivity of GaN/AlGaN distributed Bragg reflectors by insertion of multiple interlayers," *Physica Status Solidi (A)*, vol. 201, no. 12, pp. 2799–2802, 2004.

[102] O. Mitrofanov, S. Schmult, M. J. Manfra, T. Siegrist, N. G. Weimann, A. M. Sergent, and R. J. Molnar, "High-reflectivity ultraviolet AlGaN/AlGaN distributed Bragg reflectors," *Applied Physics Letters*, vol. 88, no. 17, p. 171 101, 2006.

[103] A. Bhattacharyya, S. Iyer, E. Iliopoulos, A. V. Sampath, J. Cabalu, T. D. Moustakas, and I. Friel, "High reflectivity and crack-free AlGaN/AlN ultraviolet distributed Bragg reflectors," *Journal of Vacuum Science and Technology B: Microelectronics and Nanometer Structures*, vol. 20, no. 3, pp. 1229–1233, 2002.

[104] T. Ive, O. Brandt, X. Kong, A. Trampert, and K. H. Ploog, "(Al,In)N layers and (Al,In)N/GaN heterostructures grown by plasma-assisted molecular beam epitaxy on 6H-SiC(0001)," *Physical Review B*, vol. 78, no. 3, p. 035 311, 2008.

[105] K. Hiraiwa, W. Muranaga, S. Iwayama, T. Takeuchi, S. Kamiyama, M. Iwaya, and I. Akasaki, "In situ wafer curvature measurement and strain control of AlInN/GaN distributed Bragg reflectors," *Applied Physics Express*, vol. 13, no. 5, p. 055 506, 2020.

[106] T. Akagi, Y. Kozuka, K. Ikeyama, S. Iwayama, M. Kuramoto, T. Saito, T. Tanaka, T. Takeuchi, S. Kamiyama, M. Iwaya, and I. Akasaki, "High-quality AlInN/GaN distributed Bragg reflectors grown by metalorganic vapor phase epitaxy," *Applied Physics Express*, vol. 13, no. 12, p. 125 504, 2020.

[107] J.-F. Carlin, C. Zellweger, J. Dorsaz, S. Nicolay, G. Christmann, E. Feltin, R. Butté, and N. Grandjean, "Progresses in III-nitride distributed Bragg reflectors and microcavities using AlInN/GaN materials," *Physica Status Solidi (B)*, vol. 242, no. 11, pp. 2326–2344, 2005.

[108] G. Cosendey, A. Castiglia, G. Rossbach, J.-F. Carlin, and N. Grandjean, "Blue monolithic AlInN-based vertical cavity surface emitting laser diode on free-standing GaN substrate," *Applied Physics Letters*, vol. 101, no. 15, p. 151 113, 2012.

[109] M. Kuramoto, S. Kobayashi, T. Akagi, K. Tazawa, K. Tanaka, T. Saito, and T. Takeuchi, "High-output-power and high-temperature operation of blue GaN-based vertical-cavity surface-emitting laser," *Applied Physics Express*, vol. 11, no. 11, p. 112 101, 2018.

[110] E. Feltin, J.-F. Carlin, J. Dorsaz, G. Christmann, R. Butté, M. Laügt, M. Ilegems, and N. Grandjean, "Crack-free highly reflective AlInN/AlGaN Bragg mirrors for UV applications," *Applied Physics Letters*, vol. 88, no. 5, p. 051 108, 2006.

[111] Y. Zhang, S. W. Ryu, C. Yerino, B. Leung, Q. Sun, Q. Song, H. Cao, and J. Han, "A conductivity-based selective etching for next generation GaN devices," *Physica Status Solidi (B)*, vol. 247, no. 7, pp. 1713–1716, 2010.

[112] M. A. Bergmann, J. Enslin, R. Yapparov, F. Hjort, B. Wickman, S. Marcinkevičius, T. Wernicke, M. Kneissl, and Å. Haglund, "Electrochemical etching of AlGaN for the realization of thin-film devices," *Applied Physics Letters*, vol. 115, no. 18, p. 182 103, 2019.

[113] C. Zhang, S. H. Park, D. Chen, D. W. Lin, W. Xiong, H. C. Kuo, C. F. Lin, H. Cao, and J. Han, "Mesoporous GaN for photonic engineering-highly reflective GaN mirrors as an example," *ACS Photonics*, vol. 2, no. 7, pp. 980–986, 2015.

[114] T. Braniste, J. Ciers, E. Monaico, D. Martin, J. F. Carlin, V. V. Ursaki, V. V. Sergentu, I. M. Tiginyanu, and N. Grandjean, "Multilayer porous structures of HVPE and MOCVD grown GaN for photonic applications," *Superlattices and Microstructures*, vol. 102, pp. 221–234, 2017.

[115] F. H. Fan, Z. Y. Syu, C. J. Wu, Z. J. Yang, B. S. Huang, G. J. Wang, Y. S. Lin, H. Chen, C. Hauer Kao, and C. F. Lin, "Ultraviolet GaN light-emitting diodes with porous-AlGaN reflectors," *Scientific Reports*, vol. 7, p. 4968, 2017.

[116] P. H. Griffin and R. Oliver, "Porous nitride semiconductors reviewed," *Journal of Physics D: Applied Physics*, vol. 53, p. 383 002, 2020.

[117] S. Mishkat-Ul-Masabih, T. S. Luk, A. Rishinaramangalam, M. Monavarian, M. Nami, and D. Feezell, "Nanoporous distributed Bragg reflectors on free-standing nonpolar m-plane GaN," *Applied Physics Letters*, vol. 112, no. 4, p. 041 109, 2018.

[118] S. M. Mishkat-Ul-Masabih, A. A. Aragon, M. Monavarian, T. S. Luk, and D. F. Feezell, "Electrically injected nonpolar GaN-based VCSELs with lattice-matched nanoporous distributed Bragg reflector mirrors," *Applied Physics Express*, vol. 12, no. 3, p. 036 504, 2019.

[119] R. T. Elafandy, J. H. Kang, B. Li, T. K. Kim, J. S. Kwak, and J. Han, "Room-temperature operation of c-plane GaN vertical cavity surface emitting laser on conductive nanoporous distributed Bragg reflector," *Applied Physics Letters*, vol. 117, no. 1, p. 011 101, 2020.

[120] C. Zhang, R. T. El Afandy, J. Zhang, S. Chen, A. Nurmikko, and J. Han, "Development of nanopore-based near ultraviolet vertical-cavity surface emitting lasers," in *Proc. of SPIE, Gallium Nitride Materials and Devices XIV*, H. Morkoç, H. Fujioka, and U. T. Schwarz, Eds., SPIE, 2019, p. 57.

[121] C. Xiong, P. R. Edwards, G. Christmann, E. Gu, M. D. Dawson, J. J. Baumberg, R. W. Martin, and I. M. Watson, "High-reflectivity GaN/air vertical distributed Bragg reflectors fabricated by wet etching of sacrificial AlInN layers," *Semiconductor Science and Technology*, vol. 25, no. 3, p. 032 001, 2010.

[122] P. Griffin, T. Zhu, and R. Oliver, "Porous AlGaN-based ultraviolet distributed Bragg reflectors," *Materials*, vol. 11, no. 9, p. 1487, 2018.

[123] Y. Li, C. Wang, Y. Zhang, P. Hu, S. Zhang, M. Du, X. Su, Q. Li, and F. Yun, "Analysis of TM/TE mode enhancement and droop reduction by a nanoporous n-AlGaN underlayer in a 290 nm UV-LED," *Photonics Research*, vol. 8, no. 6, p. 806, 2020.

[124] C. J. Wu, C. Y. Kuo, C. J. Wang, W. E. Chang, C. L. Tsai, C. F. Lin, and J. Han, "Deep-UV porous AlGaN distributed Bragg reflectors for deep ultraviolet light-emitting diodes and laser diodes," *ACS Applied Nano Materials*, vol. 3, no. 1, pp. 399–402, 2020.

[125] D. Adolph, R. R. Zamani, K. A. Dick, and T. Ive, "Hybrid ZnO/GaN distributed Bragg reflectors grown by plasma-assisted molecular beam epitaxy," *APL Materials*, vol. 4, no. 8, p. 086 106, 2016.

[126] E. O. Filatova and A. S. Konashuk, "Interpretation of the changing the band gap of Al_2O_3 depending on its crystalline form: connection with different local symmetries," *Journal of Physical Chemistry C*, vol. 119, no. 35, pp. 20 755–20 761, 2015.

[127] P. Laha, A. B. Panda, S. K. Mahapatra, P. K. Barhai, A. K. Das, and I. Banerjee, "Development of rf plasma sputtered Al_2O_3-TiO_2 multilayer broad band antireflecting coatings and its correlation with plasma parameters," *Applied Surface Science*, vol. 258, no. 7, pp. 2275–2282, 2012.

[128] A. A. Akl, H. Kamal, and K. Abdel-Hady, "Fabrication and characterization of sputtered titanium dioxide films," *Applied Surface Science*, vol. 252, no. 24, pp. 8651–8656, 2006.

[129] S. V. Chandra, S. Uthanna, and G. M. Rao, "Effect of substrate temperature on the structural, optical and electrical properties of dc magnetron sputtered tantalum oxide films," *Applied Surface Science*, vol. 254, no. 7, pp. 1953–1960, 2008.

[130] L. V. Rodríguez-de Marcos, J. I. Larruquert, J. A. Méndez, and J. A. Aznárez, "Self-consistent optical constants of SiO_2 and Ta_2O_5 films," *Optical Materials Express*, vol. 6, no. 11, p. 3622, 2016.

[131] K. N. Chen, C. M. Hsu, J. Liu, Y. C. Liou, and C. F. Yang, "Investigation of antireflection Nb_2O_5 thin films by the sputtering method under different deposition parameters," *Micromachines*, vol. 7, no. 9, p. 151, 2016.

[132] V. Gritsenko, D. Gritsenko, S. Shaimeev, V. Aliev, K. Nasyrov, S. Erenburg, V. Tapilin, H. Wong, M. C. Poon, J. H. Lee, J. W. Lee, and C. W. Kim, "Atomic and electronic structures of amorphous ZrO_2 and HfO_2 films," *Microelectronic Engineering*, vol. 81, no. 2-4, pp. 524–529, 2005.

[133] M. Jerman, Z. Qiao, and D. Mergel, "Refractive index of thin films of SiO_2, ZrO_2, and HfO_2 as a function of the films' mass density," *Applied Optics*, vol. 44, no. 15, p. 3006, 2005.

[134] S. Heo, E. Cho, H. I. Lee, G. S. Park, H. J. Kang, T. Nagatomi, P. Choi, and B. D. Choi, "Band gap and defect states of MgO thin films investigated using reflection electron energy loss spectroscopy," *AIP Advances*, vol. 5, no. 7, p. 077 167, 2015.

[135] R. Stephens and I. Malitson, "Index of refraction of magnesium oxide," *Journal of Research of the National Bureau of Standards*, vol. 49, no. 4, p. 249, 1952.

[136] G. Xu, P. Jin, M. Tazawa, and K. Yoshimura, "Optical investigation of silicon nitride thin films deposited by r.f. magnetron sputtering," *Thin Solid Films*, vol. 425, no. 1-2, pp. 196–202, 2003.

[137] V. H. Mudavakkat, V. V. Atuchin, V. N. Kruchinin, A. Kayani, and C. V. Ramana, "Structure, morphology and optical properties of nanocrystalline yttrium oxide (Y_2O_3) thin films," *Optical Materials*, vol. 34, no. 5, pp. 893–900, 2012.

[138] Z. A. Weinberg, G. W. Rubloff, and E. Bassous, "Transmission, photoconductivity, and the experimental band gap of thermally grown SiO_2 films," *Physical Review B*, vol. 19, no. 6, pp. 3107–3117, 1979.

[139] T. Hamaguchi, H. Nakajima, M. Tanaka, M. Ito, M. Ohara, T. Jyoukawa, N. Kobayashi, T. Matou, K. Hayashi, H. Watanabe, R. Koda, and K. Yanashima, "Sub-milliampere-threshold continuous wave operation of GaN-based vertical-cavity surface-emitting laser with lateral optical confinement by curved mirror," *Applied Physics Express*, vol. 12, no. 4, p. 044 004, 2019.

[140] S. Izumi, N. Fuutagawa, T. Hamaguchi, M. Murayama, M. Kuramoto, and H. Narui, "Room-temperature continuous-wave operation of GaN-based vertical-cavity surface-emitting lasers fabricated using epitaxial lateral overgrowth," *Applied Physics Express*, vol. 8, no. 6, p. 062 702, 2015.

[141] T. Onishi, O. Imafuji, K. Nagamatsu, M. Kawaguchi, K. Yamanaka, and S. Takigawa, "Continuous wave operation of GaN vertical cavity surface emitting lasers at room temperature," *IEEE Journal of Quantum Electronics*, vol. 48, no. 9, pp. 1107–1112, 2012.

[142] T.-C. Chang, E. Hashemi, K.-B. Hong, J. Bengtsson, J. Gustavsson, Å. Haglund, and T.-C. Lu, "Electrically injected GaN-based vertical-cavity surface-emitting lasers with TiO_2 high-index-contrast grating reflectors," *ACS Photonics*, vol. 7, no. 4, pp. 861–866, 2020.

[143] J. Cho, J. H. Park, J. K. Kim, and E. F. Schubert, "White light-emitting diodes: History, progress, and future," *Laser & Photonics Reviews*, vol. 11, no. 2, p. 1 600 147, 2017.

[144] G. Weng, Y. Mei, J. Liu, W. Hofmann, L. Ying, J. Zhang, Y. Bu, Z. Li, and B. Zhang, "Low threshold continuous-wave lasing of surface-emitting lasers," *Optics Express*, vol. 24, no. 14, pp. 15 546–15 553, 2016.

[145] T. Ueda, M. Ishida, and M. Yuri, "Separation of thin GaN from sapphire by laser lift-off technique," *Japanese Journal of Applied Physics*, vol. 50, no. 4, p. 041 001, 2011.

[146] K. Omae, Y. Higuchi, K. Nakagawa, H. Matsumura, and T. Mukai, "Improvement in lasing characteristics of GaN-based vertical-cavity surface-emitting lasers fabricated using a GaN substrate," *Applied Physics Express*, vol. 2, no. 5, pp. 6–9, 2009.

[147] H. K. Cho, O. Krüger, A. Külberg, J. Rass, U. Zeimer, T. Kolbe, A. Knauer, S. Einfeldt, M. Weyers, and M. Kneissl, "Chip design for thin-film deep ultraviolet LEDs fabricated by laser lift-off of the sapphire substrate," *Semiconductor Science and Technology*, vol. 32, no. 12, 12LT01, 2017.

[148] Z. Zheng, Y. Li, and O. Paul, "Loss analysis in nitride deep ultraviolet planar cavity," *Journal of Nanophotonics*, vol. 12, no. 4, p. 043 504, 2018.

[149] Z. Zheng, H. Long, S. Matta, M. Leroux, J. Brault, L. Ying, Z. Zheng, and B. Zhang, "Photoassisted chemical smoothing of AlGaN surface after laser lift-off," *Journal of Vacuum Science & Technology B*, vol. 38, no. 4, p. 042 207, 2020.

[150] J. T. Leonard, D. A. Cohen, B. P. Yonkee, R. M. Farrell, T. Margalith, S. Lee, S. P. DenBaars, J. S. Speck, and S. Nakamura, "Nonpolar III-nitride vertical-cavity surface-emitting lasers incorporating an ion implanted aperture," *Applied Physics Letters*, vol. 107, no. 1, p. 011 102, 2015.

[151] S. Lee, C. A. Forman, J. Kearns, J. T. Leonard, D. A. Cohen, S. Nakamura, and S. P. DenBaars, "Demonstration of GaN-based vertical-cavity surface-emitting lasers with buried tunnel junction contacts," *Optics Express*, vol. 27, no. 22, p. 31 621, 2019.

[152] J. A. Kearns, J. Back, D. A. Cohen, S. P. DenBaars, and S. Nakamura, "Demonstration of blue semipolar $(20\bar{2}\bar{1})$ GaN-based vertical-cavity surface-emitting lasers," *Optics Express*, vol. 27, no. 17, p. 23 707, 2019.

[153] C. Holder, J. S. Speck, S. P. DenBaars, S. Nakamura, and D. Feezell, "Demonstration of nonpolar GaN-based vertical-cavity surface-emitting lasers," *Applied Physics Express*, vol. 5, no. 9, K. D. Choquette and J. K. Guenter, Eds., p. 092 104, 2012.

[154] S. Okur, R. Shimada, F. Zhang, S. D. A. Hafiz, J. Lee, V. Avrutin, H. Morkoç, A. Franke, F. Bertram, J. Christen, and Ü. Özgür, "GaN-Based vertical cavities with all dielectric reflectors by epitaxial lateral overgrowth," *Japanese Journal of Applied Physics*, vol. 52, no. 8S, 08JH03, 2013.

[155] S. Heikman, S. Keller, S. Newman, Y. Wu, C. Moe, B. Moran, M. Schmidt, U. K. Mishra, J. S. Speck, and S. P. DenBaars, "Epitaxial lateral overgrowth of high Al composition AlGaN alloys on deep grooved SiC substrates," *Japanese Journal of Applied Physics*, vol. 44, no. 13, pp. L405–L407, 2005.

[156] V. Kueller, A. Knauer, U. Zeimer, H. Rodriguez, A. Mogilatenko, M. Kneissl, and M. Weyers, "(Al,Ga)N overgrowth over AlN ridges oriented in [1120] and [1100] direction," *Physica Status Solidi (C)*, vol. 8, no. 7-8, pp. 2022–2024, 2011.

[157] C. J. Chang-Hasnain and W. Yang, "High-contrast gratings for integrated optoelectronics," *Advances in Optics and Photonics*, vol. 4, no. 3, p. 379, 2012.

[158] M. Gębski, M. Dems, A. Szerling, M. Motyka, L. Marona, R. Kruszka, D. Urbańczyk, M. Walczakowski, N. Pałka, A. Wójcik-Jedlińska, Q. J. Wang, D. H. Zhang, M. Bugajski, M. Wasiak, and T. Czyszanowski, "Monolithic high-index contrast grating: a material independent high-reflectance VCSEL mirror," *Optics Express*, vol. 23, no. 9, p. 11 674, 2015.

[159] J. Lee, S. Ahn, H. Chang, J. Kim, Y. Park, and H. Jeon, "Polarization-dependent GaN surface grating reflector for short wavelength applications," *Optics Express*, vol. 17, no. 25, p. 22 535, 2009.

[160] J. T. Leonard, D. A. Cohen, B. P. Yonkee, R. M. Farrell, S. P. DenBaars, J. S. Speck, and S. Nakamura, "Smooth e-beam-deposited tin-doped indium oxide for III-nitride vertical-cavity surface-emitting laser intracavity contacts," *Journal of Applied Physics*, vol. 118, no. 14, p. 145 304, 2015.

[161] S. Rajan and T. Takeuchi, "III-nitride tunnel junctions and their applications," *Topics in Applied Physics*, vol. 133, pp. 209–238, 2017.

[162] J. T. Leonard, E. C. Young, B. P. Yonkee, D. A. Cohen, T. Margalith, S. P. DenBaars, J. S. Speck, and S. Nakamura, "Demonstration of a III-nitride vertical-cavity surface-emitting laser with a III-nitride tunnel junction intracavity contact," *Applied Physics Letters*, vol. 107, no. 9, p. 091 105, 2015.

[163] C.-C. Shen, Y.-T. Lu, Y.-W. Yeh, C.-Y. Chen, Y.-T. Chen, C.-W. Sher, P.-T. Lee, Y.-H. Shih, T.-C. Lu, T. Wu, C.-H. Chiu, and H.-C. Kuo, "Design and fabrication of the reliable GaN based vertical-cavity surface-emitting laser via tunnel junction," *Crystals*, vol. 9, no. 4, p. 187, 2019.

[164] K. Kiyohara, M. Odawara, T. Takeuchi, S. Kamiyama, M. Iwaya, I. Akasaki, and T. Saito, "Room-temperature continuous-wave operations of GaN-based vertical-cavity surface-emitting lasers with buried GaInN tunnel junctions," *Applied Physics Express*, vol. 13, no. 11, p. 111 003, 2020.

[165] Y. Zhang, Z. Jamal-Eddine, F. Akyol, S. Bajaj, J. M. Johnson, G. Calderon, A. A. Allerman, M. W. Moseley, A. M. Armstrong, J. Hwang, and S. Rajan, "Tunnel-injected sub 290 nm ultra-violet light emitting diodes with 2.8% external quantum efficiency," *Applied Physics Letters*, vol. 112, no. 7, p. 071 107, 2018.

[166] C. Kuhn, L. Sulmoni, M. Guttmann, J. Glaab, N. Susilo, T. Wernicke, M. Weyers, and M. Kneissl, "MOVPE-grown AlGaN-based tunnel heterojunctions enabling fully transparent UVC LEDs," *Photonics Research*, vol. 7, no. 5, B7, 2019.

[167] E. A. Clinton, Z. Engel, E. Vadiee, J. V. Carpenter, Z. C. Holman, and W. A. Doolittle, "Ultra-wide-bandgap AlGaN homojunction tunnel diodes with negative differential resistance," *Applied Physics Letters*, vol. 115, no. 8, p. 082 104, 2019.

[168] A. Pandey, J. Gim, R. Hovden, and Z. Mi, "An AlGaN tunnel junction light emitting diode operating at 255 nm," *Applied Physics Letters*, vol. 117, no. 24, p. 241 101, 2020.

[169] Y. Zhang, Z. Jamal-eddine, and S. Rajan, "Recent progress of tunnel junction-based ultra-violet light emitting diodes," *Japanese Journal of Applied Physics*, vol. 58, no. SC, SC0805, 2019.

[170] E. Hashemi, J. Bengtsson, J. Gustavsson, M. Calciati, M. Goano, and Å. Haglund, "Thermal lensing effects on lateral leakage in GaN-based vertical-cavity surface-emitting laser cavities," *Opt. Express*, vol. 25, no. 9, pp. 9556–9568, 2017.

[171] S.-C. Wang, T.-C. Lu, C.-C. Kao, J.-T. Chu, G.-S. Huang, H.-C. Kuo, S.-W. Chen, T.-T. Kao, J.-R. Chen, and L.-F. Lin, "Optically pumped GaN-based vertical cavity surface emitting lasers: Technology and characteristics," *Japanese Journal of Applied Physics*, vol. 46, no. 8B, pp. 5397–5407, 2007.

[172] S. Mishkat-Ul-Masabih, A. Aragon, M. Monavarian, T. Luk, and D. F. Feezell, "Nonpolar GaN-based VCSELs with lattice-matched nanoporous distributed Bragg reflector mirrors," in *Gallium Nitride Materials and Devices XV*, H. Morkoç, H. Fujioka, and U. T. Schwarz, Eds., SPIE, 2020, p. 16.

[173] J. A. Kearns, J. Back, N. C. Palmquist, D. A. Cohen, S. P. DenBaars, and S. Nakamura, "Inhomogeneous current injection and filamentary lasing of semipolar $(20\bar{2}\bar{1})$ blue GaN-based vertical-cavity surface-emitting lasers with buried tunnel junctions," *Physica Status Solidi (A)*, vol. 1900718, pp. 1–6, 2019.

[174] J. T. Leonard, B. P. Yonkee, D. A. Cohen, L. Megalini, S. Lee, J. S. Speck, S. P. Denbaars, and S. Nakamura, "Nonpolar III-nitride vertical-cavity surface-emitting laser with a photoelectrochemically etched air-gap aperture," *Applied Physics Letters*, vol. 108, no. 3, 2016.

[175] T.-C. Lu, S.-W. Chen, T.-T. Wu, P.-M. Tu, C.-K. Chen, C.-H. Chen, Z.-Y. Li, H.-C. Kuo, and S.-C. Wang, "Continuous wave operation of current injected GaN vertical cavity surface emitting lasers at room temperature," *Applied Physics Letters*, vol. 97, no. 7, p. 071 114, 2010.

[176] D. Kasahara, D. Morita, T. Kosugi, K. Nakagawa, J. Kawamata, Y. Higuchi, H. Matsumura, and T. Mukai, "Demonstration of blue and green GaN-based vertical-cavity surface-emitting lasers by current injection at room temperature," *Applied Physics Express*, vol. 4, no. 7, p. 072 103, 2011.

[177] W.-J. Liu, X.-L. Hu, L. Y. Ying, J.-Y. Zhang, and B.-P. Zhang, "Room temperature continuous wave lasing of electrically injected GaN-based vertical cavity surface emitting lasers," *Applied Physics Letters*, vol. 104, no. 25, p. 251 116, 2014.

[178] D. H. Hsieh, A. J. Tzou, T. S. Kao, F. I. Lai, D. W. Lin, B. C. Lin, T. C. Lu, W. C. Lai, C. H. Chen, and H. C. Kuo, "Improved carrier injection in GaN-based VCSEL via AlGaN/GaN multiple quantum barrier electron blocking layer," *Optics Express*, vol. 23, no. 21, p. 27 145, 2015.

[179] T. Hamaguchi, N. Fuutagawa, S. Izumi, M. Murayama, and H. Narui, "Milliwatt-class GaN-based blue vertical-cavity surface-emitting lasers fabricated by epitaxial lateral overgrowth," *Physica Status Solidi (A)*, vol. 213, no. 5, pp. 1170–1176, 2016.

[180] T. Furuta, K. Matsui, K. Horikawa, K. Ikeyama, Y. Kozuka, S. Yoshida, T. Akagi, T. Takeuchi, S. Kamiyama, M. Iwaya, and I. Akasaki, "Room-temperature CW operation of a nitride-based vertical-cavity surface-emitting laser using thick GaInN quantum wells," *Japanese Journal of Applied Physics*, vol. 55, no. 5S, 05FJ11, 2016.

[181] C. A. Forman, S. Lee, E. C. Young, J. A. Kearns, D. A. Cohen, J. T. Leonard, T. Margalith, S. P. DenBaars, and S. Nakamura, "Continuous-wave operation of m-plane GaN-based vertical-cavity surface-emitting lasers with a tunnel junction intracavity contact," *Applied Physics Letters*, vol. 112, no. 11, p. 111 106, 2018.

[182] R. Xu, Y. Mei, H. Xu, L.-Y. Ying, Z. Zheng, H. Long, D. Zhang, B. Zhang, and J. Liu, "Green vertical-cavity surface-emitting lasers based on combination of blue-emitting quantum wells and cavity-enhanced recombination," *IEEE Transactions on Electron Devices*, vol. 65, no. 10, pp. 4401–4406, 2018.

[183] M. Kuramoto, S. Kobayashi, T. Akagi, K. Tazawa, K. Tanaka, T. Saito, and T. Takeuchi, "Enhancement of slope efficiency and output power in GaN-based vertical-cavity surface-emitting lasers with a SiO_2-buried lateral index guide," *Applied Physics Letters*, vol. 112, no. 11, p. 111 104, 2018.

[184] M. Kuramoto, S. Kobayashi, K. Tazawa, K. Tanaka, T. Akagi, and T. Saito, "In-phase supermode operation in GaN-based vertical-cavity surface-emitting laser," *Applied Physics Letters*, vol. 115, no. 4, p. 041 101, 2019.

[185] R. Iida, Y. Ueshima, W. Muranaga, S. Iwayama, T. Takeuchi, S. Kamiyama, M. Iwaya, and I. Akasaki, "GaN-based vertical cavity surface emitting lasers with lateral optical confinements and conducting distributed Bragg reflectors," *Japanese Journal of Applied Physics*, vol. 59, no. SG, SGGE08, 2020.

[186] W. Muranaga, T. Akagi, R. Fuwa, S. Yoshida, J. Ogimoto, Y. Akatsuka, S. Iwayama, T. Takeuchi, S. Kamiyama, M. Iwaya, and I. Akasaki, "GaN-based vertical-cavity surface-emitting lasers using n-type conductive AlInN/GaN bottom distributed Bragg reflectors with graded interfaces," *Japanese Journal of Applied Physics*, vol. 58, no. SC, SCCC01, 2019.

[187] Y. Mei, G.-E. Weng, B.-P. Zhang, J.-P. Liu, W. Hofmann, L.-Y. Ying, J.-Y. Zhang, Z.-C. Li, H. Yang, and H.-C. Kuo, "Quantum dot vertical-cavity surface-emitting lasers covering the 'green gap'," *Light: Science & Applications*, vol. 6, no. 1, e16199–e16199, 2017.

[188] M. Kuramoto, S. Kobayashi, T. Akagi, K. Tazawa, K. Tanaka, K. Nakata, and T. Saito, "Watt-class blue vertical-cavity surface-emitting laser arrays," *Applied Physics Express*, vol. 12, no. 9, p. 091 004, 2019.

[189] T. Hamaguchi, Y. Hoshina, K. Hayashi, M. Tanaka, M. Ito, M. Ohara, T. Jyoukawa, N. Kobayashi, H. Watanabe, M. Yokozeki, R. Koda, and K. Yanashima, "Room-temperature continuous-wave operation of green vertical-cavity surface-emitting lasers with a curved mirror fabricated on $\{20\bar{2}1\}$ semi-polar GaN," *Applied Physics Express*, vol. 13, no. 4, p. 041 002, 2020.

[190] H. Xu, Y. Mei, R. B. Xu, L. Y. Ying, X. L. Su, J. P. Liu, and B. P. Zhang, "Green VCSELs based on nitride semiconductors," *Japanese Journal of Applied Physics*, vol. 59, no. SO, SO0803, 2020.

[191] R. Chen, H. D. Sun, T. Wang, K. N. Hui, and H. W. Choi, "Optically pumped ultraviolet lasing from nitride nanopillars at room temperature," *Applied Physics Letters*, vol. 96, no. 24, p. 241 101, 2010.

[192] Y.-S. Liu, A. F. M. Saniul Haq, K. Mehta, T.-T. Kao, S. Wang, H. Xie, S.-C. Shen, P. D. Yoder, F. A. Ponce, T. Detchprohm, and R. D. Dupuis, "Optically pumped vertical-cavity surface-emitting laser at 374.9 nm with an electrically conducting n-type distributed Bragg reflector," *Applied Physics Express*, vol. 9, no. 11, p. 111 002, 2016.

[193] H. Zhou, M. Diagne, E. Makarona, A. Nurmikko, J. Han, K. Waldrip, and J. Figiel, "Near ultraviolet optically pumped vertical cavity laser," *Electronics Letters*, vol. 36, no. 21, p. 1777, 2000.

[194] T. Someya, K. Tachibana, J. Lee, T. Kamiya, and Y. Arakawa, "Lasing emission from an $In_{0.1}Ga_{0.9}N$ vertical cavity surface emitting laser," *Japanese Journal of Applied Physics*, vol. 37, no. 12A, pp. L1424–L1426, 1998.

[195] S. Kako, T. Someya, and Y. Arakawa, "Observation of enhanced spontaneous emission coupling factor in nitride-based vertical-cavity surface-emitting laser," *Applied Physics Letters*, vol. 80, no. 5, pp. 722–724, 2002.

[196] J.-Y. Zhang, L.-E. Cai, B.-P. Zhang, S.-Q. Li, F. Lin, J.-Z. Shang, D.-X. Wang, K.-C. Lin, J.-Z. Yu, and Q.-M. Wang, "Blue-violet lasing of optically pumped GaN-based vertical cavity surface-emitting laser with dielectric distributed Bragg reflectors," *Journal of Lightwave Technology*, vol. 27, no. 1, pp. 55–59, 2009.

[197] S. H. Park, J. Kim, H. Jeon, T. Sakong, S. N. Lee, S. Chae, Y. Park, C. H. Jeong, G. Y. Yeom, and Y. H. Cho, "Room-temperature GaN vertical-cavity surface-emitting laser operation in an extended cavity scheme," *Applied Physics Letters*, vol. 83, no. 11, pp. 2121–2123, 2003.

[198] Z. Zheng, Y. Mei, H. Long, J. Hoo, S. Guo, Q. Li, L. Ying, Z. Zheng, and B. Zhang, "AlGaN-based deep ultraviolet vertical-cavity surface-emitting laser," *IEEE Electron Device Letters*, vol. 42, no. 3, pp. 375–378, 2021.

[199] Z. Zhang, M. Kushimoto, T. Sakai, N. Sugiyama, L. J. Schowalter, C. Sasaoka, and H. Amano, "A 271.8 nm deep-ultraviolet laser diode for room temperature operation," *Applied Physics Express*, vol. 12, no. 12, p. 124 003, 2019.

[200] T. Sakai, M. Kushimoto, Z. Zhang, N. Sugiyama, L. J. Schowalter, Y. Honda, C. Sasaoka, and H. Amano, "On-wafer fabrication of etched-mirror UV-C laser diodes with the ALD-deposited DBR," *Applied Physics Letters*, vol. 116, no. 12, p. 122 101, 2020.

[201] J. Wang, C.-w. Tsou, H. Jeong, Y. J. Park, T. Detchprohm, K. Mehta, P. D. Yoder, R. D. Dupuis, and S.-C. Shen, "III-nitride vertical resonant cavity light-emitting diodes with hybrid air-gap/AlGaN-dielectric distributed Bragg reflectors," in *Proc. of SPIE, Gallium Nitride Materials and Devices XIV*, H. Morkoç, H. Fujioka, and U. T. Schwarz, Eds., SPIE, 2019, 109180E.

[202] Y.-s. Liu, T.-t. Kao, K. Mehta, S.-c. Shen, P. D. Yoder, T. Detchprohm, R. D. Dupuis, H. Xie, and F. A. Ponce, "Development for ultraviolet vertical cavity surface emitting lasers," in *Proc. of SPIE, Gallium Nitride Materials and Devices XI*, J.-I. Chyi, H. Fujioka, H. Morkoç, Y. Nanishi, U. T. Schwarz, and J.-I. Shim, Eds., vol. 9748, 2016, p. 974 815.

[203] H. Gerischer, "Electron-transfer kinetics of redox reactions at the semiconductor/electrolyte contact. A new approach," *The Journal of Physical Chemistry*, vol. 95, no. 3, pp. 1356–1359, 1991.

[204] C. Zhang, G. Yuan, A. Bruch, K. Xiong, H. X. Tang, and J. Han, "Toward quantitative electrochemical nanomachining of III-nitrides," *Journal of The Electrochemical Society*, vol. 165, no. 10, E513–E520, 2018.

[205] W. J. Tseng, D. H. van Dorp, R. R. Lieten, P. M. Vereecken, and G. Borghs, "Anodic etching of n-GaN epilayer into porous GaN and its photoelectrochemical properties," *The Journal of Physical Chemistry C*, vol. 118, no. 51, pp. 29 492–29 498, 2014.

[206] M. A. Khan, D. T. Olson, J. M. Van Hove, and J. N. Kuznia, "Vertical-cavity, room-temperature stimulated emission from photopumped GaN films deposited over sapphire substrates using low-pressure metalorganic chemical vapor deposition," *Applied Physics Letters*, vol. 58, no. 14, pp. 1515–1517, 1991.

[207] H. Amano, N. Watanabe, N. Koide, and I. Akasaki, "Room-temperature low-threshold surface-stimulated emission by optical pumping from $Al_{0.1}Ga_{0.9}N$/GaN double heterostructure," *Japanese Journal of Applied Physics*, vol. 32, no. 7B, pp. L1000–L1002, 1993.

[208] X. Li, H. Xie, F. A. Ponce, J.-h. Ryou, T. Detchprohm, and R. D. Dupuis, "Onset of surface stimulated emission at 260 nm from AlGaN multiple quantum wells," *Applied Physics Letters*, vol. 107, no. 24, p. 241 109, 2015.

[209] "Scrutinizing lasers," *Nature Photonics*, vol. 11, no. 3, pp. 139–139, 2017.

[210] N. G. Anderson, D. A. S. Loeber, J. M. Redwing, M. A. Tischler, and J. S. Flynn, "Comment on "Lasing emission from an $In_{0.1}Ga_{0.9}N$ vertical cavity surface emitting laser"," *Japanese Journal of Applied Physics*, vol. 38, no. 8, pp. 4794–4795, 1999.

[211] M. A. Khan, S. Krishnankutty, R. A. Skogman, J. N. Kuznia, D. T. Olson, and T. George, "Vertical–cavity stimulated emission from photopumped InGaN/GaN heterojunctions at room temperature," *Applied Physics Letters*, vol. 65, no. 5, pp. 520–521, 1994.

[212] D. M. Bagnall and K. P. O'Donnell, "Comment on "Vertical-cavity stimulated emission from photopumped InGaN/GaN heterojunctions at room temperature" [Appl. Phys. Lett. 65 , 520 (1994)]," *Applied Physics Letters*, vol. 68, no. 22, pp. 3197–3197, 1996.

[213] M. Asif Khan, S. Krishnankutty, R. A. Skogman, J. N. Kuznia, D. T. Olson, and T. George, "Response to "Comment on 'Vertical-cavity stimulated emission from photopumped InGaN/GaN heterojunctions at room temperature' " [Appl. Phys. Lett. 68 , 3197 (1996)]," *Applied Physics Letters*, vol. 68, no. 22, pp. 3198–3198, 1996.

[214] Y. Mei, R.-B. Xu, H. Xu, L.-Y. Ying, Z.-W. Zheng, B.-P. Zhang, M. Li, and J. Zhang, "A comparative study of thermal characteristics of GaN-based VCSELs with three different typical structures," *Semiconductor Science and Technology*, vol. 33, no. 1, p. 015 016, 2018.

[215] S. Mishkat-Ul-Masabih, J. Leonard, D. Cohen, S. Nakamura, and D. Feezell, "Techniques to reduce thermal resistance in flip-chip GaN-based VCSELs," *Physica Status Solidi (A)*, vol. 214, no. 8, p. 1 600 819, 2017.

[216] G. Cardinali, "Thermal management of ultraviolet LEDs and VCSELs: computer-aided multiphysics optimization," *Master's thesis, Politecnico di Torino*, 2019.

[217] L. Persson, "Thermal and optical simulations of blue- and UV-emitting vertical-cavity surface-emitting lasers (VCSELs)," *Master's thesis, Chalmers University of Technology*, 2020.

[218] D. Chen, H. Xiao, and J. Han, "Nanopores in GaN by electrochemical anodization in hydrofluoric acid: Formation and mechanism," *Journal of Applied Physics*, vol. 112, no. 6, p. 064 303, 2012.

[219] M. Mohajeri, "Fabrication of high-reflectivity HfO_2/SiO_2 distributed Bragg reflectors for UVC VCSELs," *Master's thesis, Chalmers University of Technology*, 2020.

[220] A. Mutig and D. Bimberg, "Progress on High-Speed 980 nm VCSELs for short-reach optical interconnects," *Advances in Optical Technologies*, vol. 2011, p. 290 508, 2011.

[221] M. Muller, W. Hofmann, T. Grundl, M. Horn, P. Wolf, R. D. Nagel, E. Ronneberg, G. Bohm, D. Bimberg, and M. C. Amann, "1550-nm high-speed short-cavity VCSELs," *IEEE Journal of Selected Topics in Quantum Electronics*, vol. 17, no. 5, pp. 1158–1166, 2011.

[222] P. Westbergh, J. S. Gustavsson, B. Kögel, A. Haglund, and A. Larsson, "Impact of photon lifetime on high-speed VCSEL performance," *IEEE Journal of Selected Topics in Quantum Electronics*, vol. 17, no. 6, pp. 1603–1613, 2011.

[223] S. Yoshida, K. Ikeyama, T. Yasuda, T. Furuta, T. Takeuchi, M. Iwaya, S. Kamiyama, and I. Akasaki, "Electron and hole accumulations at GaN/AlInN/GaN interfaces and conductive n-type AlInN/GaN distributed Bragg reflectors," *Japanese Journal of Applied Physics*, vol. 55, no. 5S, 05FD10, 2016.

[224] K. Ikeyama, Y. Kozuka, K. Matsui, S. Yoshida, T. Akagi, Y. Akatsuka, N. Koide, T. Takeuchi, S. Kamiyama, M. Iwaya, and I. Akasaki, "Room-temperature continuous-wave operation of GaN-based vertical-cavity surface-emitting lasers with n-type conducting AlInN/GaN distributed Bragg reflectors," *Applied Physics Express*, vol. 9, no. 10, p. 102 101, 2016.

[225] C. Zhang, K. Xiong, G. Yuan, and J. Han, "A resonant-cavity blue-violet light-emitting diode with conductive nanoporous distributed Bragg reflector," *Physica Status Solidi (A)*, vol. 214, no. 8, p. 1 600 866, 2017.

[226] T. Zhou, C. Zhang, R. ElAfandy, G. Yuan, Z. Deng, K. Xiong, F.-M. Chen, Y.-K. Kuo, K. Xu, and J. Han, "Thermal transport of nanoporous gallium nitride for photonic applications," *Journal of Applied Physics*, vol. 125, no. 15, p. 155 106, 2019.

[227] M. Arita, M. Nishioka, and Y. Arakawa, "InGaN vertical microcavity LEDs with a Si-doped AlGaN/GaN distributed Bragg reflector," *Physica Status Solidi (A)*, vol. 194, no. 2, pp. 403–406, 2002.

[228] S. Figge, H. Dartsch, T. Aschenbrenner, C. Kruse, and D. Hommel, "Distributed Bragg reflectors in comparison to RUGATE and nested super lattices – growth, reflectivity, and conductivity," *Physica Status Solidi (C)*, vol. 5, no. 6, pp. 1839–1842, 2008.

[229] Y.-S. Liu, A. F. M. S. Haq, T.-T. Kao, K. Mehta, S.-C. Shen, T. Detchprohm, P. D. Yoder, R. D. Dupuis, H. Xie, and F. A. Ponce, "Electrically conducting n-type AlGaN/GaN distributed Bragg reflectors grown by metalorganic chemical vapor deposition," *Journal of Crystal Growth*, vol. 443, pp. 81–84, 2016.

[230] A. T. Ping, M. Asif Khan, and I. Adesida, "Ohmic contacts to n-type GaN using Pd/Al metallization," *Journal of Electronic Materials*, vol. 25, no. 5, pp. 819–824, 1996.

[231] A. Malmros, H. Blanck, and N. Rorsman, "Electrical properties, microstructure, and thermal stability of Ta-based ohmic contacts annealed at low temperature for GaN HEMTs," *Semiconductor Science and Technology*, vol. 26, no. 7, p. 075 006, 2011.

[232] G. S. Marlow and M. B. Das, "The effects of contact size and non-zero metal resistance on the determination of specific contact resistance," *Solid-State Electronics*, vol. 25, no. 2, pp. 91–94, 1982.

[233] F. Bernardini, V. Fiorentini, and D. Vanderbilt, "Spontaneous polarization and piezoelectric constants of III-V nitrides," *Physical Review B*, vol. 56, no. 16, R10024–R10027, 1997.

[234] C. E. Dreyer, A. Janotti, C. G. Van de Walle, and D. Vanderbilt, "Correct implementation of polarization constants in wurtzite materials and impact on III-nitrides," *Physical Review X*, vol. 6, no. 2, p. 021 038, 2016.

[235] J. C. Johnson, H.-J. Choi, K. P. Knutsen, R. D. Schaller, P. Yang, and R. J. Saykally, "Single gallium nitride nanowire lasers," *Nature Materials*, vol. 1, no. 2, pp. 106–110, 2002.

[236] C. Li, J. B. Wright, S. Liu, P. Lu, J. J. Figiel, B. Leung, W. W. Chow, I. Brener, D. D. Koleske, T. S. Luk, D. F. Feezell, S. R. Brueck, and G. T. Wang, "Nonpolar InGaN/GaN core-shell single nanowire lasers," *Nano Letters*, vol. 17, no. 2, pp. 1049–1055, 2017.

[237] T. Frost, S. Jahangir, E. Stark, S. Deshpande, A. Hazari, C. Zhao, B. S. Ooi, and P. Bhattacharya, "Monolithic electrically injected nanowire array edge-emitting laser on (001) silicon," *Nano Letters*, vol. 14, no. 8, pp. 4535–4541, 2014.

[238] K. H. Li, X. Liu, Q. Wang, S. Zhao, and Z. Mi, "Ultralow-threshold electrically injected AlGaN nanowire ultraviolet lasers on Si operating at low temperature," *Nature Nanotechnology*, vol. 10, no. 2, pp. 140–144, 2015.

[239] B. H. Le, X. Liu, N. H. Tran, S. Zhao, and Z. Mi, "An electrically injected AlGaN nanowire defect-free photonic crystal ultraviolet laser," *Optics Express*, vol. 27, no. 4, p. 5843, 2019.

[240] Y.-H. Ra, R. T. Rashid, X. Liu, S. M. Sadaf, K. Mashooq, and Z. Mi, "An electrically pumped surface-emitting semiconductor green laser," *Science Advances*, vol. 6, no. 1, eaav7523, 2020.

[241] C. Y. Huang, J. J. Lin, T. C. Chang, C. Y. Liu, T. Y. Tai, K. B. Hong, T. C. Lu, and H. C. Kuo, "Collective lasing behavior of monolithic GaN-InGaN core-shell nanorod lattice under room temperature," *Nano Letters*, vol. 17, no. 10, pp. 6228–6234, 2017.

[242] C. Tessarek, R. Röder, T. Michalsky, S. Geburt, H. Franke, R. Schmidt-Grund, M. Heilmann, B. Hoffmann, C. Ronning, M. Grundmann, and S. Christiansen, "Improving the optical properties of self-catalyzed GaN microrods toward whispering gallery mode lasing," *ACS Photonics*, vol. 1, no. 10, pp. 990–997, 2014.

[243] A. Das, J. Heo, M. Jankowski, W. Guo, L. Zhang, H. Deng, and P. Bhattacharya, "Room temperature ultralow threshold GaN nanowire polariton laser," *Physical Review Letters*, vol. 107, no. 6, p. 066 405, 2011.

[244] J. Heo, S. Jahangir, B. Xiao, and P. Bhattacharya, "Room-temperature polariton lasing from GaN nanowire array clad by dielectric microcavity," *Nano Letters*, vol. 13, no. 6, pp. 2376–2380, 2013.

[245] M. Behzadirad, M. Nami, N. Wostbrock, M. R. Zamani Kouhpanji, D. F. Feezell, S. R. J. Brueck, and T. Busani, "Scalable top-down approach tailored by interferometric lithography to achieve large-area single-mode GaN nanowire laser arrays on sapphire substrate," *ACS Nano*, vol. 12, no. 3, pp. 2373–2380, 2018.

[246] B. Damilano, P.-M. Coulon, S. Vézian, V. Brändli, J.-Y. Duboz, J. Massies, and P. A. Shields, "Top-down fabrication of GaN nano-laser arrays by displacement Talbot lithography and selective area sublimation," *Applied Physics Express*, vol. 12, no. 4, p. 045 007, 2019.

[247] Q. Li, K. R. Westlake, M. H. Crawford, S. R. Lee, D. D. Koleske, J. J. Figiel, K. C. Cross, S. Fathololoumi, Z. Mi, and G. T. Wang, "Optical performance of top-down fabricated InGaN/GaN nanorod light emitting diode arrays," *Optics Express*, vol. 19, no. 25, p. 25 528, 2011.

[248] Q. Sun, C. D. Yerino, B. Leung, J. Han, and M. E. Coltrin, "Understanding and controlling heteroepitaxy with the kinetic Wulff plot: A case study with GaN," *Journal of Applied Physics*, vol. 110, no. 5, p. 053 517, 2011.

[249] V. Jindal and F. Shahedipour-Sandvik, "Theoretical prediction of GaN nanostructure equilibrium and nonequilibrium shapes," *Journal of Applied Physics*, vol. 106, no. 8, p. 083 115, 2009.

[250] M. Pollnau and M. Eichhorn, "Spectral coherence, Part I: Passive-resonator linewidth, fundamental laser linewidth, and Schawlow-Townes approximation," *Progress in Quantum Electronics*, vol. 72, p. 100 255, 2020.

[251] M. A. Reshchikov and H. Morkoç, "Luminescence properties of defects in GaN," *Journal of Applied Physics*, vol. 97, no. 6, p. 061 301, 2005.

[252] *COMSOL - Wave Optics Module User's Guide*, 2013.

[253] M. Bengths, "Design of nanowire-based vertical-cavity surface-emitting lasers," *Master's thesis, Chalmers University of Technology*, 2018.

[254] A.-L. Henneghien, B. Gayral, Y. Désières, and J.-M. Gérard, "Simulation of waveguiding and emitting properties of semiconductor nanowires with hexagonal or circular sections," *Journal of the Optical Society of America B*, vol. 26, no. 12, p. 2396, 2009.

[255] S. Kumari, E. P. Haglund, J. S. Gustavsson, A. Larsson, G. Roelkens, and R. G. Baets, "Vertical-cavity silicon-integrated laser with in-plane waveguide emission at 850 nm," *Laser & Photonics Reviews*, vol. 12, no. 2, p. 1 700 206, 2018.

[256] D. J. Blumenthal, "Photonic integration for UV to IR applications," *APL Photonics*, vol. 5, no. 2, p. 020 903, 2020.

[257] M. Abid, T. Moudakir, G. Orsal, S. Gautier, A. En Naciri, Z. Djebbour, J.-H. Ryou, G. Patriarche, L. Largeau, H. J. Kim, Z. Lochner, K. Pantzas, D. Alamarguy, F. Jomard, R. D. Dupuis, J.-P. Salvestrini, P. L. Voss, and A. Ougazzaden, "Distributed Bragg reflectors based on diluted boron-based BAlN alloys for deep ultraviolet optoelectronic applications," *Applied Physics Letters*, vol. 100, no. 5, p. 051 101, 2012.

[258] Q. Li, Q. Zhang, Y. Bai, H. Zhang, P. Hu, Y. Li, and F. Yun, "Deep-UV hexagonal boron nitride (hBN)/BAlN distributed Bragg reflectors fabricated by RF-sputtering," *Optical Materials Express*, vol. 11, no. 1, p. 180, 2021.

[259] M. Pristovsek, D. van Dinh, T. Liu, and N. Ikarashi, "Wurtzite AlP_yN_{1-y}: a new III-V compound semiconductor lattice-matched to GaN (0001)," *Applied Physics Express*, vol. 13, no. 11, p. 111 001, 2020.

[260] D. Massoubre, L. Wang, L. Hold, A. Fernandes, J. Chai, S. Dimitrijev, and A. Iacopi, "Vertically conductive single-crystal SiC-based Bragg reflector grown on Si wafer," *Scientific Reports*, vol. 5, p. 17 026, 2015.

[261] C. Berger, A. Lesnik, T. Zettler, G. Schmidt, P. Veit, A. Dadgar, J. Bläsing, J. Christen, and A. Strittmatter, "Metalorganic chemical vapor phase epitaxy of narrow-band distributed Bragg reflectors realized by GaN:Ge modulation doping," *Journal of Crystal Growth*, vol. 440, pp. 6–12, 2016.

[262] Z. Bi, F. Lenrick, J. Colvin, A. Gustafsson, O. Hultin, A. Nowzari, T. Lu, R. Wallenberg, R. Timm, A. Mikkelsen, B. J. Ohlsson, K. Storm, B. Monemar, and L. Samuelson, "InGaN platelets: Synthesis and applications toward green and red light-emitting diodes," *Nano Letters*, vol. 19, no. 5, pp. 2832–2839, 2019.